Millimeter-wave Spectra of the Jovian Planets

By

Joanna Joiner

Paul G. Steffes, Principal Investigator

School of Electrical Engineering

Georgia Institute of Technology

Atlanta, GA 30332-0250

(404) 894-3128

August, 1991

Technical Report No. 1991-1

Prepared under NASA grant NAGW-533

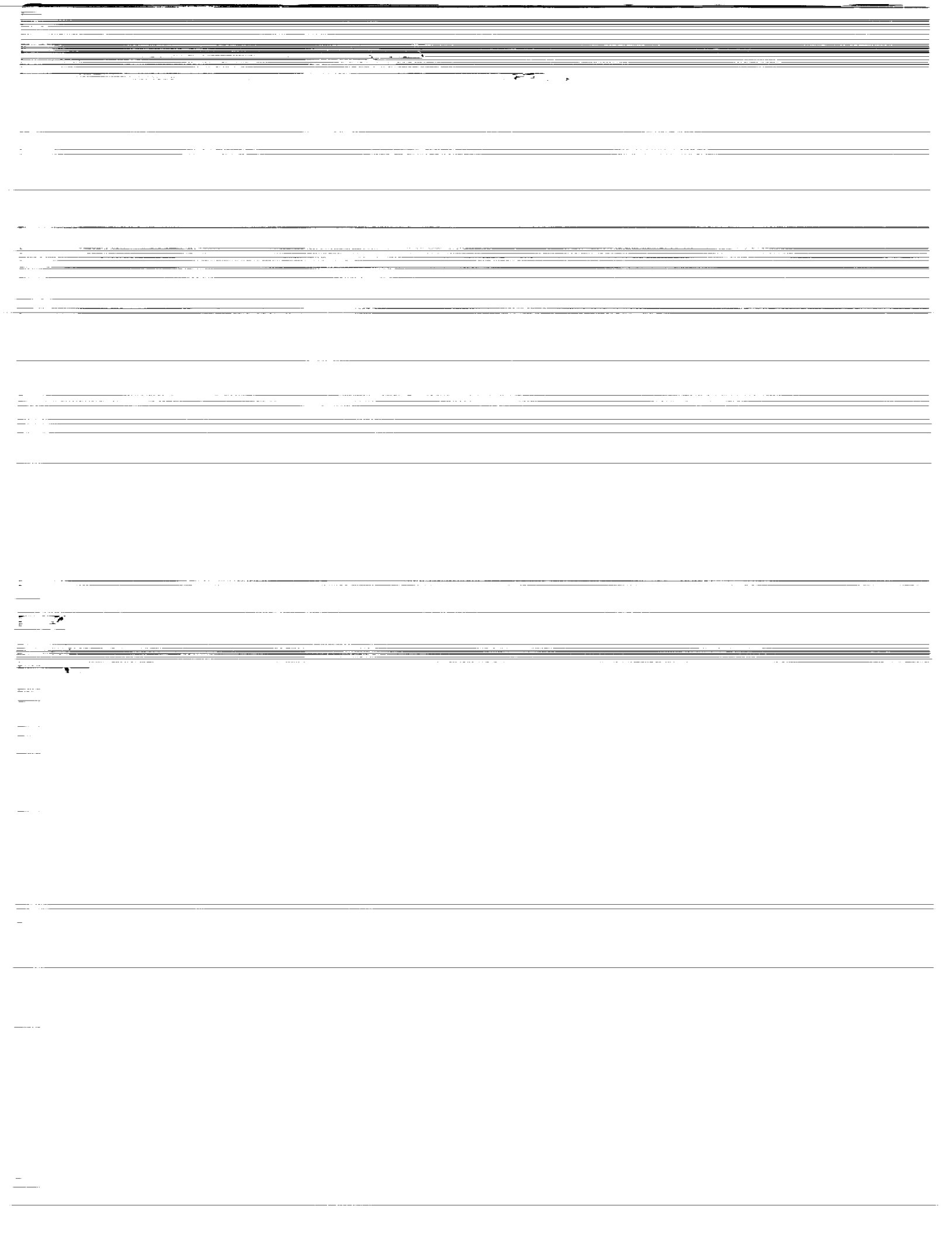

Acknowledgments

I am indebted to my advisor, Paul G. Steffes, for his guidance, optimism, confidence, and patience. I thank him for his assistance during this research and for preparing me for life beyond graduate school. I thank the following faculty committee members for their time and careful examination of the document: A. J. Gasiewski (reader), G. S. Smith (reader), J. A. Buck (chairman of the qualifying and proposal committees), and C. G. Justus.

I thank D. P. Campbell and S. Halpbern of the Georgia Tech Research Institute (GTRI) and T. E. Brewer (Georgia Tech) for their generous assistance with the laboratory equipment and for providing illuminating discussions. I also thank J. J. Gallagher (GTRI) whose selflessness and courage is an example for all. I thank the staff of the Caltech Submillimeter Observatory (CSO), especially T. D. Groesbeck and A. E. Schinckel, for their assistance with the hardware and data analysis at the CSO. I also thank T. R. Spilker (Stanford), I. dePater (Berkeley), P. N. Romani (SSAI, NASA-Goddard), K. S. Noll (NRC, NASA-Marshall), B. Bezard, and E. Lellouch (Observatoire de Paris-Meudon) for illuminating discussions and helpful suggestions.

Finally, I thank the following family and friends for their constant support and encouragement and for putting up with me during difficult times: Noel and Selma Wang, J. Robert and Valerie Joiner, Jennifer and Gilbert Lawson, Mary Frances Joiner, Bess Fleckman, Elsie Wang, Cliff Wang, Keith Noll, Michael Wileman, Jon Jenkins, Tony Fahd, Cindy Stokes, Lori Cabena, and Lynne Patterson.

This work was supported by the Planetary Atmospheres Program of the Solar System Exploration Division (Office of Space Science and Applications) of the National Aeronautics and Space Administration under grant NAGW-533 and by the Georgia Tech Space Grant Consortium.

Contents

List of Figures

List of Tables

Summary

The millimeter-wave portion of the electromagnetic spectrum is critical for understanding the subcloud atmospheric structure of the Jovian planets (Jupiter, Saturn, Uranus, and Neptune). This research utilizes a combination of laboratory measurements, computer modeling, and radio astronomical observation in order to obtain a better understanding of the millimeter-wave spectra of the Jovian planets. The pressure-broadened absorption from gaseous ammonia (NH_3) and hydrogen sulfide (H_2S) has been measured in the laboratory under simulated conditions for the Jovian atmospheres. We have developed new formalisms for computing the absorptivity of gaseous NH_3 and H_2S based on our laboratory measurements. We have developed a radiative transfer and thermochemical model to predict the abundance and distribution of absorbing constituents in the Jovian atmospheres. We use the model to compute the millimeter-wave emission from the Jovian planets. The model utilizes the results of the laboratory measurements and is also used to evaluate other possible candidates for millimeter-wave absorption in the Jovian atmospheres. Finally, we have observed Jupiter near 1.4 mm using the Caltech Submillimeter Observatory (CSO) in an attempt to detect gaseous hydrogen sulfide. Sulfur compounds have been identified on Io, one of Jupiter's moons, but they have never been detected on any of the Jovian planets. Although we were not able to detect hydrogen sulfide, we were able to make a good observation of Jupiter's brightness temperature at this wavelength using Mars as the calibration standard. This research ultimately adds to the understanding of the composition and cloud structure of the Jovian planets and provides clues to the origin and evolution of the planets and solar system.

CHAPTER 1

INTRODUCTION

Section 1.1 lays the foundation for this work as it relates to the study of the Jovian atmospheres. The organization of the document follows in Section 1.2.

1.1 Background and Motivation

The Jovian planets (Jupiter, Saturn, Uranus, and Neptune) are the most massive planetary bodies in our solar system. They are also known as the gaseous giant planets because a significant fraction of their mass is contained within their atmospheres. Atmospheric features such as the great red spot on Jupiter were observed as early as the 17th century. However, little was known about the composition of the Jovian atmospheres until this century. Advances in instrumentation over the past few decades have allowed scientists to compile much new information about the atmospheric structure and composition of the Jovian planets. The use of instruments aboard spacecraft has enhanced this new wealth of information.

The abundances of elements observed in the atmospheres of the four Jovian planets provides one of the biggest clues to the origin and evolution of the planets. The Jovian planets have retained much of their original atmospheres, unlike their inner solar system counterparts (Venus, Earth, and Mars). The most abundant elements in the Jovian atmospheres (and the solar system) are hydrogen and helium. Small abundances of other elements are found to exist primarily in reduced forms. The heavier volatiles such as CH_4, NH_3, and H_2S appear to be enriched

(relative to the sun) in the atmospheres of the giant planets (see, *e.g.*, de Pater *et al.*, 1989 and Grossman, 1990). The enrichment of heavier elements favors the core-instability model (see, *e.g.*, Pollack and Bodenheimer, 1989) in which the core of the giant planets is formed first by solid accretion. When a critical mass is reached, the planet begins to rapidly accrete gas from the surrounding solar nebula.

Only six minor elements have been positively detected on the giant planets. These elements, carbon, oxygen, nitrogen, phosphorous, germanium, and arsenic, form a cluster in the periodic table. Sulfur remains mysteriously absent from this list. The formation of clouds may deplete sulfur (in the form of gaseous H_2S) in the upper atmospheres of the Jovian planets, making it difficult to detect with conventional methods. Ground and space based radio observations and experiments provide one of best means to extract information about the presence and abundance of absorbing constituents, including H_2S, below the optically thick clouds. One goal of this research is to use the millimeter-wave spectrum to search for gaseous H_2S on Jupiter.

Radio occultation is an example of a space-based experiment which can provide information about the subcloud regions of the giant planets. During an occultation, a spacecraft travels behind a planet and transmits a stable CW signal through the atmosphere of the planet. This signal is refracted and attenuated as it passes through the atmosphere of the planet. The resulting signal is received on the earth. Information about the planetary atmosphere can be inferred from the precise measurement of the signal's frequency shift and attenuation. For example, the *Voyager* spacecraft have been used in radio occultation experiments to retrieve temperature-pressure profiles for all four of the Jovian planets (see, *e.g.*, Lindal, *et al.*, 1981). These experiments typically take place at S and X Band (between 2.3 and 8.4 GHz). Radio occultations are limited in that a single occultation can provide information only at one localized area of the planet. The data from only

one location may not be representative of the conditions elsewhere on the planet.

The expected arrival of the Galileo spacecraft at Jupiter in 1995 and the Cassini mission to Saturn in the next century will provide additional clues to the composition of the two closest Jovian planets. These spacecraft will drop probes into the atmosphere of the planets. Mass spectrometers will identify gases within the atmosphere. Again, this type of *in-situ* observation is limited in that a single probe gives information for only one location on the planet.

Ground-based radio astronomy has a distinct advantage over these space-based experiments in that the entire planet is observable with a single radio telescope or an array of telescopes. Many observations of the emission from the giant planets have been made with radio telescopes at wavelengths from 1 mm to several meters. However, the interpretation of the observations is still in the initial stages. Laboratory studies of potential absorbers are needed in order to correctly interpret the measured emission from the planets. The dearth of laboratory absorption measurements under planetary conditions has hampered the interpretation of the Jovian millimeter-wave spectra in the past. Another goal of this research is to begin a program of laboratory measurements so that the available observations can be correctly interpreted. The millimeter-wave region of the spectrum will then be an important piece of the puzzle which theorists use to piece together the origin and evolution of the planets.

Another difficulty in interpreting millimeter observations of the giant planets is the large uncertainty in the absolute flux calibration. Accurate calibration of the millimeter wavelength planetary observations is critical if meaningful comparisons are to be made between different observations and between the observations and radiative transfer models. Mars is the most frequently used calibrator at these wavelengths. However, the uncertainty in the estimated flux from Mars is reported to be approximately 10% (Griffin *et al.*, 1986). Before the millimeter-wave spectra of the Jovian planets are fully understood, better calibration techniques will be

needed.

A long standing discrepancy between modeled and observed brightness temperatures of Jupiter at millimeter wavelengths (see, *e.g.*, de Pater and Massie, 1985) provided the initial motivation for this work. One of the largest uncertainties in modeling the millimeter-wave emission from the giant planets is the absorption coefficient of gaseous ammonia (NH_3). This gas is by far the strongest millimeter wave opacity source on Jupiter. This work began with laboratory measurements of the millimeter-wave absorption from gaseous NH_3 under simulated Jovian conditions. The experiments were conducted at two frequency bands where a number of radio astronomical observations have been made. The results of the experiments were incorporated into a radiative transfer model which predicts the radio emission from the Jovian planets. The results of the radiative transfer modeling provided the motivation for a millimeter-wave observation of Jupiter in an attempt to detect gaseous hydrogen sulfide (H_2S). A laboratory measurement of the pressure-broadening effects of hydrogen and helium on hydrogen sulfide was designed in order to correctly interpret the observation.

This work contributes new experimental, theoretical, and observational results which lead to a better understanding of the millimeter-wave spectra of the Jovian planets. Millimeter-wave instrumentation for planetary spectroscopy is still in an evolutionary state and will continue to provide new and improved planetary observations in the future. The results of the laboratory measurements presented in this work will help to interpret past, present, *and* future observations of the giant planets. It is hoped that this work will stimulate future research in this area.

1.2 Organization

The scope of this research may be conveniently divided into three areas:

1. Laboratory measurements of the millimeter-wave absorption from gaseous ammonia (NH_3) and hydrogen sulfide (H_2S) in a simulated Jovian atmosphere

2. Radiative transfer and thermochemical modeling of the Jovian atmospheres

3. Dual-wavelength radio astronomical observation of Jupiter at 1.4 mm

Chapters 2, 3, and 4 discuss each of these areas, respectively.

Chapter 2 describes the laboratory configuration, experimental methodology, and results of millimeter-wave absorptivity measurements of gaseous ammonia (NH_3) and gaseous hydrogen sulfide (H_2S) under simulated Jovian conditions. The results are compared with various theories used to predict the millimeter-wave absorptivity of these gases.

The theory and application of a radiative transfer and thermochemical model are described in Chapter 3. We use a forward approach to model the emission from each of the giant planets. In a forward approach, the parameters of the radiative transfer model (*i.e.*, the abundances and distributions of absorbing constituents in the planetary atmospheres) are adjusted in order to obtain a good fit to the observed millimeter-wave spectra. The radiative transfer model utilizes the results of the laboratory measurements described in Chapter 2. We also develop new formalisms to compute the opacity from other sources in the Jovian atmospheres (*e.g.*, pressure-induced absorption and water vapor absorption).

Chapter 4 describes the approach, analysis, and results of a dual-wavelength radio astronomical observation of Jupiter at 1.4 mm. Relevant aspects of the instrumentation and calibration are described in detail.

A summary of the major conclusions and contributions of this work is presented in Chapter 5. In addition, this chapter provides several suggestions for future research.

CHAPTER 2

Laboratory Measurements of Ammonia (NH_3) and Hydrogen Sulfide (H_2S) Absorption Under Simulated Jovian Conditions

One of the outstanding problems in the millimeter spectroscopy of planets has been and continues to be the lack of adequate laboratory measurements of line shapes and widths of gases at relevant pressures and temperatures and with appropriate broadening agents. This chapter describes the laboratory apparatus, procedure, and results of gaseous ammonia (NH_3) and hydrogen sulfide (H_2S) absorptivity measurements under simulated Jovian conditions. The implications of the results presented in this chapter will be explored in Chapter 3.

2.1 Propagation in a Lossy Dielectric

The electric and magnetic fields of forward traveling waves in a lossy dielectric assume the form

$$E(x) = E_o e^{-\alpha x} e^{-j\beta x} \tag{2.1}$$

and

$$H(x) = H_o e^{-\alpha x} e^{-j\beta x}, \tag{2.2}$$

respectively, where α and β are known as the propagation constants; α is called the attenuation constant or absorption coefficient, and β is called the phase constant. The propagation constants are related to the related to the permittivity ϵ and permeability μ of the medium through which the wave travels as well as the frequency ω. In general, the permittivity of gases is complex and assumes the form

$$\epsilon = \epsilon' - j\epsilon''. \tag{2.3}$$

The permeability μ is approximately equal to the permeability of free space μ_o. The propagation constants for gases in general are

$$\alpha = \omega\sqrt{\frac{\mu\epsilon'}{2}\left[\sqrt{1+\left(\frac{\epsilon''}{\epsilon'}\right)^2}-1\right]} \tag{2.4}$$

and

$$\beta = \omega\sqrt{\frac{\mu\epsilon'}{2}\left[\sqrt{1+\left(\frac{\epsilon''}{\epsilon'}\right)^2}+1\right]}, \tag{2.5}$$

respectively. Their ratio is

$$\frac{\alpha}{\beta} = \sqrt{\frac{\left[1+\left(\frac{\epsilon''}{\epsilon'}\right)^2\right]^{1/2}-1}{\left[1+\left(\frac{\epsilon''}{\epsilon'}\right)^2\right]^{1/2}+1}}. \tag{2.6}$$

The loss tangent of a gaseous medium is defined as

$$\tan\delta = \frac{\epsilon''}{\epsilon'}, \tag{2.7}$$

and the quality factor in a gaseous medium (Q_g) is

$$Q_g = \frac{1}{\tan\delta} = \frac{\epsilon'}{\epsilon''}. \tag{2.8}$$

For a low-loss gas, the loss tangent is much less than unity. In this case, Equation 2.6 reduces to

$$\frac{\alpha}{\beta} = \frac{\epsilon''}{2\epsilon'}. \tag{2.9}$$

The phase constant β is

$$\beta = \frac{2\pi}{\lambda}, \tag{2.10}$$

so that the absorption coefficient can be written as

$$\alpha = \frac{\pi \epsilon''}{\lambda \epsilon'}. \tag{2.11}$$

2.2 Measurements of Ammonia (NH_3) Opacity at Ka-band and W-band

The absorption from gaseous ammonia strongly affects the millimeter-wave spectra of the giant planets. Ammonia is by far the largest millimeter-wave opacity source on Jupiter and Saturn. The opacity from gaseous ammonia must be known accurately before the potential effects of other absorbing constituents can be assessed.

Steffes and Jenkins (1987) have measured the absorption from gaseous ammonia between 1.38 and 18.5 cm (1.6 to 22 GHz). They have shown that to within experimental accuracy the absorptivity of gaseous NH_3 is correctly expressed by the modified Ben-Reuven line shape as discussed by Berge and Gulkis (1976). However, no laboratory absorption measurements have been made under simulated Jovian conditions at frequencies above 22 GHz (wavelengths less than 1.35 cm). Therefore, it is not known whether the use of the modified Ben-Reuven line shape is appropriate for computing gaseous ammonia opacity at frequencies above 22 GHz.

In order to test the Ben-Reuven and other line shapes, we have measured the opacity of gaseous ammonia (NH_3) under simulated Jovian conditions at several millimeter wavelengths. We conducted one set of experiments at several Ka-band frequencies between 32-40 GHz (7.5-9.38 mm). We conducted a second set of experiments at a frequency of 94 GHz or 3.2 mm (W-band). We conducted the experiments using mixing ratios of hydrogen, helium, and NH_3 which are similar to those found on Jupiter. Jupiter's atmosphere is approximately 90% H_2, 10% He, and 0.025% or 250 parts per million (ppm) NH_3. In order to measure absorption,

we need a higher NH_3 mixing ratio than that found on the Jovian planets. We used a mixture consisting of 88.34% hydrogen (H_2), 9.81% helium (He), and 1.85% ammonia (NH_3) for the Ka-band experiment. This corresponds to an NH_3 partial pressure of 28 torr within a total gas mixture pressure of 1560 torr (2 atm). The temperatures and pressures used in the experiments closely resemble those found in Jupiter's atmosphere at altitudes which emit Ka-band radiation. We conducted the experiments at a pressure of 2 atm and at a temperature of 203 K. A higher mixing ratio of NH_3 is needed in order to measure W-band absorption, because W-band ammonia opacity is significantly less than that at Ka-band. We used a mixture of 85.56% H_2, 9.37% He, and 5.07% NH_3 for the W-band experiment. The W-band experiment took place at a temperature of 210 K in order to avoid condensation. The pressures of the W-band experiments ranged from 1 to 2 atm. These experiments represent the first time that the opacity of gaseous ammonia has been measured under simulated conditions for the Jovian atmospheres at wavelengths less than 1 cm.

2.2.1 Laboratory Configuration

Figures 2.1 and 2.2 show block diagrams of the Ka-band and W-band atmospheric simulators. The components of the simulators may be grouped into the three subsystems: an electrical subsystem, a gaseous pressure subsystem, and a temperature chamber (an ultra-low temperature freezer).

The electrical subsystem of a general millimeter-wave atmospheric simulator is composed of an absorption cell, a millimeter-wave source, and a millimeter-wave receiver. For the Ka-band experiment, the electrical subsystem is a Ka-band Fabry-Perot resonator, a millimeter-wave, swept oscillator (Hewlett-Packard 8690B), and a high resolution spectrum analyzer (Tektronix 7L18). The spectrum analyzer provides the local oscillator (LO) for an external harmonic mixer. The W-band electrical system is similar to the Ka-band system. The source is a power

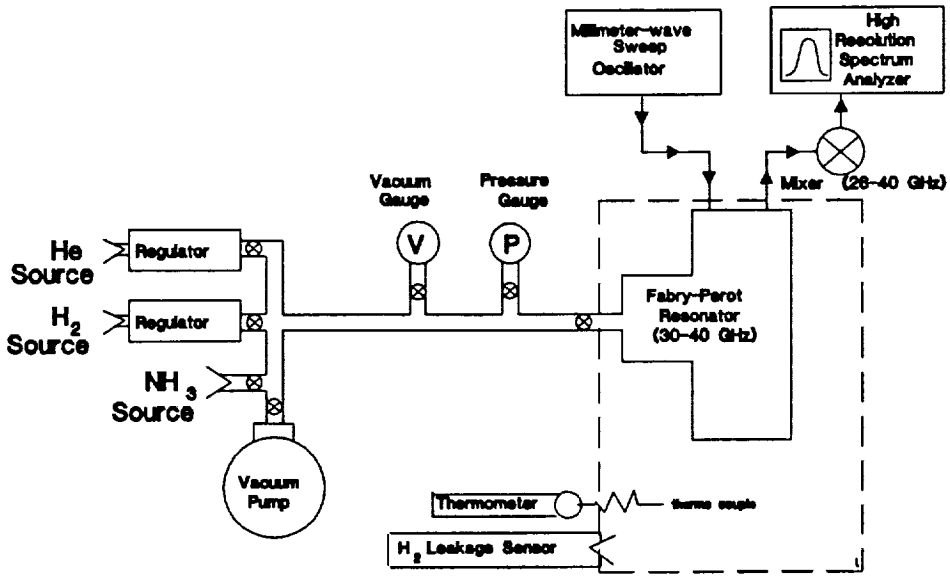

Figure 2.1: Block diagram of the Ka-band atmospheric simulator

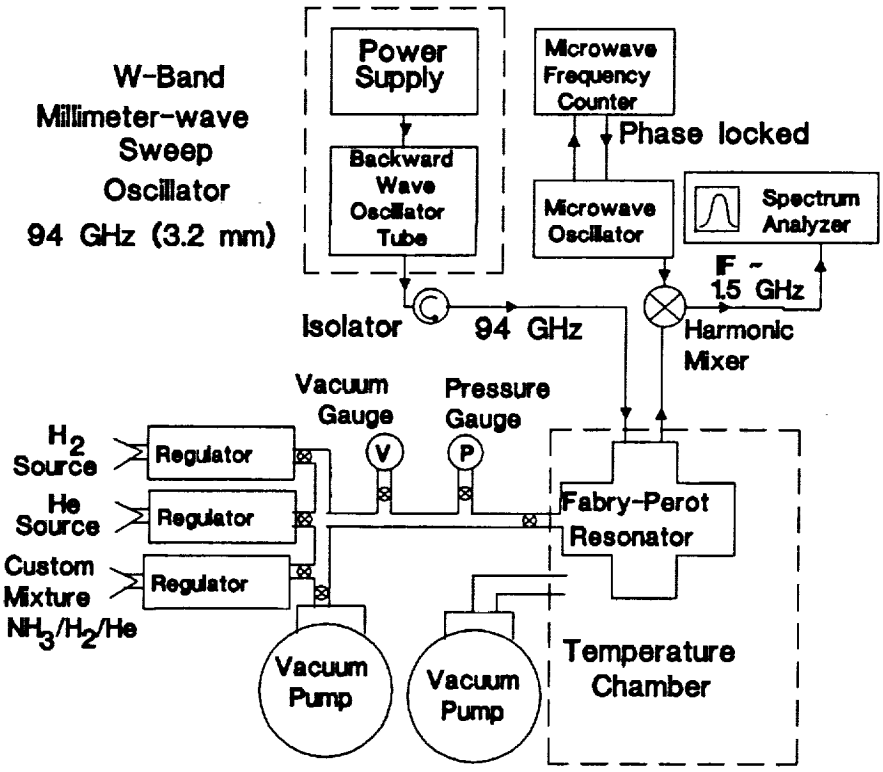

Figure 2.2: Block diagram of the W-band atmospheric simulator

supply (Micro-Now 705B) and backward-wave oscillator (BWO) tube (Micro-Now Model 728 RWO 110) which act together as a millimeter-wave, swept oscillator. The local oscillator (LO) for the harmonic mixer is a microwave source, phased locked to a microwave frequency counter. The mixer combines the tenth harmonic of the LO with the outgoing signal from the resonator. This produces an intermediate frequency (IF) of approximately 1.5 GHz. The high resolution spectrum analyzer displays the IF signal.

The Ka-band Fabry-Perot resonator (shown in Figure 2.3) consists of two gold plated mirrors contained in a T-shaped glass pipe. The mirrors are separated by a distance of approximately 20 cm. The resonator is a semi-confocal configuration in that one mirror is flat and the other is spherical. The resonant frequency can be changed by turning a micrometer connected to the spherical mirror which adjusts the mirror spacing. The quality factor (Q_C) of this resonator is approximately 8000. The W-band Fabry-Perot resonator shown in Figure 2.4 is also semi-confocal. This resonator differs from the Ka-band resonator in that the flat mirror has a much smaller radius (5 cm) than the spherical mirror (11.5 cm). The two mirrors are separated by a distance of approximately 14 cm. This type of configuration yields superior focusing which results in a high quality factor (Q_C) of the resonator (approximately 25,000). The W-band resonator is contained in a cross shaped glass pipe with the curved mirror resting on two fixed support arms. The fixed arms can be adjusted in order to change the distance between the mirrors without disturbing the sensitive alignment. Any adjustments to the mirror spacing and alignment takes place before the resonator is placed in the temperature chamber.

The mirrors were originally constructed of aluminum with a thin layer of gold sputtered on the surface of the mirrors in order to minimize resistive losses. After several sets of experiments, we noted a degradation in the quality factor (Q_C) of the resonator. An inspection of the resonator revealed that ammonia had reacted

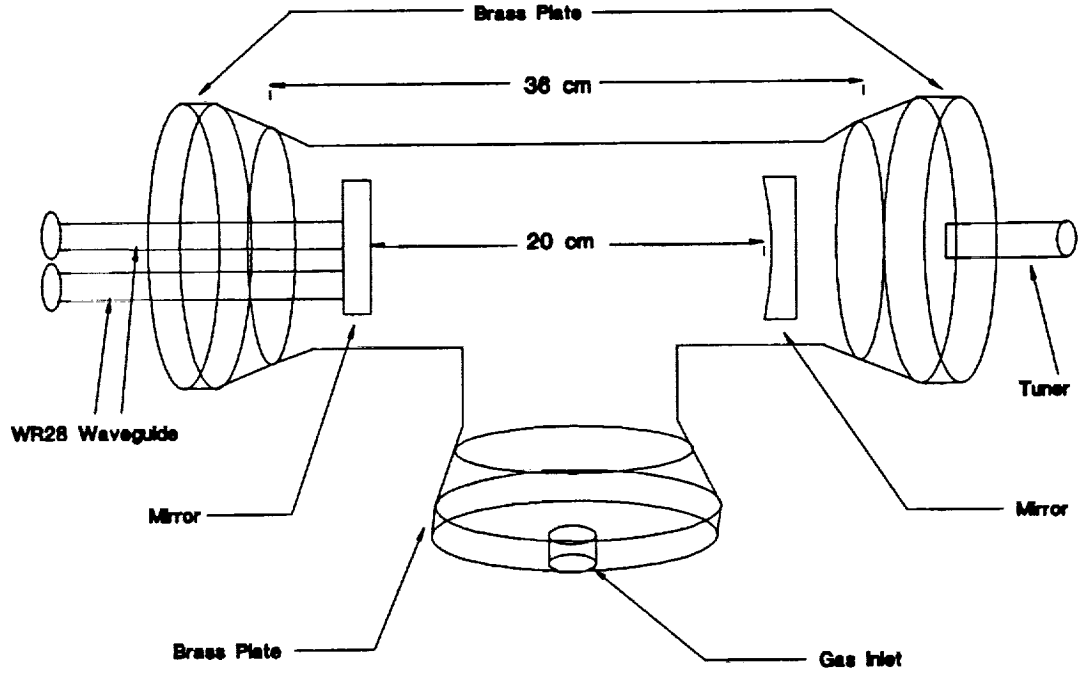

Figure 2.3: Sketch of the Ka-band Fabry-Perot resonator

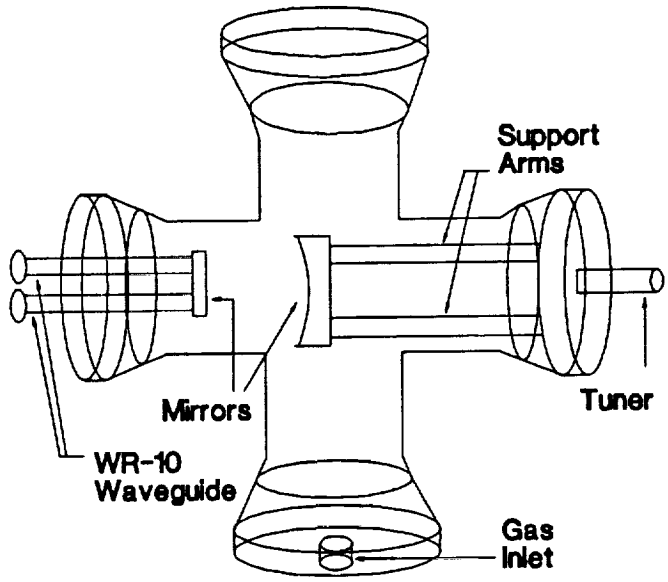

Figure 2.4: Sketch of the W-band Fabry-Perot resonator

with the aluminum. This reaction caused the gold to peel off the surface of the mirrors. In order to correct this problem, the mirrors were refabricated using brass and sputtered with gold.

The Fabry-Perot resonator operates as a band pass filter at each resonance. The millimeter-wave sweep oscillator is adjusted for each resonance so that it sweeps through the entire frequency range affected by that resonance. We measure the band width of each resonance with the high resolution spectrum analyzer. Electromagnetic energy is coupled both to and from the resonator through twin irises located on the flat mirror. The irises are attached to two sections of rigid waveguide which are sealed with rectangular pieces of mica held in place by a mixture of rosin and beeswax. Flexible Ka-band waveguide and rigid W-band waveguide connect the resonator (inside the temperature chamber) to the sweep oscillator and mixer (outside the temperature chamber) through a small hole in the temperature chamber.

The gaseous pressure subsystem consists of the cylinders containing the various gases used in the experiments (H_2, He, NH_3, and custom mixtures), two oil diffusion vacuum pumps, a thermocouple vacuum gauge tube (0-27 torr), a positive pressure gauge (0-100 PSIG), and a glass pipe which contains the resonator. Each of the open ends of the pipe is sealed with an O-ring sandwiched between the glass lip and a flat brass or aluminum plate which is bolted to an inner flange. A network of 3/8" stainless steel tubing and valves connects the components of the pressure subsystem, so that each component may be isolated from the system as necessary (see Figures 2.1 and 2.2). When properly secured, the system is capable of containing two atmospheres of pressure without detectable leakage.

Precautions have been taken to allow for the proper ventilation of the hydrogen and ammonia gas so that the experiment can take place indoors. We use a flammable gas detector to detect any leaks during the experiment. All gases are released outdoors through a vent pipe where they are safely diluted by air.

2.2.2 Experimental Approach

The Fabry-Perot resonator provides the sensitivity needed to measure the millimeter-wave aborptivity of gaseous NH_3. For a Fabry-Perot resonator or interferometer, the quality factor of a resonance (loaded or unloaded) is expressed by

$$Q_C \simeq \frac{2\pi d}{\kappa\lambda}, \tag{2.12}$$

(see, *e.g.*, Valkenburg and Derr, 1966) where λ is the wavelength of the resonance, d is the mirror spacing, and κ represents the total loss of the resonator per reflection. The total loss includes coupling loss, mirror loss, diffraction loss, and any loss due to absorbing material in the resonator. The effective path length (EPL) for electromagnetic energy in the resonator is the ratio of d to κ or

$$\text{EPL} \simeq \frac{Q_C\lambda}{2\pi}. \tag{2.13}$$

The addition of a lossy material in the resonator increases κ which results in a reduced path length. The effective path length (unloaded) for both experiments was approximately 10 m.

The quality factor (Q_C) of a resonance is equal to the ratio of the energy stored in the resonator to the energy lost per radian. The quality factor of a cavity resonance in general is

$$Q_C = \frac{f_C}{\text{BW}}, \tag{2.14}$$

(see, *e.g.*, Terman, 1943) where f_C is the center frequency of the resonance and BW is its full-width half-power band width. The quality factor of a resonance when the cavity is filled or loaded with a test gas (Q_{C_L}) is

$$\frac{1}{Q_{C_L}} = \frac{1}{Q_{C_V}} + \frac{1}{Q_g}, \tag{2.15}$$

(Collin, 1966) where Q_{C_V} is the quality factor of the resonance when the cavity is evacuated, and Q_g is the quality factor of the gas. Combining Equations 2.8, 2.11,

and 2.15 yields

$$\alpha \simeq (Q_{C_L}^{-1} - Q_{C_V}^{-1})\frac{2\pi}{\lambda} \quad \text{cm}^{-1}, \tag{2.16}$$

where α is the absorption coefficient in cm^{-1} (optical depths/cm, 4.343 dB = 1 optical depth), and λ is the wavelength (in cm) of the test signal in the NH_3 mixture.

Equation 2.16 can be simplified if the percentage change in the center frequency of the loaded (f_{C_L}) and unloaded (f_{C_V}) resonances is small. For our experiments, the percentage change is approximately 0.3%. Assuming that $f_{C_L} = f_{C_V}$ and utilizing Equation 2.11, Equation 2.14 can be rewritten simply as

$$\alpha \simeq (\text{BW}_{C_L} - \text{BW}_{C_V})\frac{2\pi}{c} \tag{2.17}$$

or

$$\alpha \simeq 2.096 \times 10^{-4}(\Delta\,\text{BW}) \quad \text{cm}^{-1} = 90.96(\Delta\,\text{BW}) \quad \text{dB/km}, \tag{2.18}$$

where c is the speed of light, and Δ BW is the change in band width of the loaded and unloaded resonances in MHz.

The following procedure is used to measure the unknown quantities in Equations 2.17 and 2.18: First, we measure the unloaded band width (BW_{C_V}) for each resonance while the cell is evacuated. Next, we add the hydrogen-helium-ammonia mixture to the cell and measure the loaded band width (BW_{C_L}) for each resonance. The total pressure of the gas mixture is reduced by venting, and the measurements are repeated. Using this approach insures that the same mixture is used for measurements at all frequencies. Thus, even though some uncertainty exists in the mixing ratio and total pressure, the uncertainty for the frequency dependence of the millimeter-wave absorption is due only to the accuracy limits of the absorptivity measurements.

The dielectric properties of non-absorbing gases such as hydrogen and helium can cause changes in the apparent bandwidths of resonances. The velocity (v) of electromagnetic energy is dependent on the dielectric constant of the medium

through which it travels since $v = (\mu\epsilon)^{-(1/2)}$. When hydrogen and helium are added to an evacuated resonator, a slight change occurs in the velocity or wavelength of the electromagnetic radiation. This slight change in wavelength can result in a change in coupling and a corresponding change in the quality factor or band width of a resonance. Because the percentage change in band width due to the absorption of NH_3 is relatively small for our system (approximately 20%), any changes in band width due to the dielectric effects of hydrogen and helium may lead to significant errors in the absorption measurement.

The resonator, which operates as a band pass filter, is connected to a signal source (the millimeter-wave sweep oscillator) and to a receiver (the high resolution spectrum analyzer). Coupling between the resonator and the spectrum analyzer or sweep oscillator causes additional energy losses thereby decreasing the quality factor (Q_C) of the resonance. The resonator was designed with minimal coupling in order to maximize Q_C and minimize the variations in Q_C that might result from changes in coupling that occur when gases are introduced into the resonator. The changes in coupling are due to the dielectric constant or permittivity of the test gas mixtures and are not necessarily related to the absorptivity of the gases. Slight imperfections in the waveguide or irises can make the apparent Q_C of the resonator appear to vary with the abundance of lossless gases. We will refer to this effect as *dielectric loading.*

It is necessary to repeat the absorption measurement without the absorbing gas present. The last step in the experimental procedure is to measure the band width of each resonance in a mixture consisting of 90% hydrogen (H_2) and 10% helium (He) with no ammonia present. Since the H_2/He mixture is essentially transparent for the pressures and wavelengths involved, no absorption is expected. If any apparent absorption is detected, dielectric loading (or a change in coupling due to the dielectric properties of the gases) is indicated. As long as the effects of dielectric loading are not time variable, they can be removed by measuring Q_{C_V}

and BW_{C_V} with the non-absorbing gases present, rather than in a vacuum.

We used pre-mixed (custom) constituent analyzed $H_2/He/NH_3$ gas mixtures obtained from a local gas company (Matheson) for both the Ka-band and W-band experiments. The gases can also be mixed in the laboratory using a thermocouple vacuum gauge. The uncertainty in the mixing ratio using the thermocouple vacuum gauge ($\pm 20\%$) is significantly higher than the uncertainty in the custom mixture ($\pm 2\%$). Before we obtained the custom mixture, we conducted one set of experiments at Ka-band using a mixture obtained with the thermocouple vacuum gauge.

To mix the gases with the thermocouple vacuum gauge, the chamber is first completely evacuated, and 28 torr of gaseous ammonia is added to the system. We measure the pressure of the ammonia gas with the high-accuracy thermocouple vacuum gauge. We calibrated our vacuum gauge with a vacuum gauge from the Georgia Tech Microelectronics Research Center (MRC). Because the calibration of our vacuum gauge is based on the specific heat of air rather than ammonia, a conversion factor is needed to convert the gauge reading to actual ammonia gas pressure. We measured this conversion factor and found it to be 0.72 ± 0.05. Therefore, a reading of 20 torr on the vacuum gauge corresponds to approximately 14 torr of actual ammonia gas pressure.

Because the gauge is accurate only at pressures up to 20 torr, the ammonia gas is added in two stages. In order to obtain a total pressure of 28 torr, ammonia gas is initially added to the system until the thermocouple vacuum gauge reading is 20 torr (14 torr of gaseous ammonia). We monitor the refraction due to ammonia gas for this pressure with the spectrum analyzer by measuring the frequency shift of the 39.3 GHz resonance. This frequency shift is approximately one megahertz. The band width change due to the absorption from self-broadened ammonia is negligible during this stage. Additional ammonia gas is then added to the system until the total frequency shift is twice that measured for an ammonia pressure of

14 torr. The resulting total pressure is 28 torr.

At these low pressures, the index of refraction (relative to unity) is proportional to the ammonia gas abundance. Therefore, the ability of the system to accurately measure refractivity can be used to infer the relative NH_3 vapor abundance or pressure. However, it is not possible to use this approach for the accurate determination of absolute NH_3 pressure since accurate refractivity data for the 7.3 to 10 mm wavelength range is not yet available. In fact, by using the thermocouple vacuum gauge, we have measured the density normalized refractivity of gaseous ammonia at 39.3 GHz and it found to be approximately 6.8×10^{-17} N-units/molecule/cm^3. This is approximately 6 times the value at optical wavelengths. The last step in the procedure is to add 1.8 atm of hydrogen (H_2) and 0.2 atm of helium (He) to the system. This results in an ammonia mixing ratio of 0.0185 at a total pressure of 2 atm (14.7 PSIG).

2.2.3 Experimental Uncertainties

Uncertainties in the measurement of the absorption coefficient may be classified into two categories: uncertainties due to instrumental error and the uncertainty due to noise. The uncertainties due to instrumental error are caused by the limited resolution and capability of the equipment used to measure pressure, temperature, and resonant band width. These uncertainties have been significantly reduced so that they are relatively small when compared with the uncertainty due to noise. For instance, proper calibration of the spectrum analyzer has made the uncertainty in the measurement of the resonant band width and center frequency in the absence of noise negligible. The limited ability of the low-temperature chamber to maintain a constant temperature results in temperature variations of only $\pm$ 2.5%.

The largest source of uncertainty due to instrumental error in the past has been associated with the mixing ratio of the gas mixture. The uncertainty in the ammonia mixing ratio due to the thermocouple vacuum gauge is approximately

$\pm$ 20% which results in an NH_3 volume mixing ratio of 0.0185$\pm$ 0.0037. Even though measurements at all frequencies are made with the same mixing ratio and the frequency dependence remains intact, a large uncertainty still remains in the relative amplitude of the measured absorption. This uncertainty has been reduced by using a pre-mixed, constituent analyzed, hydrogen-helium-ammonia atmosphere with a mixing ratio accuracy of better than $\pm$2% or an NH_3 volume mixing ratio of 0.0185 $\pm$ 0.00037.

When the gaseous ammonia is introduced into the resonator and pipes, it adsorbs onto metallic surfaces. When the NH_3 gas is evacuated from the system, the NH_3 desorbs from the metallic surfaces leaving behind a trace amount of the gas. The pungent odor of gaseous NH_3 was indeed present when we disassembled the equipment (especially the stainless steel pipes) months after the experiment. Spilker (1990) points out that the effects and magnitudes of adsorption and desorption are not fully understood and should be considered. Since our pressure vessel is constructed of glass and the mirrors of gold, the end plates (brass and aluminum) and backs of the mirrors are the only surfaces which adsorb NH_3 in the resonator. Adsorption can be a non-trivial effect in low pressure spectroscopic measurements. However, our measurement are made using high pressures. Therefore, the fractional amounts of NH_3 which adsorb and desorb should be small.

The most significant source of uncertainty in the measurement of the absorption coefficient was due to the effects of noise in the system. This electrical noise is displayed by the spectrum analyzer. As a result, the measurement of the band width of a resonance must be accompanied by an error term which is equal to the width of the noise on the spectrum analyzer's display.

In order to reduce the effects of noise, the system sensitivity must be as high as possible. The system sensitivity is defined as the minimum detectable absorptivity. It is dependent on both the quality factor (Q_C) of the resonator and the noise present in the system. The quality factor is inversely proportional to the

energy lost (per cycle) in the resonator. Therefore, reducing losses in the resonator increases the sensitivity of the system. The loss in a Fabry-Perot type resonator can be attributed to three sources (Collin, 1966): resistive loss on the surfaces of the mirrors, coupling loss due to energy coupling out of the resonator through the irises, and diffraction loss around the sides of the mirrors.

Computation of the resistive losses resulting from the gold surface of the mirrors showed that (in the absence of all other losses) the quality factor of the Ka-band resonator should have been approximately 250,000. However, its actual quality factor was approximately 10,000. The limiting factor in the performance of the resonator is attributed to either coupling losses or diffraction losses. In order to minimize the coupling losses, adjustable irises were developed so that the smallest possible coupling losses would occur, while still allowing sufficient signal coupling in and out of the resonator. However, this yielded only slightly improved results.

The major limiting factor to the system sensitivity is diffraction losses around the edges of the mirrors. One approach used to reduce diffraction losses involves the precise alignment of the mirrors. We aligned the mirrors by directing the beam of a helium-neon laser through the input waveguide and iris and into the resonator. We adjusted the spherical mirror so that the reflected beam focuses precisely on the output iris. We found that this increased both the signal to noise ratio and the Q_C of the resonator and therefore increased the sensitivity of the system. We used this technique to improve the Q_C of the Ka-band system. We could not use this technique for the W-band experiment due to curvature in the waveguide leading to the resonator. Fortunately, the Q_C of the W-band system was already high enough to provide the needed sensitivity and no major adjustments were necessary.

2.2.4 Theoretical Characterization of Ammonia Absorption

The ammonia molecule (NH_3) forms a tetrahedral shape as shown in Figure 2.5. The nitrogen atom vibrates around a stable position along an axis perpendicular to the plane of the hydrogen atoms. Quantum mechanics predicts that the nitrogen atom will tunnel through the plane of the hydrogen atoms to a stable point on the other side of the plane. This type of vibrational transition is known as *inversion.* Although most vibrational transitions occur in the infrared, the ammonia inversion is slowed by a peak in the potential well of the molecule which occurs as the nitrogen atom passes through the plane of the hydrogen atoms. This causes the transition to occur at microwave frequencies (Townes and Showlow, 1955). The inversion is coupled with rotational transitions in the molecule producing over one hundred individual absorption lines centered around the main inversion frequency of 23 GHz (1.3 cm). Under pressure, collisions with other molecules cause broadening of the individual lines. At pressures of tens of torr, the lines are broadened to such an extent that they overlap and form one continuous peak, obscuring the individual lines.

The rotational state of a molecule is specified by two quantum numbers: J represents the total angular momentum which is quantized in units of the ground state angular momentum so that it must take on positive values; K represents the projection of the total angular momentum vector onto the molecular symmetry axis so that $K \leq J$. In general, the absorption coefficient of gaseous ammonia (α_{NH_3}) is expressed as a summation over all of the rotational states:

$$\alpha_{NH_3}(\nu) = C \sum_{J=0}^{\infty} \sum_{K=1}^{J} A(J,K) F(J,K,\gamma,\nu,\nu_o) \ \ \mathrm{cm}^{-1}, \tag{2.19}$$

where ν is frequency, γ is the pressure-broadened line width, and ν_o is center frequency of the (J,K) transition. The summation is evaluated for $J = 0, 1, .., 16$. Each combination of (J,K) corresponds to a unique absorption line which results

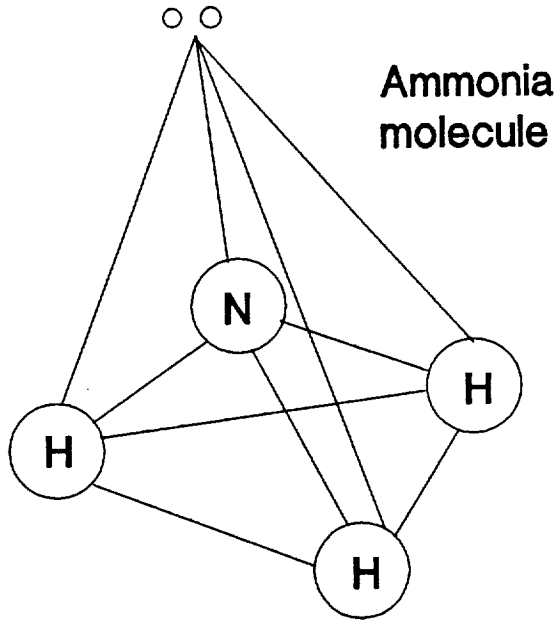

Figure 2.5: Sketch of the ammonia (NH_3) molecule

from the inversion of ammonia molecules in the (J,K) rotational state. An empirical correction factor, C, can be applied to bring the theory into agreement with laboratory data. The line intensity A can be calculated theoretically from

$$A(J,K) = 1.214\frac{(2J+1)K^2}{J(J+1)}\nu_o^2(J,K)S(K)\frac{P_{NH_3}}{T^{7/2}}e^{4.8/T[1.09K^2-2.98J(J+1)]}, \quad (2.20)$$

(*e.g.*, Berge and Gulkis, 1976) where ν_o(J,K) is the center frequency of the (J,K) transition, γ is the pressure broadened line width, T is the temperature in kelvins, P_{NH_3} is the partial pressure of NH_3 gas in bar, S(K) = 3 for K a multiple of 3, and S(K) = 1.5 otherwise.

The frequency dependent part of the absorption coefficient, $F(J,K,\gamma,\nu,\nu_o)$, is known as the line shape. Several different theories have been used to describe the line shape of collision or pressure broadened absorption lines. The Van Vleck-Weisskopf (1945) is

$$F(\nu,\gamma,J,K) = \left(\frac{\nu}{\nu_o}\right)^2 \cdot \left[\frac{\gamma}{(\nu-\nu_o)^2+(\gamma)^2} + \frac{\gamma}{(\nu+\nu_o)^2+(\gamma)^2}\right], \quad (2.21)$$

where ν is frequency, ν_o is the center frequency of the (J,K) transition, and γ is the line width of that transition. The Van-Vleck Weisskopf line shape is known to be accurate at low pressures (less than 1 atm). Zhevakin and Naumov (1963) derived a different line shape and found that their line shape gave better results than the Van Vleck-Weisskopf theory when applied to atmospheric water vapor absorption measurements. This line shape was also derived independently by Gross (1955) and is sometimes referred to as the kinetic line shape. Its spectral shape is

$$F(\nu,\gamma,J,K) = \left(\frac{\nu}{\nu_o}\right)\frac{4\,\nu\,\nu_o\gamma}{\left(\nu_o^2-\nu^2\right)^2+4\nu^2\gamma^2}. \tag{2.22}$$

Ben-Reuven (1966) derived a more comprehensive line shape which was found to be more accurate at higher pressures. His line shape is

$$F(J,K,\gamma,\varsigma,\delta,\nu,\nu_o) = 2\left(\frac{\nu}{\nu_o}\right)^2\frac{(\gamma-\varsigma)\nu^2+(\gamma+\varsigma)\left[(\nu_o+\varsigma)^2+\gamma^2-\varsigma^2\right]}{\left[\nu^2-(\nu_o+\delta)^2-\gamma^2+\varsigma^2\right]^2+4\nu^2\gamma^2}, \tag{2.23}$$

where ς is a coupling element, and δ is a pressure shift term. This line shape reduces to the other line shapes under certain conditions. If $\varsigma = 0$ and $\delta = 0$, then the Ben-Reuven line shape is equal to the Van-Vleck Weisskopf line shape. If $\gamma = \varsigma$ and $\delta = 0$, the Ben-Reuven line shape is equal to the kinetic line shape.

Berge and Gulkis (1976) have developed a formalism for computing the absorption from ammonia in a hydrogen-helium atmosphere. This formalism employs the Ben-Reuven (1966) line shape with the parameters defined as follows:

$$\gamma(J,K) = 2.318P_{H_2}\left(\frac{300}{T}\right)^{2/3}+0.79P_{He}\left(\frac{300}{T}\right)^{2/3}+0.75P_{NH_3}\left(\frac{300}{T}\right)\gamma_o(J,K), \tag{2.24}$$

$$\varsigma(J,K) = 1.92P_{H_2}\left(\frac{300}{T}\right)^{2/3}+0.3P_{He}\left(\frac{300}{T}\right)^{2/3}+0.49P_{NH_3}\left(\frac{300}{T}\right)\gamma_o(J,K), \tag{2.25}$$

and

$$\delta = 0.45P_{NH_3}. \tag{2.26}$$

where P_{H_2}, P_{He}, and P_{NH_3} are the partial pressures of hydrogen, helium, and ammonia in bar, and the units of γ, ς, and δ are GHz. This formalism utilizes a

correction factor (C) in Equation 2.19

$$C = 1.0075 + 0.0304\left(\frac{P_{NH_3}}{T}\right) + 0.0537\left(\frac{P_{H_2}}{T}\right)^2 \tag{2.27}$$

in order to be consistent with the laboratory results of Morris and Parsons (1970), who measured NH_3 absorption at 9.58 GHz in a high pressure H_2/He atmosphere at room temperature.

Recently, Spilker (1990) has derived new pressure and temperature dependencies for the Ben-Reuven line shape based on high accuracy laboratory measurements under simulated Jovian conditions from 9-18 GHz. However, the extrapolation of this formalism to different pressures and frequencies can produce unreliable results.

We have modified the parameters of the Ben-Reuven line shape in order to be compatible with the results of this work as well as the work of Morris and Parsons (1970), Steffes and Jenkins (1988), and Spilker (1990). This formalism employs the Ben-Reuven line shape as described above with the pressure-broadened line width and coupling element given by

$$\gamma(J,K) = 1.69P_{H_2}\left(\frac{300}{T}\right)^{2/3} + 0.75P_{He}\left(\frac{300}{T}\right)^{2/3} + 0.6P_{NH_3}\left(\frac{300}{T}\right)\gamma_o(J,K) \tag{2.28}$$

and

$$\varsigma(J,K) = 1.35P_{H_2}\left(\frac{300}{T}\right)^{2/3} + 0.3P_{He}\left(\frac{300}{T}\right)^{2/3} + 0.2P_{NH_3}\left(\frac{300}{T}\right)\gamma_o(J,K), \tag{2.29}$$

respectively, where the units of γ and ς are GHz. The pressure shift term, δ, is the same as that of the Berge and Gulkis (1976) formalism (Equation 2.26). The correction term (C) used in this formalism is equal to 1. Our formalism differs only from the Berge and Gulkis formalism.

Figure 2.6 shows a graph of the four theoretical formalisms which are used to compute ammonia absorption from 1 mm to 10 cm. The center frequencies, ν_o, and self-broadened line widths, γ_o, of the ammonia inversion resonances used in all calculations are from Poynter and Kakar (1975).

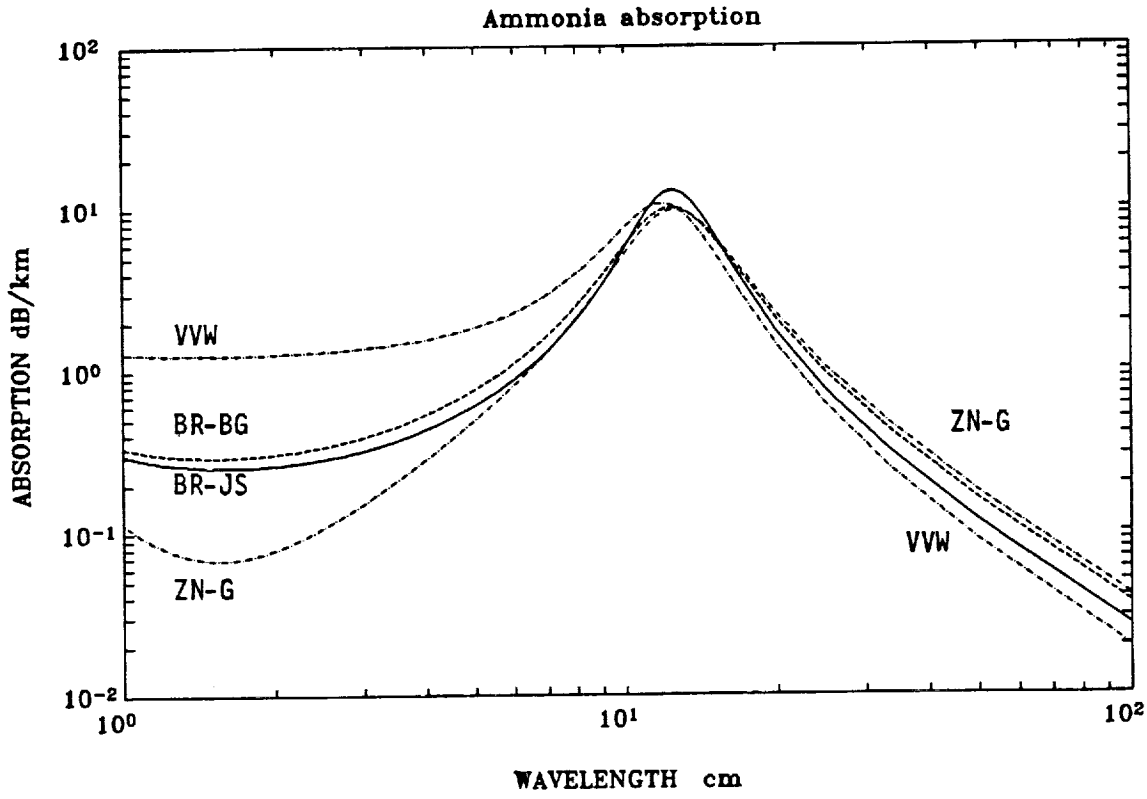

Figure 2.6: Theoretically computed ammonia absorption for 90% H_2, 10% He, and 0.025% NH_3, at 2 bars, and 200 K using the Van Vleck Weisskopf lineshape (VVW), Ben-Reuven lineshape as per Berge and Gulkis (BR-BG), Ben-Reuven formalism as given in this paper (BR-JS), and Zhevakin-Naumov or Gross lineshape (ZN-G)

The absorption from the pressure-broadened submillimeter rotational lines of NH_3 is significant at millimeter wavelengths. The absorption from the submillimeter lines is expressed by Equation 2.19 for $J = 0, 1$ with

$$A(J,K) = 1.826\ \nu_o(J,K)\frac{P_{NH_3}}{T^{7/2}}B(J,K), \tag{2.30}$$

where

$$B(0,0) = 0.070(1 - e^{-28.6/T}), \tag{2.31}$$

$$B(1,0) = 0.075(1 - e^{-57.2/T})e^{-28.6/T}, \tag{2.32}$$

and

$$B(1,1) = 0.053(1 - e^{-57.2/T})e^{-23.3/T}. \tag{2.33}$$

(de Pater and Massie, 1985). We use the kinetic line shape for $F(J,K,\gamma,\nu,\nu_o)$ and $C = 1$.

2.2.5 Experimental Results and Interpretation

The results of the Ka-band and W-band NH_3 absorptivity measurements are listed in Table 2.1. The theoretically-derived values for the Ben-Reuven, Van Vleck-Weisskopf, and kinetic line shapes are also provided in tabular form.

The Ka-band results are presented graphically in Figure 2.7. Two sets of measurements are shown. One set of measurements was conducted using a premixed, constituent analyzed gas mixture (NH_3 mixing ratio uncertainty = $\pm$ 2% of its value). The gas mixture in the other set of measurements was mixed using the thermocouple vacuum gauge (NH_3 mixing ratio uncertainty = $\pm$ 20% of its value). Also shown in Figure 2.7 are solid lines which represent the theoretically computed absorption using the Van Vleck-Weisskopf line shape (VVW), the Berge and Gulkis (1976) modified Ben-Reuven line shape (BR-BG), our modified Ben-Reuven line shape (BR-JS), and the Zhevakin and Naumov or Gross line shape (ZN-G). The Van Vleck-Weisskopf line shape overstates the opacity of NH_3 by nearly a factor

Table 2.1: Measured and theoretical values of NH_3 absorption

Freq (GHz)	Date	Press. (atm)	α meas. (dB/km)	α ZN/G	α VVW	α BR-BG	α BR-JS
†32.17	6/28/88	2.0	291± 47	290.4	461.6	337.7	321.5
	7/7/88	2.0	246± 45*				
†32.89	6/28/88	2.0	254± 53	266.7	435.0	312.3	292.0
	7/7/88	2.0	210± 54*				
†34.32	6/28/88	2.0	200± 34	226.7	388.6	269.0	244.4
	7/7/88	2.0	146± 34*				
†35.03	6/28/88	2.0	146± 34	209.9	368.6	250.7	225.2
	7/7/88	2.0	146± 36*				
†35.75	6/28/88	2.0	173± 40	194.5	350.0	234.0	208.1
	7/7/88	2.0	137± 45*				
†36.46	6/28/88	2.0	119± 40	180.9	333.5	219.1	193.3
	7/7/88	2.0	146± 34*				
†37.17	6/28/88	2.0	155± 40	168.6	318.4	205.7	180.2
	7/7/88	2.0	146± 47*				
†37.89	6/28/88	2.0	164± 40	157.4	304.5	193.5	168.5
	7/7/88	2.0	137± 34*				
†37.89	6/28/88	2.0	146± 40	147.4	292.0	182.5	158.2
	7/7/88	2.0	100± 34*				
†39.32	6/28/88	2.0	119± 34	138.2	280.5	172.5	148.8
	7/7/88	2.0	109± 34*				
‡94.0	10/20/88	2.0	115±32*	42.3	350.6	117.0	120.8
	10/20/88	2.0	109±32				
‡94.0	10/20/88	1.7	58±30*	30.8	253.9	84.7	87.4
	10/20/88	1.7	36±30				
‡94.0	10/20/88	1.3	0±30*	18.2	148.9	49.7	51.1
‡94.0	10/20/88	1.0	0±30*	10.8	88.3	29.4	30.3
‡94.0	10/22/88	2.0	91±30*	42.3	350.6	117.0	120.8
	10/22/88	2.0	91±30*				

†88.34% H_2/9.81% He/1.85% NH_3, T=203K
‡85.56% H_2/9.37% He/5.07% NH_3, T=210K
*Measurements made with premixed, constituent analyzed mixture

of 2, while the modified Ben-Reuven line shape overstates the opacity of NH_3 by an average of over 40%. At these frequencies, it is not clear which line shape (if any) is most appropriate.

We have further evaluated theoretical line shapes by making use of our measurements at higher frequencies where the line shapes are more distinct. Figure 2.8 shows the results of the 94 GHz experiment as compared to four theoretical line shapes. At this frequency, it is clear that neither the Van-Vleck Weisskopf line shape nor the Gross line shape is appropriate. In Figure 2.9, we show an example of laboratory measurements at centimeter wavelengths by Spilker (1990) compared with our new formalism of the Ben-Reuven line shape. Our new line shape provides a good fit to laboratory measurements under a wide range of temperatures, pressures, and frequencies.

Theory predicts that there should be a smooth transition from the Ben-Reuven line shape to the Van Vleck-Weisskopf or Gross line shape at some low pressure. However, it is not known at what pressure this transition occurs. The sensitivity of the millimeter-wave measurement apparatus used in our experiments is not great enough to measure the absorption of ammonia under Jovian conditions at pressures near or below 1 atm. In fact, we obtained no reliable Ka-band absorption measurements at 1 atm pressure. We obtained one reliable set of W-band measurements at 1 atm pressure. The results are shown in Figure 2.10. Although we measured no significant absorption at 1 atm, the error bars give an upper limit for NH_3 opacity. This upper limit is well below the Van Vleck-Weisskopf theory and more compatible with the Gross line shape at 1 atm. This is most likely due to reduced coupling between individual lines at 1 atm pressure.

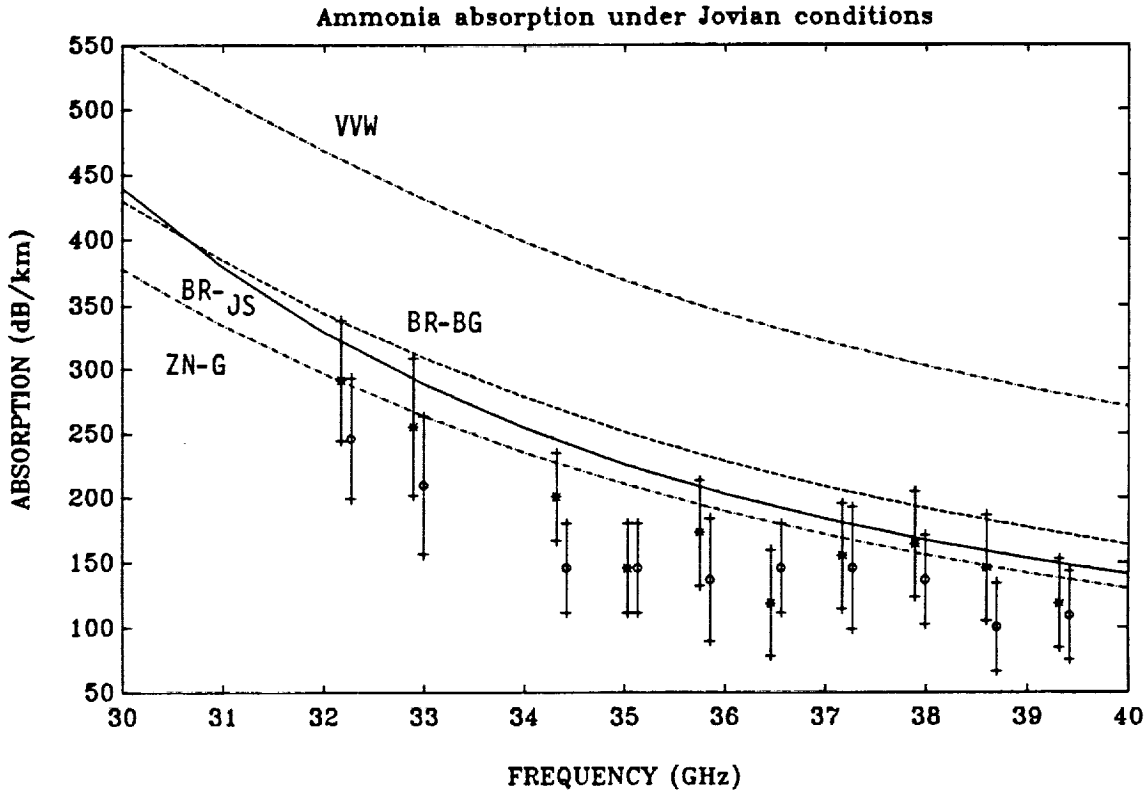

Figure 2.7: Measured and theoretical Ka-band absorption from gaseous NH_3 in an 88.34% H_2-9.81% He-1.85% NH_3 mixture at 210 K and 2 atm. o: Gases mixed with thermocouple vacuum gauge; *: Premixed, constituent analyzed gas mixture.

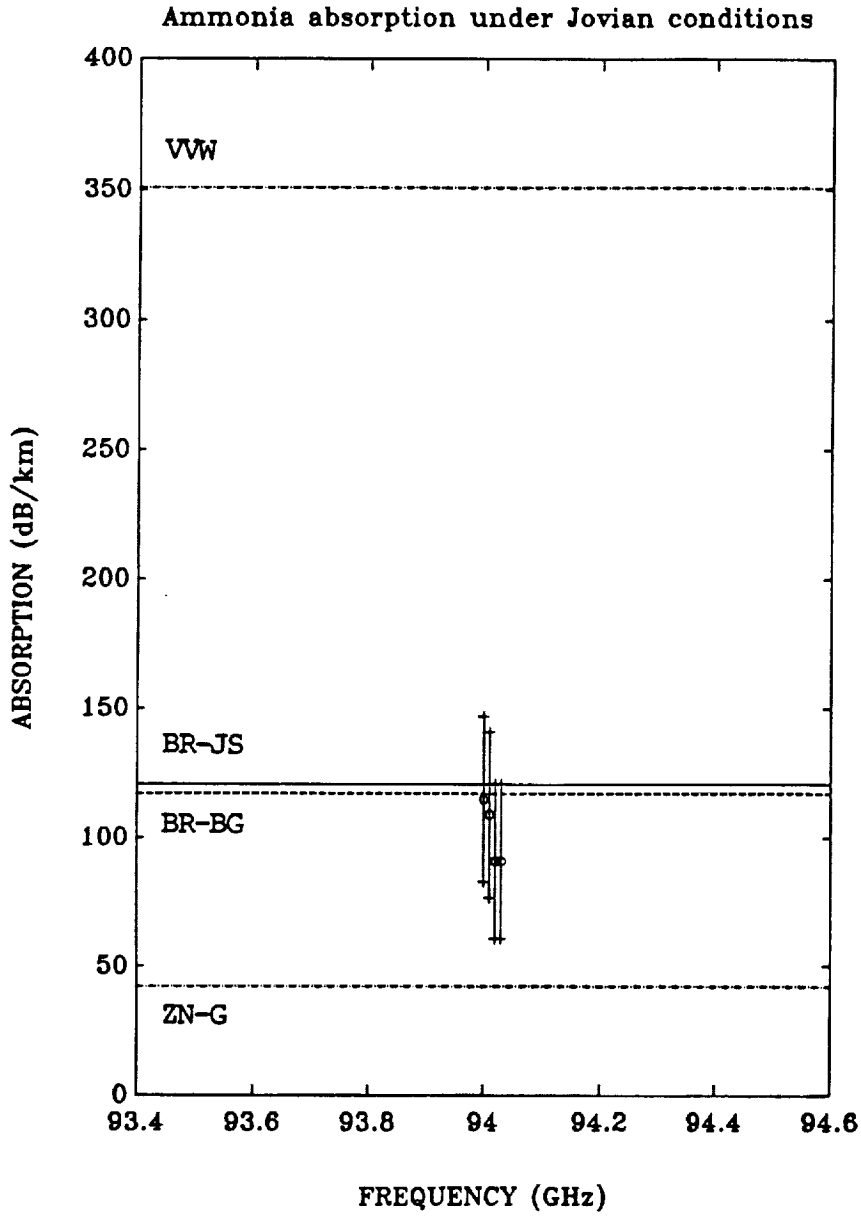

Figure 2.8: Measured and theoretical W-band NH_3 absorption in an 88.56% H_2-9.37% He-5.07% NH_3 mixture at 210 K and at 2 atm

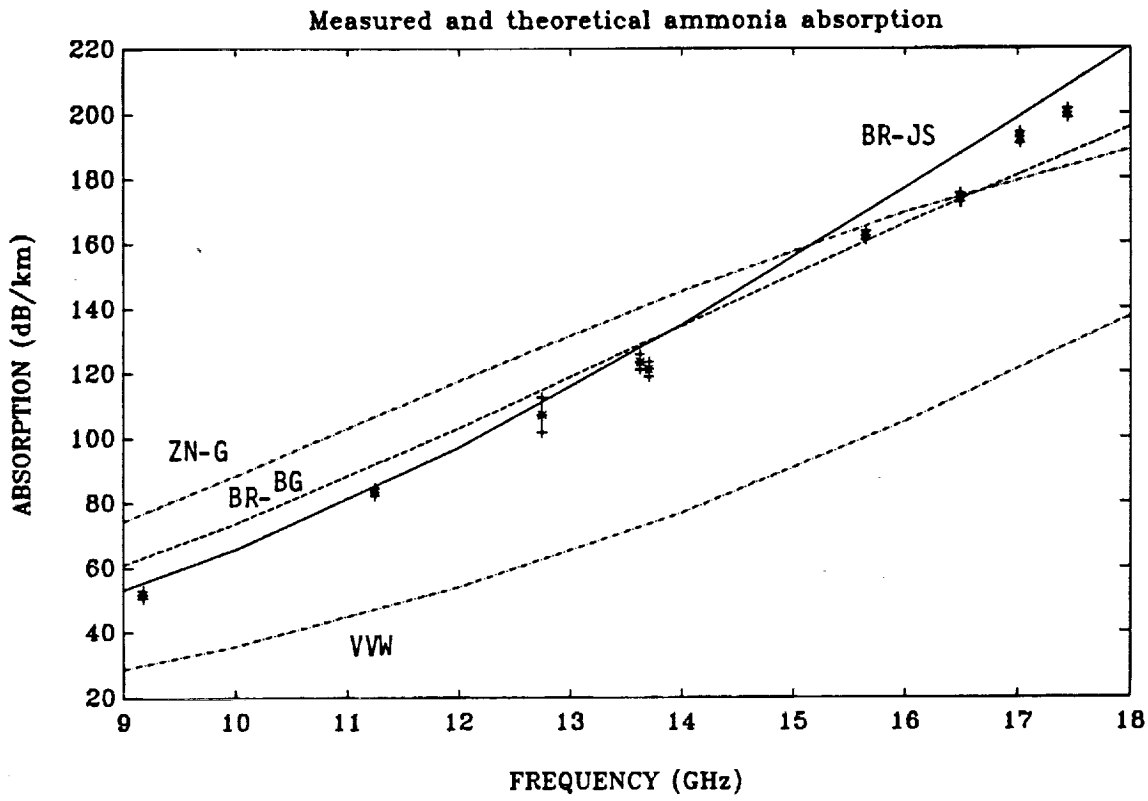

Figure 2.9: Measured (Spilker, 1990) and theoretical NH_3 absorption in an 89.3% H_2, 9.92% He, 0.82% NH_3 mixture at 273 K and at 8 atm)

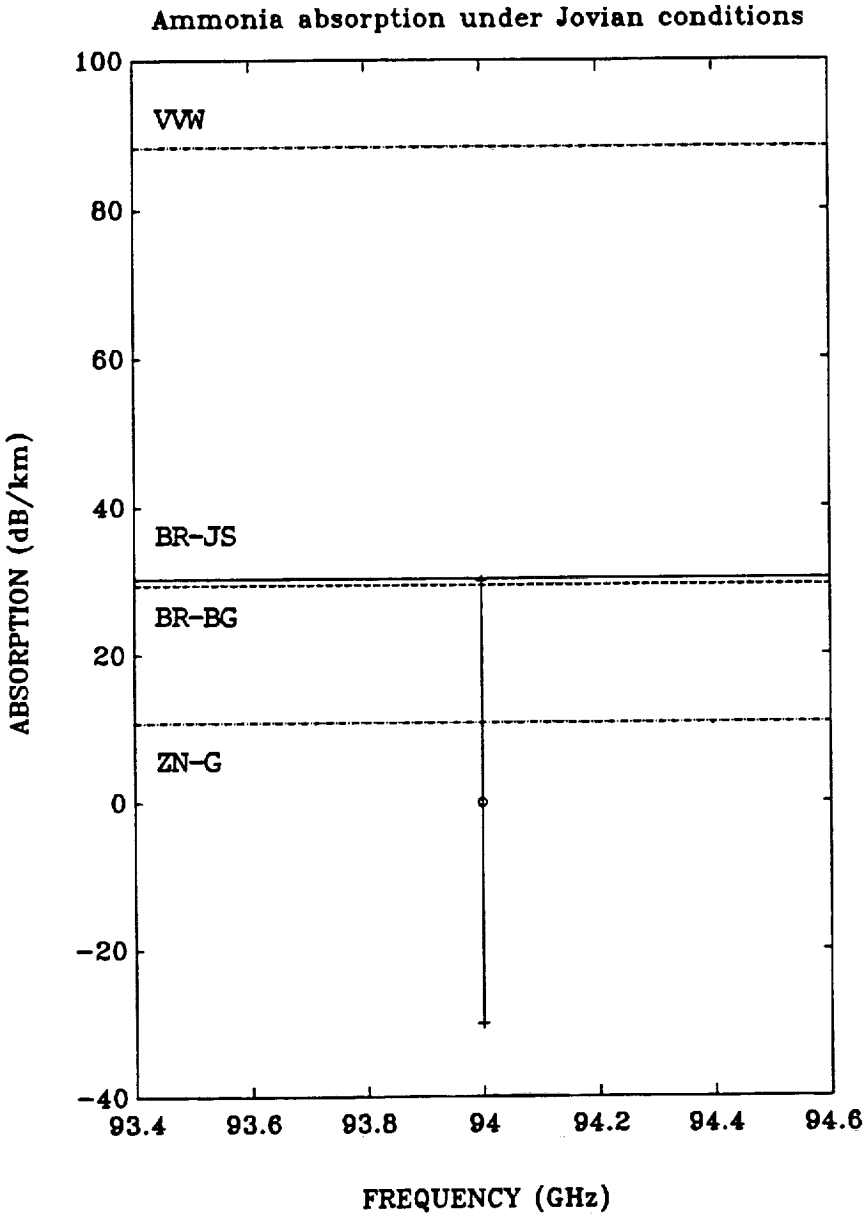

Figure 2.10: Measured and theoretical W-band NH_3 absorption in an 88.56% H_2-9.37% He-5.07% NH_3 mixture at 210 K and at 1 atm

2.3 Measurement of Hydrogen Sulfide (H_2S) Opacity at G-band

Hydrogen sulfide (H_2S) has several strong rotational lines at millimeter wavelengths (168, 217, and 300 GHz). The lines are pressure broadened by H_2 and He in the Jovian atmospheres. We have developed a system capable of measuring pressure-broadening effects of H_2 and He on the $J'_{K'_{-1}K'_{+1}} - J_{K_{-1}K_{+1}} = 2_{0,2} - 2_{1,1}$ line at 217 GHz (1.4 mm). The laboratory configuration, procedure, and results are described in the following sections.

2.3.1 Laboratory Configuration and Procedure

Because gaseous H_2S is extremely opaque near the center of the rotational line at 216.7 GHz, the extended path length provide by a resonator is not needed. Hydrogen sulfide absorption can be measured with a transmission cell, a millimeter wave source, and a detector. A block diagram of the system used to measure H_2S absorption is shown in Figure 2.11. The G-Band CW signal (~218 GHz) is generated by doubling a W-Band (~109 GHz) klystron tube source (Varian, Inc. VAT 692A2). The klystron power supply (Micro-Now Model 756) provides 1 KHz modulation by varying the voltage on the reflector of the klystron. The variation in frequency using this technique is less than 0.5%. Since the pressure-broadened line width of H_2S is several GHz wide, absolute frequency stability is not necessary. The modulation signal incident on the frequency doubler is monitored with an oscilloscope. The klystron signal is sampled with a 20 dB coupler and downconverted to an IF of approximately 800 MHz with a harmonic mixer. A microwave source phase locked to a microwave frequency counter provides the LO for the mixer. The frequency and stability of the IF signal is monitored with a high resolution spectrum analyzer. The klystron frequency can be computed from the precise measurement of the IF and LO frequencies using the spectrum analyzer

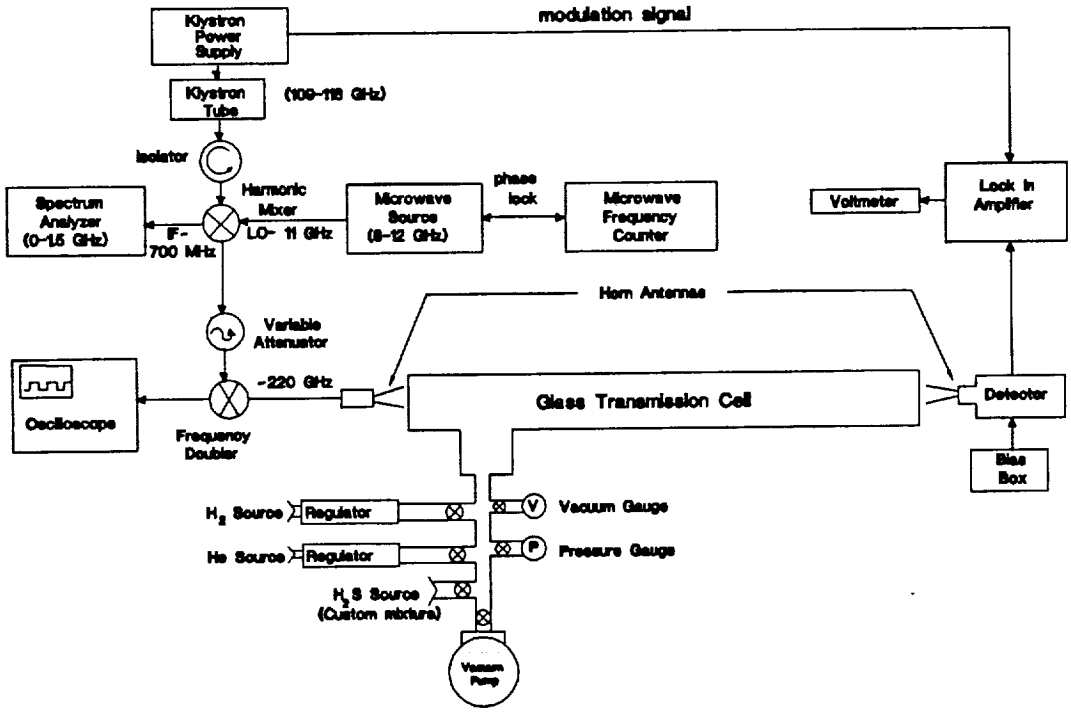

Figure 2.11: Block diagram of a transmission cell for measuring H_2S absorption

and frequency counter.

High gain horn antennas are used to transmit and receive the G-band signal which passes through a 71 cm glass cell. We aligned the antennas with a helium-neon laser. A G-Band square law detector converts the received millimeter-wave signal to a voltage which is measured with a lock in amplifier (Ithaco-Dynatrac 391A). A 5 cm piece of WR-5 waveguide ($f_c = 168$ GHz) acts as a high pass filter to prevent any leakage of the fundamental or first harmonic (~ 109 GHz) through the doubler from being detected. We used a high pass filter ($f_c = 300$ GHz) to

measure the signal level of the third harmonic ($\sim$ 327 GHz). The power from the third harmonic was 30 dB down from the second harmonic. Thus, the detector is measuring power from mostly the desired second harmonic ($\sim$ 218 GHz).

A situation analogous to dielectric loading (described in the previous section) occurs in a transmission cell measurement. Reflections occur at the cell boundaries due to the different dielectric constants of the air outside the cell, gas mixture in the cell, and lenses at the cell boundary. We first measured the power or voltage on the detector with the H_2S mixture in the cell. We then measured the power with a gas mixture of 90% hydrogen and 10% helium in the cell. The indices of refraction for the two gas mixtures (with and without H_2S, respectively) at STP are approximately 1.000183 and 1.000122. Reflections occurring at the cell boundaries should be similar for both gas mixtures. In a less rigorous check, we observed no difference between the signal level measured in the H_2/He mixture and in a mixture of 70% H_2/30% air which has exactly the same index of refraction as the H_2S mixture. The absorption due to the hydrogen and helium mixture is negligible. The attenuation due to the H_2S mixture is computed from the ratio of the voltages measured in the gas mixtures with and without H_2S. This approach ensures that the drop in signal level is due only to absorption and not to changes in reflection at the cell interfaces.

A relatively high mixing ratio of H_2S is needed in order to measure absorption in the cell. The experiments take place at ambient temperature (296 K) and at a total pressure of 2 atm. We used a pre-mixed, constituent analyzed gas mixture (Matheson) in all experiments. This mixture consists of 78.79% H_2, 9.28% He, and 11.93% H_2S.

Because H_2S is an extremely noxious and corrosive gas, various safety precautions are undertaken during the experiment. We used filtered gas masks and safety goggles when handled the gas. All equipment coming in contact with the H_2S is constructed of stainless steel, glass, or plastic. The experiment takes place

indoors in a well ventilated area, and the gases are vented outdoors where they are safely diluted by air.

2.3.2 Experimental Uncertainties

The main source of uncertainty in this experiment is power drift in the klystron source. Power and frequency drifts occur as the temperature of the klystron varies. We found that the klystron output power exhibited a sinusoidal drift even though it was mounted on a large heat sink. The drift period is substantially longer than the time required to make an individual measurement. By obtaining several measurements, we can characterize the drift and minimize this uncertainty. The overall uncertainty in klystron power is approximately ±7%. Other instrumental uncertainties include uncertainty in the measurement of temperature (±1%) and total pressure (±7%). The uncertainty in the mixing ratio of the gas mixture is ±2% per stated component. The total uncertainty in the measured absorption coefficient is the root sum square of the individual uncertainties.

2.3.3 Theoretical Characterization of H_2S Absorption

In general, the opacity from a single absorption line at millimeter wavelengths is expressed by

$$\alpha = N\, S_o \left(\frac{T_o}{T}\right)^{5/2} exp\left[-1.439\, E\, \left(\frac{1}{T} - \frac{1}{T_o}\right)\right] F(\nu, \nu_o, \Delta\nu) \ \ \mathrm{cm}^{-1}, \qquad (2.34)$$

where N is the number density in molecules/cm^3, T is temperature in Kelvins, T_o is a normalizing temperature (296 K), S_o is a normalized line intensity, E is the lower state energy level, and $F(\nu, \nu_o, \Delta\nu)$ is the line shape. The line parameters used in the computation of H_2S absorption are taken from the GEISA (Gestion et Etude des Spectroscopiques Atmospherique) line catalog (Chedin *et al.*, 1982 and Flaud *et al.*, 1983).

The Van-Vleck Weisskopf (1945) line shape used in this calculation is

$$F(\nu,\nu_o,\Delta\nu)=\frac{1}{\pi}\left(\frac{\nu}{\nu_o}\right)\left[\frac{\Delta\nu}{(\nu-\nu_o)^2+(\Delta\nu)^2}+\frac{\Delta\nu}{(\nu+\nu_o)^2+(\Delta\nu)^2}\right], \qquad (2.35)$$

where $\Delta\nu$ is the pressure-broadened line width, and all frequencies are in cm^{-1}. The pressure-broadened line width of H_2S in an H_2-He atmosphere is

$$\Delta\nu=\left(\frac{T}{T_o}\right)^n\left[\Delta\nu_{H_2}P_{H_2}+\Delta\nu_{He}P_{He}+\Delta\nu_{H_2S}P_{H_2S}\right] \qquad (2.36)$$

where $\Delta\nu_{H_2}$, $\Delta\nu_{He}$, and $\Delta\nu_{H_2S}$ are the hydrogen, helium and self-broadened line widths of H_2S. The temperature scaling exponent, n, has not been measured for H_2S. We assume a value of 0.67 for n, based on the values reported for the nitrogen-broadened line width of H_2O at 183 GHz (Waters, 1976). Because our measurements are conducted at room temperature, the assumed value of n does not affect our results. Moreover, the value of n does not significantly affect the line width calculation when temperatures are extrapolated to lower temperatures occurring in Jupiter's atmosphere. For example, changing the value of n to 0.3 (which we estimate to be a lower limit) at 200 K (the temperature near 2 bar on Jupiter) results in a line width difference of less than 20%. Helminger and De Lucia (1977) have measured the self-broadened line widths of the $J'_{K'_{-1}K'_{+1}}-J_{K_{-1}K_{+1}}=2_{0,2}-2_{1,1}$ line at 217 GHz and report a value of $\Delta\nu_{H_2S}=9.10$ MHz/Torr (6.92 GHz/bar). Willey *et al.* (1989) have measured the helium-broadened line width of the $1_{0,1}-1_{1,0}$ hydrogen sulfide transition at 168.8 GHz and 295 K and found it to be 1.60 MHz/Torr (1.22 GHz/Bar). We assume the same value of $\Delta\nu_{He}$ for the $2_{0,2}-2_{1,1}$ transition.

2.3.4 Experimental Results

The measured H_2S absorption at 2 atm and 296 K is shown in Figure 2.12. The solid lines represent the theoretically computed absorption for several values of $\Delta\nu_{H_2}$. Visual inspection of Figure 2.12 suggests a value of $\Delta\nu_{H_2}$ approximately equal to 2 ± 0.5 GHz/Bar (2.6 ± 0.7 MHz/Torr).

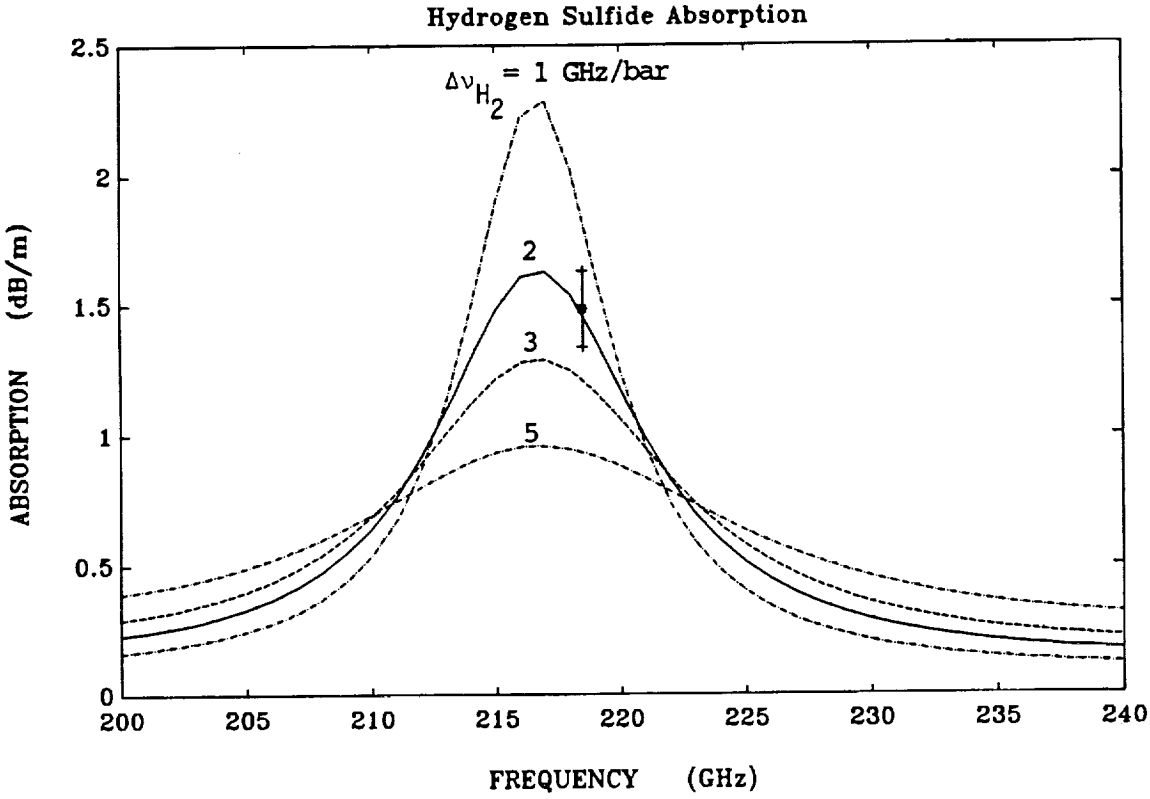

Figure 2.12: Measured and theoretical G-Band absorption from gaseous H_2S in a 78.79% H_2, 9.28% He, 11.93% H_2S mixture at 2 atm and 296 K. Theoretical absorption using the Van Vleck-Weisskopf line shape for various $\Delta\nu_{H_2}$ between 1 and 5 GHz/bar.

CHAPTER 3

Modeling of the Jovian Atmospheres

In the last chapter, we developed formalisms for computing the absorption from gaseous NH_3 and H_2S. In this chapter, we apply the new expressions to a radiative transfer and thermochemical model of the giant planet atmospheres. This chapter begins with an explanation of a thermochemical model which is used to predict the distribution of volatiles (NH_3, H_2S, H_2O, and CH_4) in the giant planet atmospheres. Section 3.2 follows with the theory of radiative transfer as it is used to compute the radio emission from the giant planets. Section 3.3 describes the parameters of the radiative transfer model in detail. In this section, we also develop new expressions for computing the absorption from other opacity sources. In Section 3.4, we adjust the parameters of the radiative transfer and thermochemical models for each the four Jovian planets. Using a forward modeling approach, we compare the modeled emission of each planet with its observed emission.

3.1 Thermochemical Modeling

The composition of the Jovian clouds cannot be readily determined by present observational techniques. However, the composition of clouds can be predicted with thermochemical models. Weidenschilling and Lewis (1973) developed some of the earliest thermochemical models of the giant planets. Their models were based on a solar mix of elements. Recently, thermochemical models have been combined with radiative transfer models and used to predict the emission from

the giant planet atmospheres (see, *e.g.*, Atreya and Romani, 1987 or Briggs and Sacket, 1989). We will use the thermochemical models in a similar approach. We will estimate the distribution of cloud forming constituents in the giant planet atmospheres and use the distributions in a radiative transfer model to predict the radio emission from the giant planets. We will also use the thermochemical models to estimate cloud bulk densities which will be used in the computation of cloud opacity.

The atmosphere in the thermochemical model is composed of discrete homogeneous layers. The thermochemical model begins deep in the atmosphere where a starting temperature and pressure have been previously established (see Section 3.3.1). A step dP is taken, and the average temperature and pressure are computed. A check is made to see if condensation has occurred.

The saturated vapor pressure for a single constituent over a single phase is

$$\ln(P) = \frac{a_1}{T} + a_2 + a_3 \ln(T) + a_4 T + a_5 T^2. \tag{3.1}$$

We use values of the coefficients a_i for liquid and solid NH_3 and H_2O from Briggs and Sacket (1989). The values of a_{1-2} ($a_{3-5} = 0$) for liquid and solid CH_4 are from de Pater and Massie (1985). Although both NH_3 and H_2S dissolve in aqueous H_2O cloud drops, the net effect on the millimeter-wave opacity, latent heat, and depression of the freezing point is small (see, *e.g.*, Grossman, 1990 or Briggs and Sacket, 1989). Therefore, we will consider only a pure H_2O cloud in the thermochemical model. The coefficients a_i for solid H_2S were derived from recent laboratory measurements by Kraus *et al.* (1989).

Gaseous NH_3 and H_2S combine to form solid ammonium hydrosulfide (NH_4SH) in the reaction

$$NH_3(\text{gas}) + H_2S(\text{gas}) \overset{K}{\rightleftharpoons} NH_4SH(\text{solid}), \tag{3.2}$$

where the equilibrium constant K is related to the saturated partial pressures of

NH_3 and H_2S by

$$\ln(K) = \ln(P_{NH_3} P_{H_2S}) = 34.151 - \frac{10834}{T}, \tag{3.3}$$

where P_{NH_3} and P_{H_2S} are the partial pressures of NH_3 and H_2S in bar. The value of K could be overestimated by a factor of 3 in the worst case (de Pater *et al.*, 1989). Therefore, the NH_4SH cloud could form at deeper levels in the atmosphere (higher pressures). Since no additional laboratory data is available at this time, we will use Equation 3.3.

If condensation has occurred, the incremental change in the mixing ratio of the condensate is computed. The mixing ratio or molar concentration (X_k) for an ideal gas is

$$X_k = \frac{P_k}{\overline{P}}, \tag{3.4}$$

where P_k is the partial pressure of gas k, and $\overline{P}$ is the mean pressure. The change in mixing ratio, dX_k, is found by differentiating Equation 3.4:

$$dX_k = \frac{1}{P} dP_k - \frac{P_k}{P^2} dP. \tag{3.5}$$

Substituting the Clausius-Clapeyron equation,

$$\frac{dP}{dT} = \frac{LP}{RT^2}, \tag{3.6}$$

into Equation 3.5 yields

$$dX_k = \frac{L_k P_k}{PRT^2} dT - \frac{L_k P_k}{P^2} dP. \tag{3.7}$$

The incremental change in the mixing ratios of NH_3 and H_2S resulting from the formation of the NH_4SH cloud is

$$dX_{NH_3} = dX_{H_2S} = \left[\frac{P_{NH_3} P_{H_2S}}{P(P_{NH_3} + P_{H_2S})}\right]\left[\frac{10834}{T^2} dT - \frac{2}{P} dP\right]. \tag{3.8}$$

The saturated vapor pressure for a single constituent over a single phase is

$$\ln(P) = \frac{a_1}{T} + a_2 + a_3 \ln(T) + a_4 T + a_5 T^2. \tag{3.9}$$

We use values of the coefficients a_i for liquid and solid NH_3 and H_2O from Briggs and Sacket (1989). The values of a_{1-2} ($a_{3-5} = 0$) for liquid and solid CH_4 are from de Pater and Massie (1985). Although both NH_3 and H_2S dissolve in aqueous H_2O cloud drops, the net effect on the millimeter-wave opacity, latent heat, and depression of the freezing point is small (see, *e.g.*, Grossman, 1990 or Briggs and Sacket, 1989). Therefore, we will consider only a pure H_2O cloud in the thermochemical model. The coefficients a_i for solid H_2S were derived from recent laboratory measurements by Kraus *et al.* (1989).

Gaseous NH_3 and H_2S combine to form solid ammonium hydrosulfide (NH_4SH) in the reaction

$$NH_3(\text{gas}) + H_2S(\text{gas}) \stackrel{K}{\rightleftharpoons} NH_4SH(\text{solid}), \tag{3.10}$$

where the equilibrium constant K is related to the saturated partial pressures of NH_3 and H_2S by

$$\ln(K) = \ln(P_{NH_3} P_{H_2S}) = 34.151 - \frac{10834}{T}, \tag{3.11}$$

where P_{NH_3} and P_{H_2S} are the partial pressures of NH_3 and H_2S in bar. The value of K could be overestimated by a factor of 3 in the worst case (de Pater *et al.*, 1989). Therefore, the NH_4SH cloud could form at deeper levels in the atmosphere (higher pressures). Since no additional laboratory data is available at this time, we will use Equation 3.8.

The cloud density is computed according to Weidenschilling and Lewis (1973)

$$D = 100 \frac{dX_k \, m_k \, \overline{P}^2}{dP \, \overline{T} \, R} \ \text{g/cm}^3 \tag{3.12}$$

where $\overline{P}$ is the mean pressure of the layer in bar, $\overline{T}$ is the mean temperature in kelvins, dP is the difference in pressure between the top and bottom of the layer, dX_k is the change in mixing ratio of condensate k, m_k is the molecular weight of the k_{th} condensate, and R is the universal gas constant. The resulting cloud bulk densities and vertical distributions of the cloud forming constituents are integrated into the radiative transfer model which is described in the following section.

3.2 Theory of Radiative Transfer

In this section, we develop various forms of the radiative transfer equation. The equations are used to compute synthetic brightness spectra of the giant planets. We also explore the potential effect of the oblate shape of the giant planets on their radio emission.

3.2.1 The Radiative Transfer Equation

The Planck radiation law relates the brightness radiated by a black body ($B_\nu(T)$) to its physical temperature (T) in kelvins and frequency (ν) in Hz as follows:

$$B_\nu(T) = \frac{h\nu^3}{c^2[\exp(\frac{h\nu}{kT}) - 1]}, \tag{3.13}$$

where c is the speed of light (2.998×10^{10} cm/s), h is the Planck constant (6.63×10^{-34} J s) and k is the Boltzmann constant (1.38×10^{-23} J/K). The units of $B_\nu(T)$ are watts per square meter per hertz per steradian ($\mathrm{Wm^{-2}Hz^{-1}sr^{-1}}$).

The radiative transfer geometry for a planet is shown in Figure 3.1. The zenith angle, θ, is defined at a given point on a constant pressure surface of the planet. It is the angle between the observer's line of sight to the planet and the local normal to the surface at that point. The quantity μ is the cosine of the zenith angle. The radiative transfer equation gives the total brightness emitted at the top of the atmosphere ($z = 0$) along a ray in the direction μ as follows:

$$B_\nu(T,\mu) = \int_0^\infty B_\nu\big(T(z)\big) \exp\Big(-\int_z^\infty \alpha_\nu(z')\frac{dz'}{\mu}\Big)\alpha_\nu(z)\frac{dz}{\mu}, \tag{3.14}$$

where z is the depth as measured from the top of the planet ($z = 0$), and $\alpha_\nu(z)$ (in optical depths per unit length) is the total absorption coefficient or the sum of all of the absorbing processes at the depth z and at frequency ν. The total brightness can also be expressed in terms of a weighting function, $\mathcal{W}_\nu(z,\mu)$:

$$B_\nu(T,\mu) = \int_0^\infty B_\nu\big(T(z)\big)\mathcal{W}_\nu(z,\mu)\frac{dz}{\mu}. \tag{3.15}$$

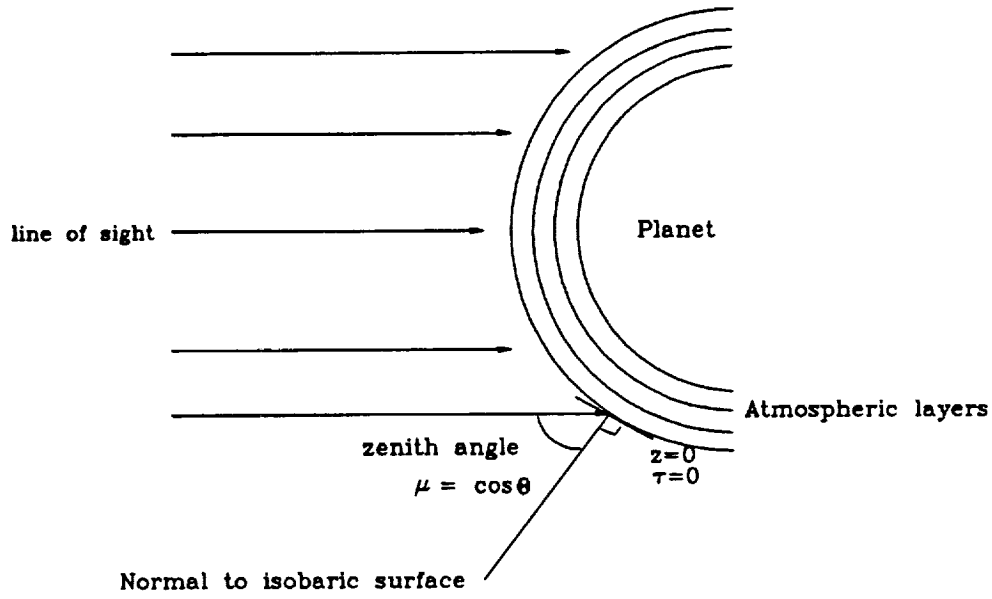

Figure 3.1: Sketch of the zenith angle of a planet.

The weighting function provides a representation of which altitudes are contributing most to the emission at a particular frequency. Another term commonly used in radiative transfer modeling is the vertical optical depth, τ, which is defined as

$$\tau_\nu(z) = \int_0^z \alpha_\nu(z')dz'. \tag{3.16}$$

Substituting Equation 3.13 in Equation 3.11 yields an alternate form of the radiative transfer equation:

$$B_\nu(T,\mu) = \int_0^\infty B_\nu\big(T(\tau)\big)\exp(-\frac{\tau}{\mu})\frac{d\tau}{\mu}. \tag{3.17}$$

The absorption coefficient for gaseous molecules is a function of temperature, pressure, and frequency. The temperature, T, and pressure, P, may be related to depth in the atmosphere, z, by the hydrostatic equation,

$$dP = \rho\, g\, dz, \tag{3.18}$$

and the equation of state,

$$P = \frac{\rho\, T\, R}{\overline{m}}, \tag{3.19}$$

which yields

$$dz = \left(\frac{RT}{mgP}\right) dP, \tag{3.20}$$

where R is the universal gas constant (8.3143×10^7 erg k^{-1} mol^{-1}), $\overline{m}$ is the mean molecular weight of the atmosphere, and g is the acceleration due to gravity. Using Equation 3.17, the absorption coefficient at frequency ν can be written simply as a function of depth z.

The integral over τ in Equation 3.14 is evaluated by modeling the atmosphere as a finite number of discrete layers. The average temperature, pressure, and altitude are specified at each layer. The integration begins at top of the atmosphere (P=10 mbar, $\tau = 0$, $z = 0$) and is terminated when τ reaches a value of $\tau_o = 5$ optical depths:

$$B_\nu(T,\mu) = \sum_{\tau=0}^{\tau_o=5} B_\nu\Big(T(\tau)\Big) \exp(-\frac{\tau}{\mu})\frac{\Delta\tau}{\mu} + B_\nu(T_o)\exp(-\tau_o), \tag{3.21}$$

where the last term is a correction factor which accounts for the brightness contribution from altitudes below the cutoff altitude, τ_o. The correction assumes that the temperature is constant below the cutoff altitude.

Radio astronomical observations of the planets are commonly reported in terms of the temperature of an equivalent blackbody that would produce the observed brightness. This temperature, T_B, is called the brightness temperature. It is found by inverting the Planck function:

$$T_B = \frac{h\nu}{k\, \ln\left(\left[\frac{h\nu^3}{Bc^2}\right] + 1\right)}. \tag{3.22}$$

3.2.2 Disk-averaged Brightness

The disk-averaged brightness of a planet, $B_\nu(T_D)$, results from the integration of Equation 3.11 or 3.14 over all angles of incidence using

$$B_\nu(T_D) = 2\int_0^1 B_\nu(T,\mu)\mu d\mu. \tag{3.23}$$

Combining Equations 3.14 and 3.20, the disk-averaged brightness is expressed by

$$B_\nu(T_D) = 2\int_0^1 \int_0^\infty B_\nu\big(T(\tau)\big)\exp(-\frac{\tau}{\mu})d\tau\ d\mu. \tag{3.24}$$

Spherical Approximation

If the shape of the planet is a sphere, the integral over μ may be simplified to a single integral (Goodman, 1969) by making use of the exponential integrals of the form

$$E_n(\tau) = \int_1^\infty \frac{1}{y^n} e^{-\tau y} dy. \tag{3.25}$$

Substituting $y = 1/\mu$, Equation 3.21 becomes

$$B_\nu(T_D) = 2\int_0^\infty B_\nu\big(T(\tau),\mu\big)E_2(\tau)d\tau \tag{3.26}$$

or

$$B_\nu(T_D) = -2\int_{\tau=0}^\infty B_\nu\big(T(\tau),\mu\big)dE_3(\tau). \tag{3.27}$$

The exponential integral is evaluated numerically.

Oblate Grid Model

In order to test the spherical approximation, the integral over μ in Equation 3.20 can be evaluated by constructing a grid of the projection of the planet against the sky. The grid is made up of a finite number of rectangular elements which form the oblate shape of the planet. A grid of Jupiter is shown in Figure 3.2. The grid is more finely spaced at the edges of the planet where the limb darkening is greatest. The brightness temperature is computed at each point (from Equations 3.11 or 3.14) and weighted according to the fractional area which it covers on the projection. The disk-averaged brightness is the weighted sum of the brightness over all elements:

$$T_B(\text{disk} - \text{averaged}) = \frac{\int_x \int_y \mathrm{T_B(x,y)dx\ dy}}{\int_x \int_y \mathrm{dx\ dy}}. \tag{3.28}$$

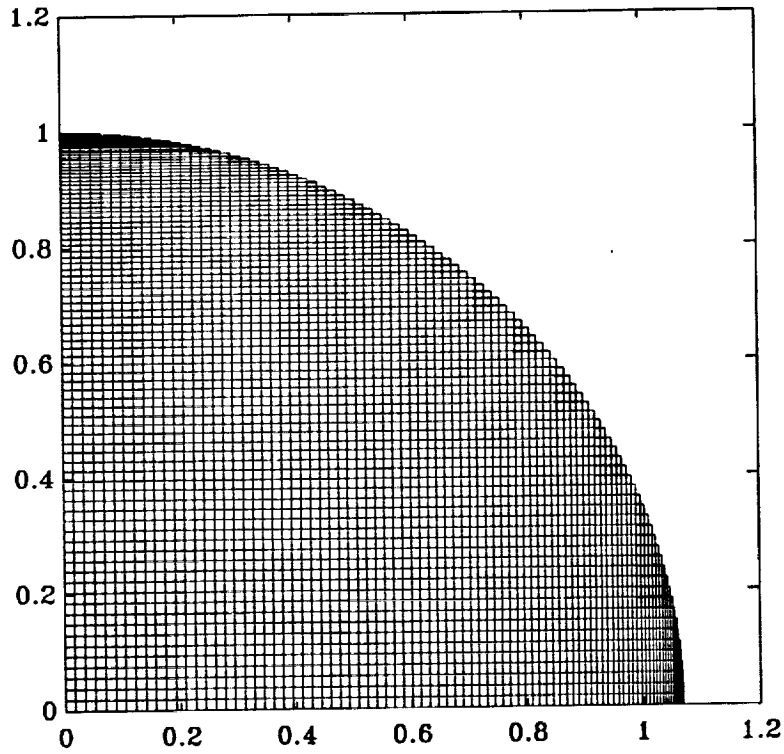

Figure 3.2: Grid of Jupiter.

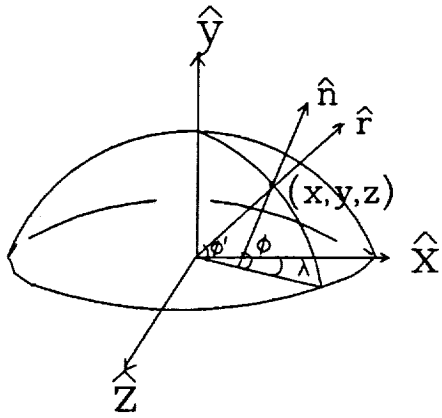

Figure 3.3: Geometry of an oblate spheroid.

The grid coordinate system is shown in Figure 3.3. The disk of the planet is projected onto the ($\hat{x}$,$\hat{y}$) plane. The line of sight from the observer to the planet is in the direction $\hat{z}$. Each (x,y,z) refers to the coordinate of a point on the surface of the planet that is projected onto the ($\hat{x}$,$\hat{y}$) plane.

The surface or radius of a Darwin-de Sitter spheroid is a function of the planetocentric latitude ϕ' (Zharkov and Trubitsyn, 1978):

$$r(\Phi) = 1 + b_0 + \sum_{i=1}^{\infty} b_{2i} P_{2i}\Big(cos(\Phi)\Big), \tag{3.29}$$

where P_{2i} is the Legendre polynomial of degree $2i$, b_{2i} are coefficients which are related to the zonal harmonic coefficients J_{2i}, and

$$\Phi = \frac{\pi}{2} - \phi', \tag{3.30}$$

The planetographic latitude, ϕ is related to the planetocentric latitude ϕ' by

$$\phi = \phi' + arctan\Big(\frac{dr(\Phi)}{r\ d\Phi}\Big). \tag{3.31}$$

The planetocentric longitude, λ, is

$$\lambda = arctan\left(\frac{z}{x}\right) \tag{3.32}$$

and

$$z = \sqrt{(r(\phi)\ sin\Phi)^2 - x^2}. \tag{3.33}$$

The 1 bar surfaces of Jupiter and Saturn are shown in Figure 3.4. For Uranus and Neptune, the ellipticity is less than 2%.

The value of Φ at the surface of the planet for a point (x, y) on the projection can be computed using Newton's method

$$\Phi_{n+1}(y, b_{2i}) = \Phi_n - \frac{r(\Phi_n)cos(\Phi_n) - y}{dr(\Phi_n)cos(\Phi_n) - r(\Phi_n)sin(\Phi_n)}. \tag{3.34}$$

The cosine of the angle between the line of sight ($\hat{z}$) and the local vertical or normal ($\hat{n}$) is equal to μ for a sphere as well as an oblate spheroid:

$$\mu = \hat{n} \cdot \hat{z} = cos(\phi)\ sin(\lambda). \tag{3.35}$$

For a sphere, $\phi = \phi'$.

The gravitational field of the planet is expressed in terms of radial (g_r) and latitudinal (g_ϕ) components (see, *e.g.*, Lindal *et al.*, 1985)

$$\hat{g} = \hat{u_r} g_r + \hat{g_\phi} g_\phi, \tag{3.36}$$

where $\hat{u_r}$ and $\hat{u_\phi}$ are unit vectors in the radial and latitudinal directions, respectively. The vector components are

$$g_r(r, \phi) = -\frac{GM}{r^2} + \frac{GM}{r^2}\sum_{i=1}^{\infty}(2i+1)J_{2i}\left(\frac{R}{r}\right)^{2i} P_{2i}(sin\phi) + \frac{2}{3}\omega^2 r[1 - P_2(sin\phi)] \tag{3.37}$$

and

$$g_\phi(r, \phi) = -\frac{GM}{r^2}\sum_{i=1}^{\infty} J_{2i}\left(\frac{R}{r}\right)^{2i} \frac{dP_{2i}(sin\phi)}{d\phi} - \frac{1}{3}\omega^2 r \frac{dP_2(sin\phi)}{d\phi}, \tag{3.38}$$

where G is the universal gravitational constant, M is the mass of the planet, J_{2i} is the $2i_{th}$ zonal harmonic coefficient, R is the radius normalized to the J_{2i}, P_{2i} is

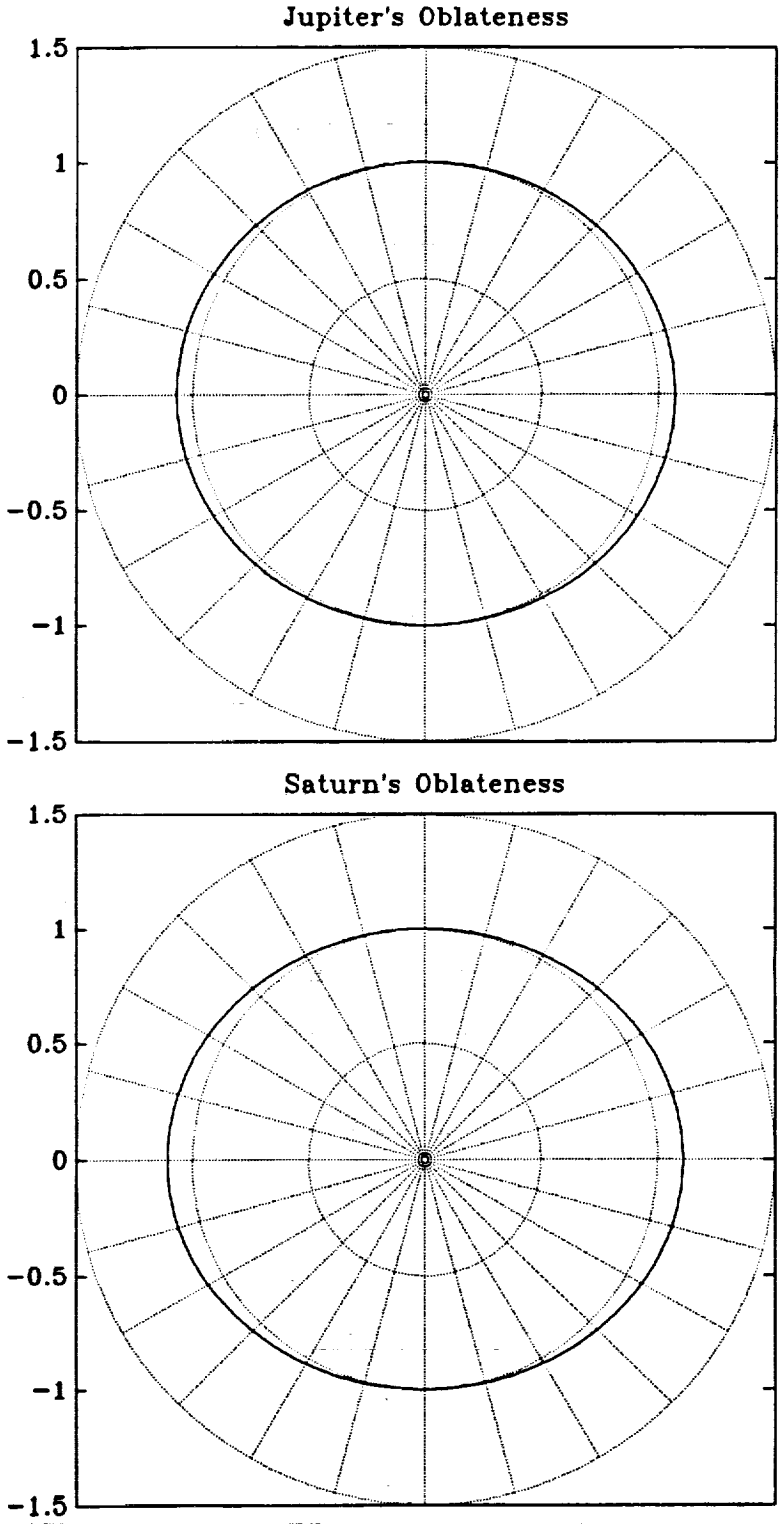

Figure 3.4: The 1 bar surfaces of Jupiter and Saturn.

the Legendre polynomial of degree $2i$, ω is the angular velocity, r is the distance to the center of mass, and ϕ is the planetocentric latitude. The planetocentric and planetographic latitudes are related to the gravitational components by

$$\phi = \phi' - arctan(g_\phi / g_r). \tag{3.39}$$

We found that the variation in gravity over the disk of the planet did not significantly affect the computed brightness temperature. Therefore, we use a constant value of g equal to the area weighted average.

The calculation of the disk-averaged brightness temperature is computationally intensive. However, the amount of computation can be significantly reduced as follows: First, construct a table of the brightness temperature (T_B) as a function of μ, from $\mu = 0.1$ to 1 ($T_B = 0$ at $\mu = 0$) using Equation 3.14. Then compute the value of μ at each point on the (x,y) grid. Use a table look up with linear interpolation to find the brightness temperature at each point on the grid. Use a weighted sum to find the disk-averaged brightness temperature (Equation 3.25). Since the brightness as a function of μ is nearly linear, the brightness temperature need only be computed for a few values of μ (we use approximately 10). The symmetry of the x and y axes further decreases the amount of computation since disk-averaged brightness need only be computed for one quadrant of the visible hemisphere of the planet.

In order to test the accuracy of the finite element grid, the total brightness was evaluated on a circular grid and compared with the exact solution using Equation 3.23. The difference between the two methods was approximately 0.6% in the worst case.

Finally, we computed the disk-averaged brightness with the finite element oblate grid and compared it with the spherical approximation. The difference between the two methods for both Jupiter and Saturn was less than 1% for wavelengths between 1 mm and 10 cm. Since other uncertainties in the radiative transfer model are much larger than 1% (*e.g.*, uncertainty in the absorption coefficient),

the use of the spherical approximation is justified.

3.3 Parameters of the Radiative Transfer Model (RTM)

The parameters of the radiative transfer model (RTM) are the temperature-pressure profile, absorption profiles of the absorbing constituents, and the abundance profiles or vertical distributions of the absorbing constituents (abundance as a function of altitude or pressure). We use a forward modeling approach, in which we vary the parameters of the RTM in order to obtain good agreement between the modeled and observed spectra.

Radiative transfer models are complex because they involve multiple parameters. In most cases, a unique solution does not exist. Fortunately, some of the variables may be constrained. The laboratory measurements of NH_3 absorption described in Chapter 2 are very important, because they eliminate one of the variables in the radiative transfer model. Measurements by the *Voyager* spacecraft help to constrain other variables such as the temperature-pressure profile. In the following sections, we discuss the parameters of the RTM in detail.

3.3.1 Temperature-Pressure Profile

The computation of the temperature-pressure profile begins deep in the atmosphere of the planet where a starting temperature and pressure are specified. A step, dP, is taken and the corresponding change in altitude, dz is computed from Equation 3.17. A check is made to see if condensation has occurred. If so, the lapse rate is equal to the saturated adiabatic lapse rate. The saturated adiabatic lapse rate is found by solving the equation of energy conservation for the adiabatic

expansion of one mole of gas as follows:

$$C_p dT + \frac{RT}{P} dP + L_k dX_k = 0, \tag{3.40}$$

(see, *e.g.*, Atreya and Romani, 1985) where T is temperature, P is pressure, R is the universal gas constant, dX_k is the change in mixing ratio of gaseous condensate k, L_k is the latent heat released on condensation for the k_{th} condensate, and C_p is the specific heat. Substituting Equations 3.7-3.8 into Equation 3.38 yields a form of the saturated adiabatic lapse rate:

$$\frac{dT}{dz} = -\frac{\overline{m}g}{\overline{C_p}} \frac{\left[1 + \frac{1}{RT}\left(\sum_k L_k X_k + \frac{2(X_{H_2S} \cdot X_{NH_3}) L_{RX}}{(X_{H_2S} + X_{NH_3})}\right)\right]}{\left[1 + \frac{1}{\overline{C_p} T^2}\left(\sum_k L_k^2 X_k + \frac{(X_{H_2S} \cdot X_{NH_3}) L_{RX}}{(X_{H_2S} + X_{NH_3})} \cdot 10845\right)\right]}, \tag{3.41}$$

where dz is the layer thickness, $\overline{m}$ is the weighted or mean molecular weight of the atmosphere, g is the gravitational acceleration, and L_{RX} is the heat of reaction for the formation of NH_4SH, and $\overline{C_p}$ is the weighted or mean specific heat of the atmosphere. Using the Clausius-Clapeyron equation (Equation 3.6) and Equation 3.1, the latent heat released per mole is expressed by

$$L = -a_1 + a_3 T + a_4 T^2 + 2a_5 T^3, \tag{3.42}$$

where the a_i are the same coefficients as described in Section 3.1.

If no condensation occurred, the lapse rate is equal to the dry adiabatic lapse rate:

$$\frac{dT}{dz} = -\frac{\overline{m}g}{\overline{C_p}}. \tag{3.43}$$

The temperature-pressure profile is computed iteratively and constrained to meet the deepest level probed by the *Voyager* radio occultation experiments.

A constant specific heat is used for all constituents except H_2. The specific heats are shown in Table 3.1 (Grossman, 1990). The specific heat of hydrogen is explicitly dependent on the *ortho-para* ratio (orientation of the hydrogen atoms in the molecule) which is dependent on temperature. We will assume, as have others (see, *e.g.*, de Pater and Massie, 1985 or Briggs and Sacket, 1989), the

Table 3.1: Specific heat of atmospheric constituents

Atmospheric Constituent	C_p/R
He (Helium)	2.503
CH_4 (Methane)	4.296
H_2O (Water vapor)	4.018
NH_3 (Ammonia)	4.459
H_2S (Hydrogen Sulfide)	4.013

frozen equilibrium or *intermediate* case for the specific heat of hydrogen (see, *e.g.*, Wallace, 1980). The effect of the ortho-para ratio of hydrogen may slightly alter the temperature-pressure profile. However, we will consider the temperature-pressure profile to be a constrained variable in the radiative transfer model.

3.3.2 Opacity

In the last section, we constrained one of the variables of the RTM. In this section, we will examine the opacity from various atmospheric sources in detail. By making use of all of the available laboratory measurements, we will constrain this variable to a large extent. However, some uncertainty in the computation of opacity still remains.

NH_3 Absorption

The new formalism of the Ben-Reuven line shape described in Section 2.2.4 provides the best fit to laboratory NH_3 absorption measurements obtained at radio wavelengths. This formalism will be used to compute the absorption from gaseous

NH_3 in the radiative transfer model.

H_2S Absorption

The absorption from H_2S is computed as in Section 2.3.3. We use the line parameters from the GEISA catalog (Chedin *et al.*, 1982) for 80 lines with frequencies up to 600 GHz. The computed absorption from H_2S under Jovian conditions from 1 to 600 GHz is shown in Figure 3.5.

Pressure-Induced Absorption

Another source of opacity in the radiative transfer model is pressure-induced absorption from molecular hydrogen pairs (*i.e.*, H_2-H_2, H_2-He, and H_2-CH_4). Pressure-induced absorption is caused by the transient dipole which is induced by intermolecular forces in pairs of colliding molecules. This effect is a large source of opacity at millimeter wavelengths for Uranus and Neptune where ammonia is depleted.

Goodman (1969) developed a simple expression for calculating the pressure-induced absorption from H_2-H_2 and H_2-He pairs at radio wavelengths:

$$\alpha_{H_2} = \frac{4.0 \times 10^{-11}}{\lambda^2} P_{H_2}\left[P_{H_2}\left(\frac{273}{T}\right)^{2.8} + 1.7\, P_{He}\left(\frac{273}{T}\right)^{2.61}\right] \text{ cm}^{-1}, \qquad (3.44)$$

where P_{H_2} and P_{He} are the partial pressures of hydrogen and helium in atm, and λ is the wavelength in cm. We compare this expression to the extrapolation of an empirical formalism developed from more recent laboratory data taken at infrared wavelengths (Bachet *et al.*, 1983 and Dore *et al.*, 1983). The pressure-induced absorption is computed from the computationally intensive six-parameter empirical model given by Borysow *et al.* (1985). We fit new parameters for the temperature and pressure dependencies in the Goodman (1969) expression to the Borysow *et al.* (1985) model. We added a term to account for H_2-CH_4 absorption. We optimized the parameters for temperatures and pressures corresponding to

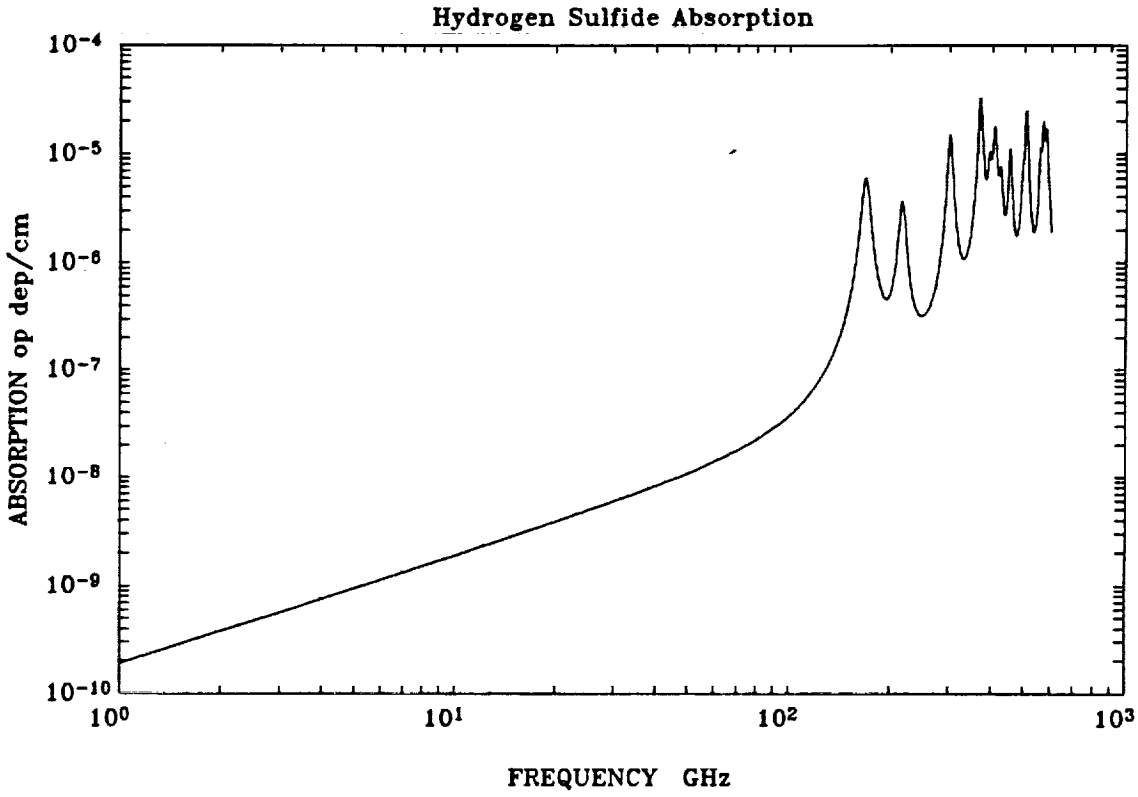

Figure 3.5: The computed absorption from gaseous H_2S under Jovian conditions: $\chi_{H_2} = 0.90$, $\chi_{He} = 0.10$, $\chi_{H_2S} = 3.35 \times 10^{-5}$, P=2 atm, T=200 K.

Jupiter's atmosphere. The new expression is

$$\alpha_{H_2} = \frac{3.557 \times 10^{-11}}{\lambda^2} P_{H_2}\left[P_{H_2}\left(\frac{273}{T}\right)^{3.12} + 1.382 P_{He}\left(\frac{273}{T}\right)^{2.24} + 9.322 P_{CH_4}\left(\frac{273}{T}\right)^{3.34}\right]. \tag{3.45}$$

Graphs of the three formalisms are shown in Figure 3.6 for 30 and 300 GHz (1 cm and 1 mm). Our new expression deviates from the Borysow formalism by less than 1% for pressures less than 10 bar. At higher temperatures which correspond to pressures greater than 100 bar in the Jovian atmosphere, our new expression deviates from the Borysow formalism by approximately 10%.

H_2O Absorption

Goodman (1969) developed an expression for computing water vapor absorption based on the experimental data which was available at that time. This expression employed a Van Vleck-Weisskopf line shape for the rotational line at 22.235 GHz and a residual term for the remaining rotational lines which occur at higher frequencies.

We have developed a new expression for water vapor absorption under Jovian conditions which is based on more recent laboratory data under terrestrial conditions. The parameters for the water vapor lines are summarized by Ulaby *et al.* (1981) from a more detailed compilation by Waters (1976). This calculation includes ten rotational lines with frequencies up to 448 GHz. The kinetic line shape is used in this calculation along with an empirical correction term derived by Gaut and Reifenstein (1971). Our expression is essentially the same as that described in Ulaby *et al.*(1981). The term P representing the pressure in the earth's nitrogen and oxygen atmosphere is replaced by $(0.81P_{H_2}+0.25P_{He})$ to reflect the broadening characteristics of the Jovian atmosphere. Figure 3.7 shows a comparison between the Goodman (1969) expression and our expression for pressures of 1 and 6 bar.

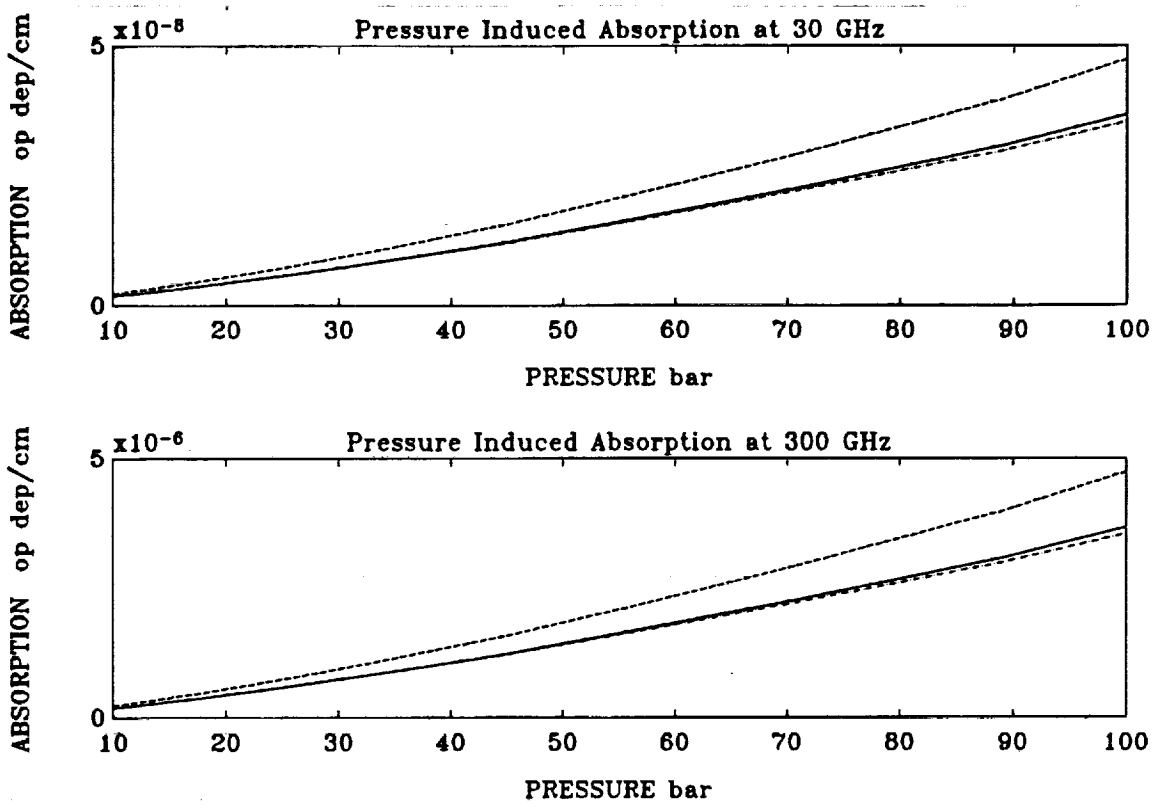

Figure 3.6: Computed pressure-induced absorption from H_2-H_2, H_2-He, and H_2-CH_4 pairs as a function of pressure Jupiter's atmosphere at 30 and 300 GHz; Solid line: our expression; dot-dash line: Borysow *et al.* (1985) model; dashed line: Goodman (1969) expression.

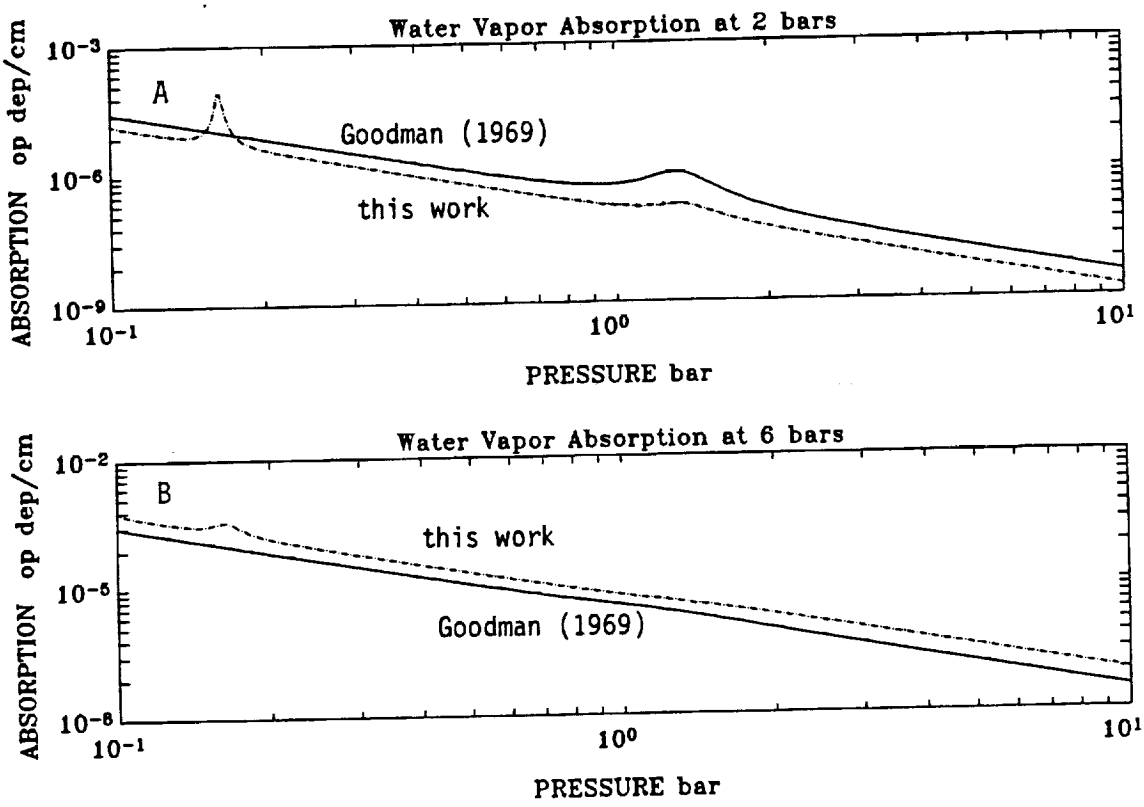

Figure 3.7: Comparison between Goodman's expression and our expression for H_2O absorption with $\chi_{H_2} = 0.9$, $\chi_{He} = 0.1$, and $\chi_{H_2O} = 1 \times 10^{-6}$; A: 1 bar, 150 K; B: 6 bar, 300 K; Solid line: our expression, dot-dash: Goodman (1969) expression.

Absorption from other minor constituents

Lellouch *et al.* (1984a,b) and Lellouch and Destombes (1985) have completed an extensive study of the detectability of minor species in the atmospheres of Jupiter and Saturn at millimeter wavelengths. They considered absorption from phosphine (PH_3), hydrogen cyanide (HCN), carbon monoxide (CO), and many other more complex molecules. The abundances of these molecules in the Jovian atmospheres are quite small. Emission cores arising from molecules such CO or HCN in the stratospheres of Jupiter or Saturn might be detectable. However, their net effect on the millimeter continuum is negligible. In fact, the only molecule capable of providing a significant amount of opacity is PH_3. We will compute PH_3 absorption using the parameters from the Poynter-Pickett catalog (1981) and assuming the same line width as that of H_2S. We will neglect the absorption from other molecules.

Cloud Absorption

Another potential source of opacity at millimeter wavelengths is scattering and absorption from cloud condensates. We have developed a computer program for computing cloud transmissivity and reflectivity using the two-stream approximation. Our cloud model is described in detail below. In the following section, we use this model to compute potential cloud reflectivities and transmissivities for Jupiter.

The volume extinction coefficient for cloud condensates is the sum of its volume absorption and scattering coefficients

$$\alpha_{cloud} = \kappa_e = \kappa_a + \kappa_s = \sum_{i=1}^{N_v} Q_a(r_i) + \sum_{i=1}^{N_v} Q_s(r_i), \qquad (3.46)$$

where Q_s and Q_a are the scattering and absorption cross sections, respectively, N_v is the number of particles per unit volume, and r_i is the radius of the i_{th} particle.

In the Rayleigh approximation, the scattering and absorption cross sections

are simply

$$Q_s = \frac{2\lambda^2}{3\pi}\chi^6 \mid K \mid^2 \tag{3.47}$$

and

$$Q_a = \frac{\lambda^2}{\pi}\chi^3 Im(-K), \tag{3.48}$$

respectively, where

$$K = \frac{\hat{n}^2 - 1}{\hat{n}^2 + 2} = \frac{\hat{\epsilon} - 1}{\hat{\epsilon} + 2}, \tag{3.49}$$

$$\chi = \frac{2\pi r}{\lambda}, \tag{3.50}$$

$$\hat{\epsilon} = \epsilon' - j\epsilon'', \tag{3.51}$$

$$\hat{n} = n - jk, \tag{3.52}$$

$$\hat{\epsilon} = \hat{n}^2, \tag{3.53}$$

$$\epsilon' = n^2 - k^2, \tag{3.54}$$

$$\epsilon'' = 2nk, \tag{3.55}$$

r is the particle radius, λ is the wavelength in the same units, $\hat{n}$ is the complex index of refraction, and $\hat{\epsilon}$ is complex dielectric constant. The Rayleigh scattering approximation is acceptable for $\mid \hat{n}\chi \mid < 0.5$ (Ulaby *et al.*, 1981). If $\mid \hat{n}\chi \mid > 0.5$, a full Mie (1909) calculation should be performed.

If the absorption cross section is much larger than the scattering cross section, Equation 3.44 reduces to a simple form:

$$\alpha_{cloud} = \kappa_a = \frac{18\pi M}{\rho\lambda} \cdot \left[\frac{\epsilon''}{(\epsilon' + 2)^2 + \epsilon''^2}\right] \quad \text{cm}^{-1}, \tag{3.56}$$

(Battan, 1973) where ρ is the density of the condensation particle (in g/cm^3), M is the bulk density of the cloud in the same units, λ is the wavelength in cm.

If the scattering cross section is comparable to the absorption cross section, a more complex model is needed. In this case, the volume absorption and scattering coefficients are

$$\kappa_a = \int_{r_1}^{r_2} p(r) Q_a(r) dr \tag{3.57}$$

and

$$\kappa_s = \int_{r_1}^{r_2} p(r) Q_s(r) dr, \tag{3.58}$$

respectively, where r is the radius of the cloud particle, $p(r)$ is the drop-size distribution, and r_1 and r_2 are the lower and upper limits of the drop radii in the cloud. The phase function asymmetry, g, is

$$g = \frac{1}{\kappa_s} \int_{r_1}^{r_2} G\ p(r)\ Q_s(r) dr, \tag{3.59}$$

where G is the fraction of power scattered in the forward direction. We assume that the scattering is from spherical particles, so that G is determined from the Mie coefficients (see *e.g.*, Gasiewski, 1990).

The uncertainties in modeling the cloud absorption are very large and arise from several sources. One uncertainty is the cloud bulk density. We estimate the densities with the thermochemical model described in Section 3.1. Romani (*private communication*, 1990) suggests that the actual cloud densities on the planets may be a factor of 5 less than those predicted with equilibrium condensation models based on studies of the earth's clouds. Therefore, the cloud bulk density will be a variable in the computation of cloud opacity. Another uncertainty in calculating cloud opacity is the complex index of refraction of NH_3 and NH_4SH ice. The complex index of refraction for NH_3 ice has been measured at infrared wavelengths by Sill *et al.* (1980). We use a value of 1.3 for n_{NH_3} (Sill *et al.*, 1980), 1.74 for n_{NH_4SH} (CRC, 1980), and 1.78 for n_{H_2O} ice (Ulaby, 1981). The value of n should not differ significantly from infrared to millimeter wavelengths. However, the value of k is frequency dependent. We will assume k_{NH_3} and k_{NH_4SH} to be variables. For H_2O ice,

$$k_{H_2O} = \frac{\alpha\lambda}{4\pi}, \tag{3.60}$$

(Grossman, 1990) where α is the absorption coefficient. At $\lambda = 1$ mm, $k_{H_2O} = 0.00035$.

Finally, there is a large uncertainty in the cloud particle size and distribution. West *et al.* (1986) have given a summary of constraints on the particle sizes of

Jupiter's clouds based on a compilation of available observations. There is evidence for a stable layer of particles having effective radii of 1 μm or smaller at pressures from 0.2 to 0.7 bar. A layer of larger particles ($\simeq 3 - 100$ μm) may exist near 0.7 bar primarily in Jupiter's zones. This cloud is thought to be a mixture of NH_3 ice and chromophores (although there is no direct evidence). Bjoraker *et al.* (1986a,b) used a massive absorbing cloud (greybody with $\tau \simeq 3$) at 2 bar in order to explain observations at 5 μm. This second cloud is thought to be NH_4SH ice and/or H_2O ice. There are no estimates of particle sizes for this cloud.

We have assumed the particle-size distribution to be a modified gamma distribution (Deirmendjian, 1969):

$$p(r) = ar^{\alpha} \exp(-br^{\gamma}), \tag{3.61}$$

where a, b, α, and γ are shape factors. We assume two of the shape factors to be similar to those of a cirrostratus cloud:

$$\alpha = 6, \ \beta = 0.5, \tag{3.62}$$

(see, *e.g.*, Ulaby *et al.*, 1981). The remaining shape factors b and γ are determined by specifying a mode radius (r_c) and bulk density M for the cloud. The mode radius, r_c, is defined as the radius at which the distribution $p(r)$ is at a maximum. The shape factors may be written in terms of the mode radius,

$$r_c^{\gamma} = \frac{\alpha}{b\gamma}, \tag{3.63}$$

and the bulk density, M,

$$M = \frac{\rho \, a \, \pi}{3 \, \gamma \, b^{\beta}} \Gamma(\beta) \ \ \mathrm{g/cm^3}, \tag{3.64}$$

where

$$\beta = \frac{\alpha + 4}{\gamma}, \tag{3.65}$$

ρ is the density of the condensate, and Γ is the gamma function.

The radiative transfer problem is simplified by assuming that radiation is scattered in only the forward and backward directions. The cloud is assumed to be made up of discrete homogeneous layers. The reflection and transmission for a layer of thickness dz are

$$r_c = \frac{\overline{\omega}}{1 + \sqrt{1 - \overline{\omega}^2}\coth(\alpha_c\, dz)} \tag{3.66}$$

and

$$t_c = \frac{\sqrt{1 - \overline{\omega}^2}\,\mathrm{csch}(\alpha_c\, dz)}{1 + \sqrt{1 - \overline{\omega}^2}\coth(\alpha_c\, dz)}, \tag{3.67}$$

respectively (Gasiewski, 1990), where α_c is the mode power attenuation coefficient

$$\alpha_c = \sqrt{\kappa_a^2 + 2\kappa_a\kappa_{sb}}, \tag{3.68}$$

$\overline{\omega}$ is the back-scattering albedo

$$\overline{\omega} = \frac{\kappa_{sb}}{\kappa_a + \kappa_{sb}}, \tag{3.69}$$

κ_a includes both gaseous absorption and absorption from cloud particles, and κ_{sb} is the back-scattering coefficient

$$\kappa_{sb} = \kappa_s \frac{1 - g}{2}. \tag{3.70}$$

If the reflectivity and transmissivity of two adjacent layers (a and b) are specified, the combined reflectivity and transmissivity of both layers are

$$r_{ab} = r_a + \frac{t_a r_b t_a}{1 - r_a r_b} \tag{3.71}$$

and

$$t_{ab} = \frac{t_a t_b}{1 - r_a r_b}, \tag{3.72}$$

(*e.g.*, Paltridge and Platt, 1976) respectively, for downwelling radiation. A similar set of equations applies to upwelling radiation.

Once the reflectivity and transmissivity are known, the brightness temperature at $\mu = 1$ can be roughly estimated using the following approach: Suppose

that there is a cloud at pressure P_c and temperature T_c, with reflectivity re_c and transmissivity tr_c, and that the zenith optical depth above the cloud is τ_1. The total brightness or emission at $\mu = 1$ is the sum of the emission from the atmosphere above the cloud, emission from the cloud itself, emission reflected by the cloud, and emission from below the cloud:

$$B_\nu(T, \mu = 1) = \int_0^{\tau_1} B_\nu\big(T(\tau)\big) \exp(-\tau) d\tau + (1 - re_c - tr_c) B_\nu(T_c) \exp(-\tau_1) +$$

$$re_c \exp(-\tau_1) \int_{\tau_1}^{0} B_\nu\big(T(\tau)\big) \exp(-\tau) d\tau + tr_c(1 - re_c) \exp(-\tau_1) \int_{\tau_1}^{\infty} B_\nu\big(T(\tau)\big) \exp(-\tau) d\tau \quad (3.73)$$

3.3.3 Vertical Distributions of Opacity Sources

In the previous two sections, we constrained two of the three parameters of the RTM to a large degree. This leaves the vertical distribution of opacity sources as the main variable in the model. The gaseous constituents are well mixed in the deep atmospheres of the giant planets. Some of the gaseous constituents will be destroyed by photolysis or condensation at higher altitudes. We estimate the vertical distribution of the cloud forming constituents NH_3, H_2S, and H_2O using the thermochemical model described in Section 3.1. The actual distributions are more complex; they exhibit latitudinal variations due to upwelling and downwelling, and some of the gaseous constituents might be super-saturated (see, *e.g.*, de Pater *et al.*, 1989). We will use a single distribution to model the disk-averaged brightness temperatures of the giant planets. Our goal is to find distributions of opacity sources which provide good fits to the observed spectra of giant planets.

3.4 Modeling Results

In the previous sections, we developed an elaborate model for computing the brightness temperatures of the giant planets. We now adjust the parameters of the

model in order to obtain a good fit between the modeled and observed brightness temperatures. A list of reliable observations has been compiled for each of the planets. We examine the millimeter observations and their calibration procedures in detail. The most detailed analysis is carried out for Jupiter. Of the four giant planets, Jupiter has perhaps the most interesting millimeter-wave spectrum because the emission originates from pressures near the putative NH_4SH cloud.

The temperature-pressure profile, T(P) for each of the Jovian planets is shown in Figure 3.8. The temperature-pressure profiles of the four planets are similar in that each planet has a well defined troposphere in which the temperature increases with increasing pressure. The temperatures of the planets generally decrease as the distance from the sun increases. The temperature-pressure profiles for Uranus and Neptune are almost identical even though Neptune is much further from the sun than Uranus. Neptune, like Jupiter and Saturn, possesses a large internal heat source. Uranus has a much smaller internal heat source. Some of the model parameters are listed in Table 3.2. The deepest temperature and pressure probed by the *Voyager* spacecraft are listed in the table.

The modeling work presented here extends the work of others who have developed similar models to carry out detailed analyses of the centimeter wavelength emission from the giant planets (see references in following sections). The goal here is to focus on the millimeter region of the radio spectrum and to draw comparisons between the millimeter-wave spectra of the four giant planets.

3.4.1 The radio spectrum of Jupiter

Jupiter's radio emission is composed of both thermal (quasi-thermal) and non-thermal components. The thermal component is emission from the planet which exhibits the characteristics of a blackbody radiating at its physical temperature. The non-thermal component is cyclotron and synchrotron radiation from energetic electrons moving within the magnetosphere of a planet. The non-thermal com-

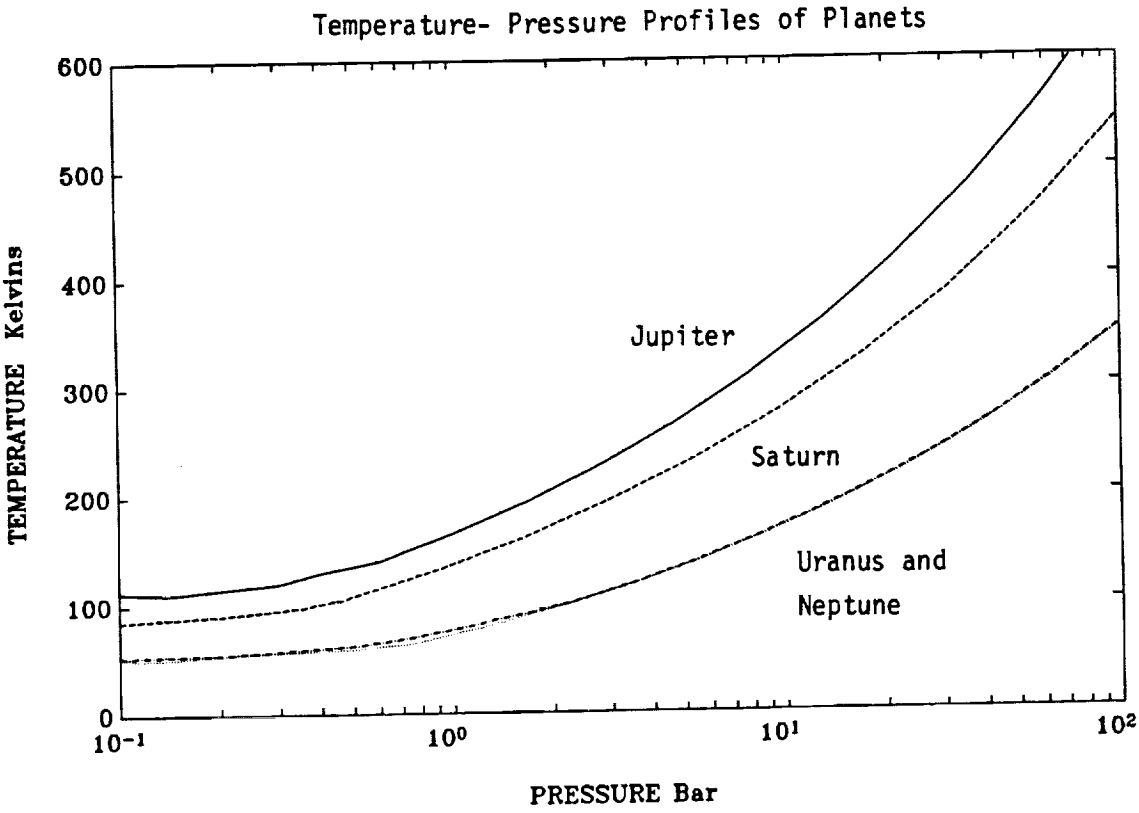

Figure 3.8: Temperature-pressure profiles of the Jovian planets; Solid line: Jupiter, dashed line: Saturn, dot-dashed: Uranus, and dotted line: Neptune (indistinguishable from Uranus).

Table 3.2: Model parameters

	Jupiter	Saturn	Uranus	Neptune
χ_{H_2}	0.90	0.963	0.833	0.833
g (cm/s^2)	2417	982	850	1130
T (K)	165[a]	107.5[b]	100.9[c]	78[d]
P (bar)	1	0.5	2.3	1.2

[a]Lindal *et al.*(1981), [b]Lindal *et al.*(1985),[c]Lindal *et al.*(1987), [d]Tyler *et al.*(1989)

ponent is dominant at wavelengths longer than 7 cm and negligible at millimeter wavelengths. The non-thermal component can be separated from the thermal component so that the observed thermal emission may be compared with synthetic thermal emission spectra.

We have compiled a list of Jupiter's published millimeter observations to be used as a basis for comparison with synthetic spectra. Table 3.3 lists the reliable observations at frequencies between 36 and 300 GHz (1-8.35 mm) along with corresponding calibration sources and spectral bandwidths. Klein and Gulkis (1978) have normalized all of the observations between 14.5 and 36 GHz (8.35-20.7 mm) to a common flux scale. At longer wavelengths, Berge and Gulkis (1976) have given a survey in which the observations have been normalized to a common flux scale whenever possible. They have also removed the non-thermal component of Jupiter's flux.

Vertical distributions of NH_3, H_2S, H_2O, and PH_3 are shown in Figure 3.9. The distributions of NH_3, H_2S, and H_2O are estimated with the thermochemical

Table 3.3: List of reliable millimeter observations of Jupiter

λ (mm)	ν (GHz)	T_B (K)	Cal	$\Delta\nu$ (GHz)	Reference
1.0	300	168±8	Mars	102,229	Werner *et al.*(1978)
1.08	279	169.9±5.1	Mars	75	Griffin *et al.*(1986)
1.32	227	170.9±3.9	Mars	70	Griffin *et al.*(1986)
1.32	227	165±8	planets	39	Ulich *et al.*(1984)
1.4	214	148±16[a]	planets	275	Rather *et al.*(1975)
1.40	214	168±[b]11	Mars	210	Courtin *et al.*(1977)
2.00	150	173.3±1.1	Mars	50	Griffin *et al.*(1986)
2.13	141	167±12[a]	abs	1-2	Ulich (1974, 1981)
2.14	140	178±13[a]	abs	1-2	Cogdell *et al.*(1975)
3.09	97	174±10[a]	abs	0.1-0.2	Ulich *et al.*(1973)
3.33	90	172.5±1.4	Mars	1-2	Griffin *et al.*(1986)
3.48	86	179.4±4.7	abs	0.03-0.5	Ulich *et al.*(1980)
3.53	85	166±6[a]	DR21	1-2	Ulich (1974)

[a]Brightness temperatures as given in Berge and Gulkis (1976)

[b]Recalculated with beam correction factor in Ulich *et al.*(1980)

model described in Section 3.1. The NH_3 vertical distributions assume a deep mixing ratio of 2.5×10^{-4}. This value corresponds to the upper limit derived by Bjoraker *et al.* (1986a) at 5 μm. Distributions of H_2S assume subcloud mixing ratios equal to the solar abundance (distribution 1: $\chi_{H_2S} = 2.9 \times 10^{-5}$, Anders and Grevesse, 1989) and approximately seven times the solar abundance (distribution 2: $\chi_{H_2S} = 2.2 \times 10^{-4}$). Since the H_2S abundance is less than the NH_3 abundance, H_2S is rapidly depleted near 2 bar due to the reaction with NH_3 to form NH_4SH. The upper limit for the deep mixing ratio of H_2S is the deep mixing ratio of NH_3. If the mixing ratio of H_2S were greater than the mixing ratio of ammonia, the ammonia would be rapidly depleted at 2 bar. This would be inconsistent with microwave observations (Lindal *et al.*, 1981 and de Pater and Massie, 1985). The H_2S distributions are compatible with the upper limit derived by Larson *et al.* (1984) at 2.7μm. For subcloud H_2S mixing ratios less than or equal to the solar abundance, NH_3 is not significantly depleted (as in NH_3 distribution 1). However, if the H_2S mixing ratio is increased to 2.2×10^{-5} (as in H_2S distribution 2), NH_3 becomes depleted near 2 bar (as in NH_3 distribution 2). The formation of an NH_3 ice cloud further depletes the ammonia near 0.75 bar. The H_2O distribution assumes a subcloud mixing ratio equal to the solar abundance (1.5×10^{-3}) and is depleted by the formation of an H_2O cloud. The distribution of PH_3 is the same as that used by Lellouch *et al.* (1984c) which is based on the inferred profile of Kunde *et al.* (1982). This distribution assumes a deep PH_3 mixing ratio $\chi_{PH_3} = 6 \times 10^{-7}$. Phosphine is depleted by photolysis above 1 bar.

The distributions and cloud bulk densities shown here may not represent the actual distributions in Jupiter's atmosphere, but are used as a basis to test the effects of the various absorbers on the computed Jovian spectrum. For example, the actual H_2O distribution in Jupiter's atmosphere may be depleted by a factor of 100 (Bjoraker *et al.*, 1986b). The H_2O distributions and bulk densities shown above are used to illustrate the maximum possible effect of H_2O (gas and clouds)

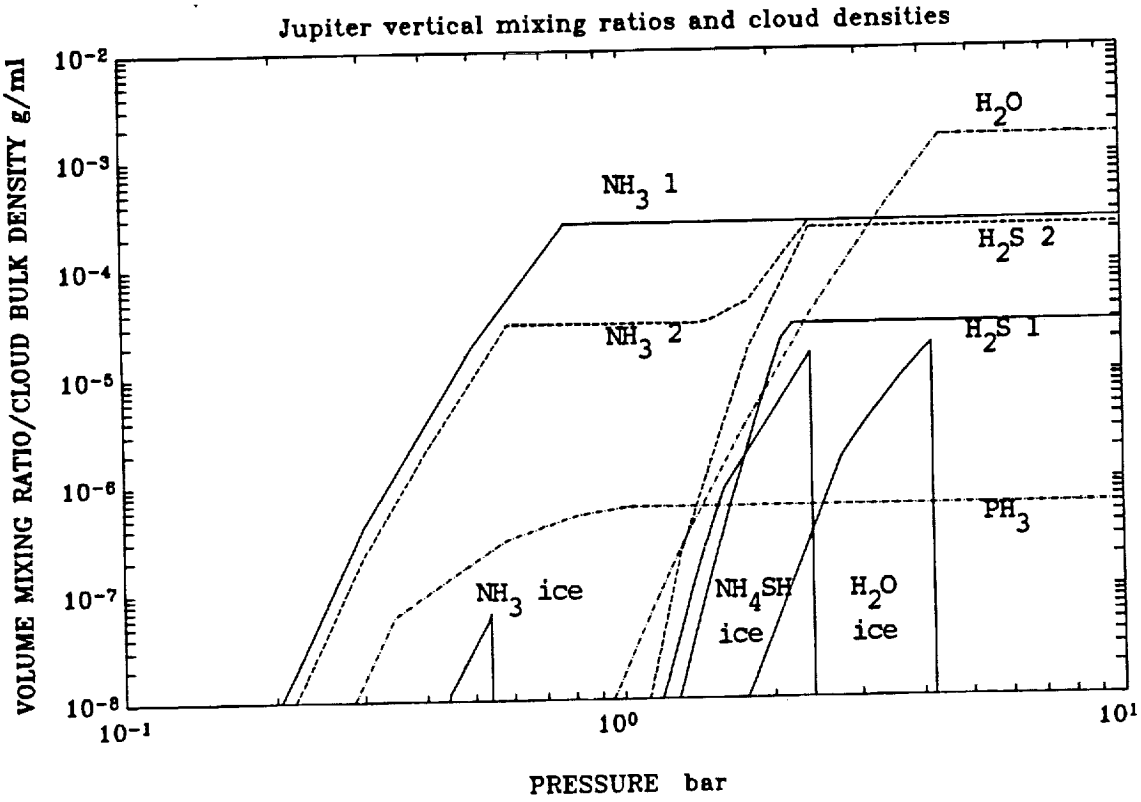

Figure 3.9: Vertical distributions of NH_3, H_2S, PH_3, and H_2O in Jupiter's atmosphere. $\chi_{NH_3} = 2.5 \times 10^{-4}$, $\chi_{H_2O} = 1.5 \times 10^{-3}$ (solar), $\chi_{PH_3} = 6 \times 10^{-7}$; Distribution 1: $\chi_{H_2S} = 2.9 \times 10^{-5}$ (solar), Distribution 2: $\chi_{H_2S} = 2.2 \times 10^{-4}$. Cloud bulk densities from thermochemical model using H_2S distribution 2.

on Jupiter's emission. We do not consider the latitudinal variations in the cm wavelength emission which have been observed with the VLA by de Pater (1986). Instead, we use a single vertical distribution to represent an average over the disk of the planet.

Model sensitivity to NH_3 and H_2O

In Figure 3.10, the Jupiter's observed spectrum is shown along with computed emission spectra. The synthetic emission spectra include only NH_3, H_2O, and pressure-induced opacity and use the two NH_3 distributions shown in Figure 3.9. The error bars for observations using Mars as the primary calibrator include a 10% uncertainty for the calibration in addition to the systematic uncertainties reported in Table 3.2. Synthetic spectra using both NH_3 distributions provide a good fit to observations near 1.3 cm and at longer wavelengths. However, only NH_3 distribution 1 provides a good fit to the millimeter-wave observations. The influence of the 183 GHz H_2O line on the computed emission is small for NH_3 distribution 1.

Model sensitivity to H_2S and PH_3

The effect of adding H_2S opacity to Jupiter's computed spectrum for the two NH_3 distributions is shown in Figure 3.11 (dashed line: NH_3, H_2O, and pressure-induced opacity only, solid line: H_2S opacity added). We have also modeled the effect of the phosphine (PH_3) rotational line at 267 GHz. As seen in Figure 3.12, the effect of PH_3 opacity is limited to frequencies near its transition at 267 GHz.

Model sensitivity to clouds

Previous attempts to model the effects of cloud opacity have only included the potential contribution from the NH_3 ice cloud. For example, Griffin *et al.* (1986) have modeled the potential effect of the NH_3 cloud on Jupiter's millimeter and submil-

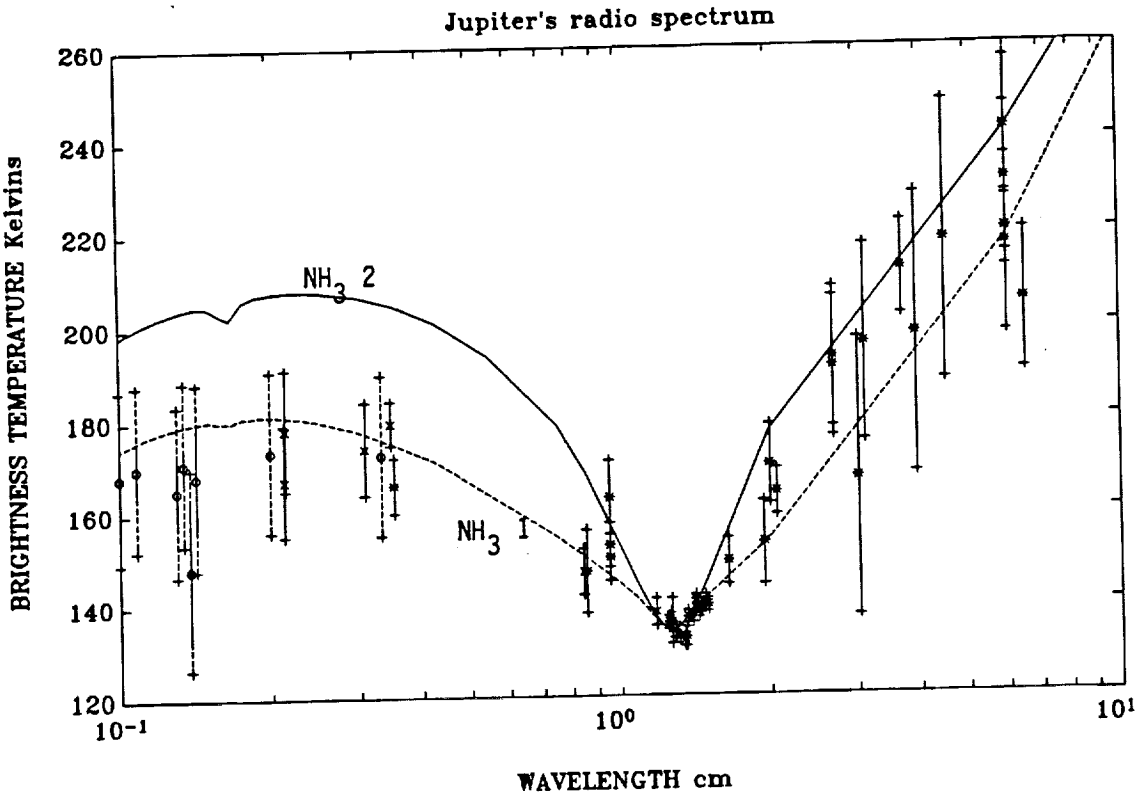

Figure 3.10: Observed spectrum of Jupiter. Error bars include systematic uncertainty (solid line) and 10% uncertainty for observations using Mars as calibrator (dashed line). Computed emission using NH_3, H_2O, and pressure-induced opacity only with vertical distributions in Figure 3.9.

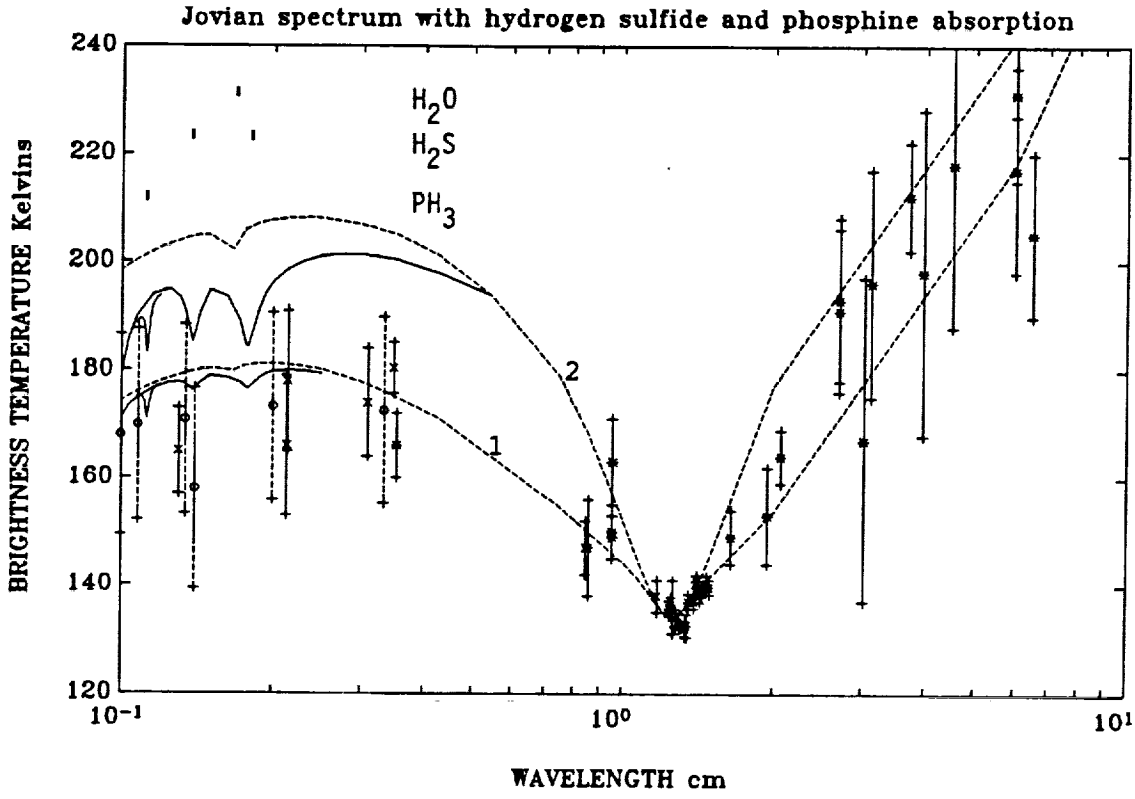

Figure 3.11: Observed spectrum of Jupiter with computed emission using NH_3 and H_2S distributions 1 and 2 from Figure 3.9. Dashed line: NH_3 and H_2O opacity only; Solid line: NH_3, H_2O, PH_3, and H_2S opacity.

limeter emission using a multiple scattering solution for various effective radii and particle-to-gas scale heights. Their model assumed that the imaginary part of the index of refraction (k_{NH_3}) decreased exponentially with frequency from the measured value at 50 cm^{-1} ($\lambda = 200$ μm). The difference in brightness temperature resulting from cloud scattering model at 1 mm was less than 5%. Similarly, Bezard *et al.* (1983) have modeled the multiple scattering effects of the NH_3 cloud by assuming that k_{NH_3} was the same at 1 mm as the measured value at 200 μm. They also found that the contribution from the NH_3 cloud at millimeter wavelengths was negligible.

Figure 3.12 shows normalized weighting functions at 1 mm, 1 cm, and 10 cm using model 2 above with and without cloud opacity. The 1 cm weighting function is very sensitive to gaseous NH_3 since it is near the 1.3 cm inversion wavelength. The 1 cm weighting function peaks near 0.5 bar, close to the NH_3 saturated vapor pressure. At longer wavelengths, NH_3 is more transparent, and the weighting function peaks much deeper in the atmosphere. For example, the 10 cm weighting function peaks near 6 bar. At millimeter wavelengths, the weighting functions begin to increase near 0.8 bar due to NH_3 opacity. The 1.4 mm weighting function has a second peak near 2 bar. This second peak is due to H_2S absorption since 1.4 mm is near a strong H_2S absorption line.

The weighting functions show that most of the emission at short millimeter wavelengths originates from pressures between 1 and 3 bars. Therefore, the potential contributions from the putative NH_4SH cloud should also be included. We have computed a weighting function which includes cloud opacity using Equation 3.56. This weighting function does not include the effects of cloud scattering. The 1 mm weighting function with cloud opacity has several interesting features. The main peak near 0.8 bar is due to gaseous NH_3(also present in the cloud free weighting function). The first small peak near 0.5 bar is due to opacity from the NH_3 ice cloud. The second much larger peak is due to opacity from the NH_4SH

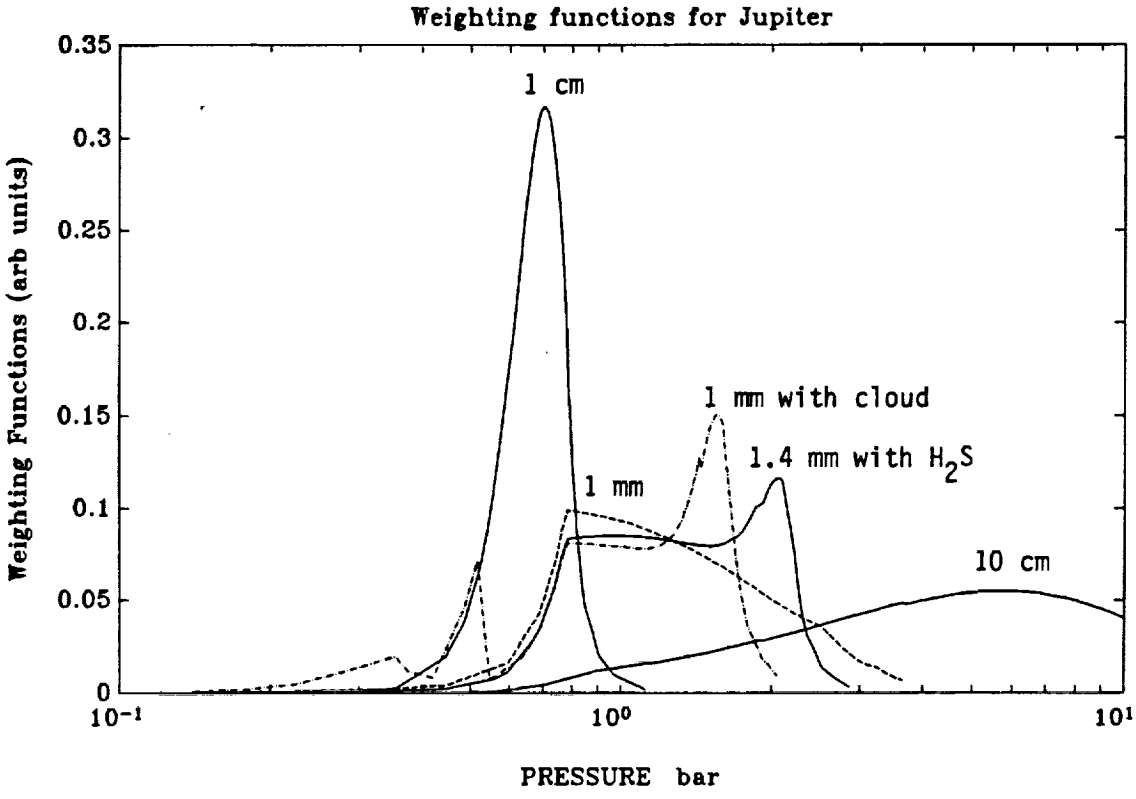

Figure 3.12: Weighting functions for Jupiter at 1 mm (with and without cloud opacity, 1.4 mm (with H_2S opacity), 1 cm, and 10 cm.

cloud near 2 bar.

We have computed the cloud reflectivity (re_c) and transmissivity (tr_c) of the NH_3 and NH_4SH clouds using the approach outlined in Section 3.3.2 for scattering in the forward and backward directions. We compute the reflectivity and transmissivity for several different values of k (the imaginary or absorbing part of the complex index of refraction, $\hat{n} = n - jk$), fractional bulk density M/M_o, where M_o are the bulk densities shown in Figure 3.9, and mode radius (r_c). The bulk densities shown in Figure 3.9 were computed by assuming that the subcloud H_2S abundance was enhanced relative to the solar value. If the H_2S abundance is closer to the solar abundance, the NH_4SH cloud density will be lower and the NH_3 cloud density will be higher. Therefore, we have computed the reflectivities and transmissivities over a range of bulk densities. The computed reflectivities, transmissivities, and corresponding zenith optical depths, $\tau = -\ln(t_c)$, are listed in Table 3.4. The transmissivity includes absorption from the clouds as well as the gases within the cloud. We have also determined the corresponding reduction in Jupiter's brightness temperature resulting from the effects of reflection and absorption by clouds using the two NH_3 distributions shown in Figure 3.9 (ΔT_1 and ΔT_2, respectively). The clouds have a larger effect when less opacity is present above the clouds as in NH_3 distribution 2.

Both the opacity and reflectance of the NH_3 ice cloud are small. We also find that its influence on Jupiter's spectrum is small. However, the opacity and reflectance of the NH_4SH ice cloud is significant in some cases. For $r_c > 40$ μm, the cloud is highly absorbing regardless of the value of k_{NH_4SH}. For $r_c = 10$ μm, the cloud is still highly absorbing for $k_{NH_4SH} > 0.01$. The NH_4SH cloud is also opaque when the cloud bulk density is decreased by a factor of 20.

Figure 3.13 shows synthetic emission spectra with and without a highly absorbing cloud at 2 bar using NH_3 distributions 1 and 2. The absorption is computing according to Equation 3.56 (scattering is not included) with $k = 0.05$ and

Table 3.4: Potential cloud reflectivities (re_c), transmissivities (tr_c), zenith optical depth (τ), and reduction in Jupiter's brightness temperature using NH_3 distributions 1 and 2 from Figure 3.9 (ΔT_1 and ΔT_2) at 1 mm for different values of k, $\hat{n} = n - jk$, mode radius r_c, and fractional bulk density M/M_o where M_o are the bulk densities shown in Figure 3.9

Cloud	k	M/M_o	$r_o(\mu m)$	tr_c	τ	re_c	ΔT_1	ΔT_2
NH_3	0.001	1	40	0.99	0.01	0.0008	1	3
($n = 1.3$)	0.01	1	40	0.98	0.02	0.005	3	5
	0.05	1	40	0.90	0.11	0.008	8	12
	0.001	1	100	0.99	0.01	0.002	1	3
	0.01	1	100	0.97	0.03	0.01	5	7
	0.05	1	100	0.89	0.12	0.02	12	16
	0.001	2	40	0.99	0.01	0.001	1	3
	0.01	2	40	0.95	0.05	0.01	6	9
	0.05	2	40	0.81	0.21	0.02	16	22
	0.001	2	100	0.99	0.01	0.01	4	6
	0.01	2	100	0.93	0.07	0.03	13	17
	0.05	2	100	0.79	0.24	0.04	22	29
NH_4SH	0.001	1	10	0.16	1.8	0.06	5	17
($n = 1.74$)	0.01	1	10	0.01	4.6	0.03	4	14
	0.05	1	10	5×10^{-8}	17	0.01	4	11
	0.001	1	40	2×10^{-4}	8.5	0.36	4	55
	0.01	1	40	4×10^{-8}	17	0.28	11	45
	0.05	1	40	4×10^{-16}	35	0.19	10	33
	0.001	1	100	1×10^{-6}	14	0.60	8	85
	0.01	1	100	1×10^{-13}	30	0.46	17	68
	0.05	1	100	9×10^{-28}	62	0.26	14	43
	0.001	0.05	10	0.30	1.2	0.005	2	8
	0.01	0.05	10	0.26	1.3	0.004	2	8
	0.05	0.05	10	0.14	2.0	0.003	3	9
	0.001	0.05	40	0.15	1.9	0.12	6	26
	0.01	0.05	40	0.13	2.0	0.11	5	25
	0.05	0.05	40	0.05	2.7	0.08	5	20
	0.001	0.05	100	0.07	2.7	0.21	9	34
	0.01	0.05	100	0.05	3.0	0.19	8	35
	0.05	0.05	100	0.01	4.6	0.13	6	26

the bulk densities equal to those shown in Figure 3.9 in order to simulate a highly absorbing NH_4SH cloud. At 1 mm, the brightness temperature using both distributions with a highly absorbing cloud provide good fits to the observations. The clouds also decrease the effect of H_2S shown with a solid line, since most of the H_2S gas should exist just beneath the NH_4SH cloud. Since neither cloud nor NH_3 absorption has distinctive spectral features, cloud opacity cannot be distinguished from the effects of NH_3 opacity. However, NH_3 distribution 1 still provides a better fit to the spectrum at the longer millimeter wavelengths than distribution 2. This suggests that NH_3 is most likely the dominant source of opacity on Jupiter at millimeter wavelengths. This also suggests that NH_3 is probably not significantly depleted by the reaction with H_2S to form solid NH_4SH and consequently $\chi_{H_2S} \ll \chi_{NH_3}$.

3.4.2 The radio spectrum of Saturn

A list of Saturn's radio observations has been compiled by Klein *et al.* (1978). The observations in this survey have been normalized to a common flux scale. Corrections for the size of the oblate planet were also applied to all of the observations. The influence of the rings was removed so that the brightness temperatures correspond to the temperatures which would have been observed in the absence of the rings. Additional observations have been compiled by Grossman (1990).

Detailed analyses of the centimeter spectrum of Saturn have been carried out by Grossman (1990) and Briggs and Sackett (1989). These authors have investigated several possible distributions of NH_3, H_2S, and H_2O in Saturn's atmosphere. Their best fits to centimeter wavelengths observations used enriched NH_3 and H_2S mixing ratios (relative to the sun). As on Jupiter, the overall mixing ratio of H_2S is less than that of NH_3, so that H_2S is depleted in the upper atmosphere. The observed latitudinal variation at centimeter wavelengths is characterized by a hot band at northern latitudes (Grossman, 1990). This is suggestive of a large scale

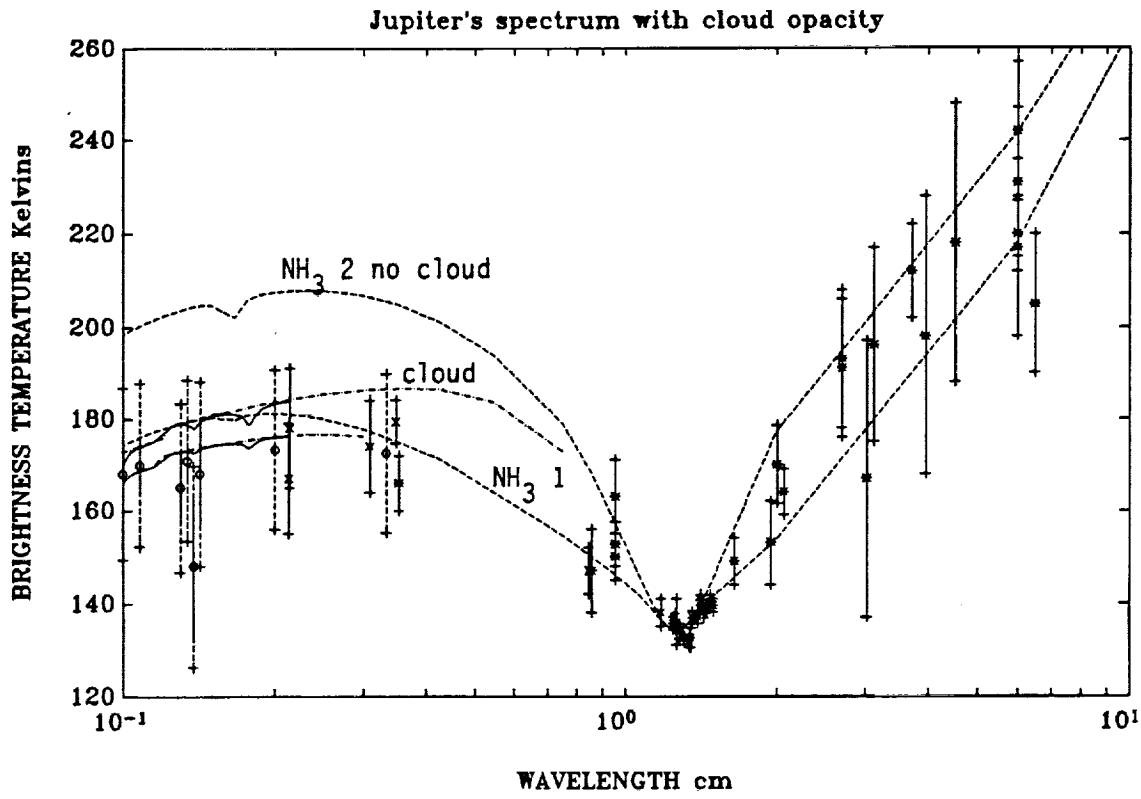

Figure 3.13: Observed spectrum of Jupiter with computed emission using NH_3 distributions 1 and 2 with and without cloud opacity included. Dashed line: NH_3 and H_2O opacity only; dot-dash line: highly absorbing cloud; solid line: H_2S opacity added.

circulation pattern.

Figure 3.14 shows three vertical distributions of NH_3 and cloud bulk densities. Figure 3.15 shows Saturn's observed spectrum with three synthetic spectra using the vertical distributions in Figure 3.14. Figure 3.16 shows normalized weighting functions using NH_3 distribution 3 at 1 mm, 1 cm, and 10 cm. Again, the weighting function at 1 cm is sensitive to the presence of NH_3 gas and peaks near the NH_3 saturation pressure. The weighting function at 1 mm peaks slightly deeper in the atmosphere. The weighting function at 10 cm peaks still deeper. The sharp peak in the 10 cm weighting function near 7 bar is due to the increase in the NH_3 abundance at that pressure (see Figure 3.14) where the NH_4SH cloud forms.

Since the millimeter-wave emission originates from near the same altitudes as the NH_3 cloud, Saturn's cloud opacity should be very small. Moreover, the millimeter-wave emission originates from altitudes where H_2S and H_2O are likely to be severely depleted. Therefore, the only opacity sources are NH_3 and pressure-induced absorption. Since the opacity from NH_3 is significantly larger than that from pressure-induced absorption, the millimeter-wave spectrum of Saturn is primarily sensitive to the vertical distribution of NH_3.

3.4.3 The radio spectrum of Uranus

Gulkis and de Pater (1984) have reviewed the existing millimeter and centimeter observations of Uranus and have normalized the observations to a common radius and flux scale whenever possible. Detailed analyses of the microwave spectrum of Uranus have been carried out by Hofstadter and Muhleman (1988), Hofstadter *et al.* (1990) and de Pater *et al.* (1989, 1991). Both temporal and spatial variations have been observed in the Uranus atmosphere (see, *e.g.*, , Hofstadter and Muhleman, 1988 and Gulkis and de Pater, 1984). The spatial variation is characterized by a large pole-equator gradient in which the brightness temperature is warmer at the pole than at the equator. The observed brightness temperatures of Uranus

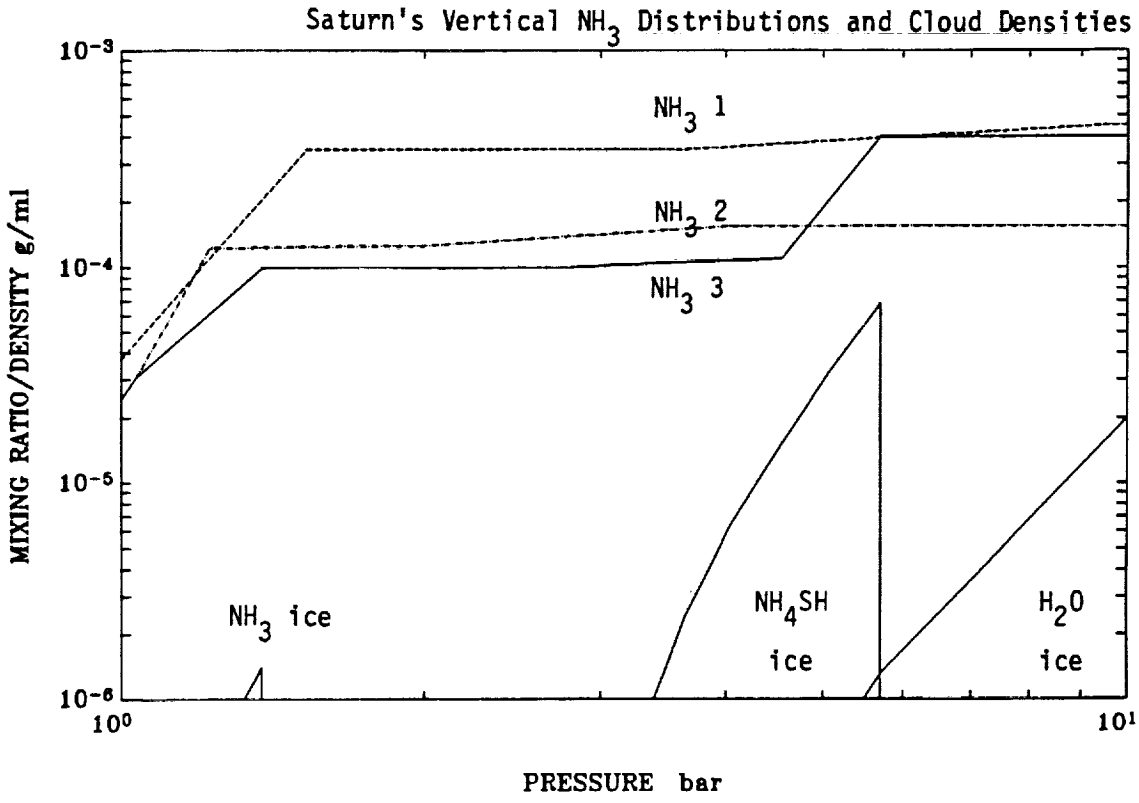

Figure 3.14: Vertical NH_3 distributions and cloud bulk densities in Saturn's atmosphere; 1-Dashed line: $\chi_{NH_3} = 4.5 \times 10^{-4}$, $\chi_{H_2S} = 1 \times 10^{-4}$; 2-Dot-dashed line: $\chi_{NH_3} = 1.5 \times 10^{-4}$, $\chi_{H_2S} = 2.9 \times 10^{-5}$ (solar); 3- Solid line: $\chi_{NH_3} = 4 \times 10^{-4}$, $\chi_{H_2S} = 3.6 \times 10^{-4}$; For cloud bulk densities, $\chi_{NH_3} = 4 \times 10^{-4}$, $\chi_{H_2S} = 3.6 \times 10^{-4}$, and $\chi_{H_2O} = 1.5 \times 10^{-3}$.

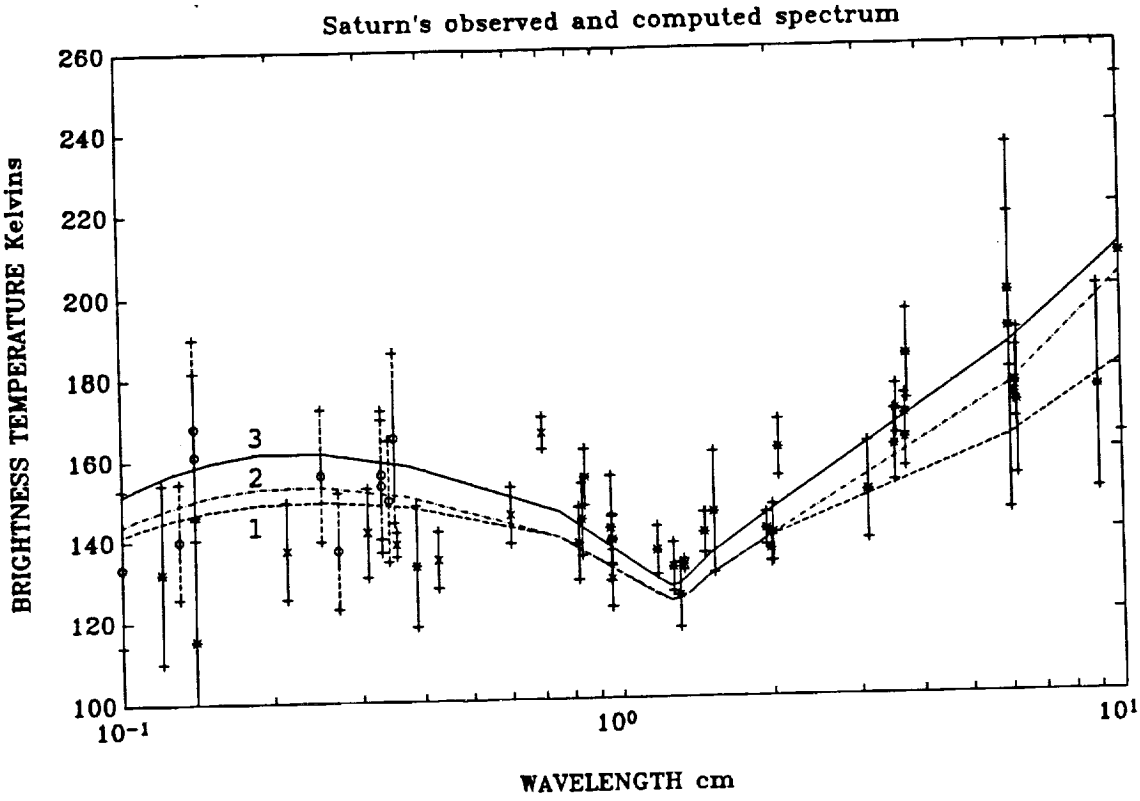

Figure 3.15: Observed spectrum of Saturn with computed emission using vertical NH_3 distributions in Figure 3.14.

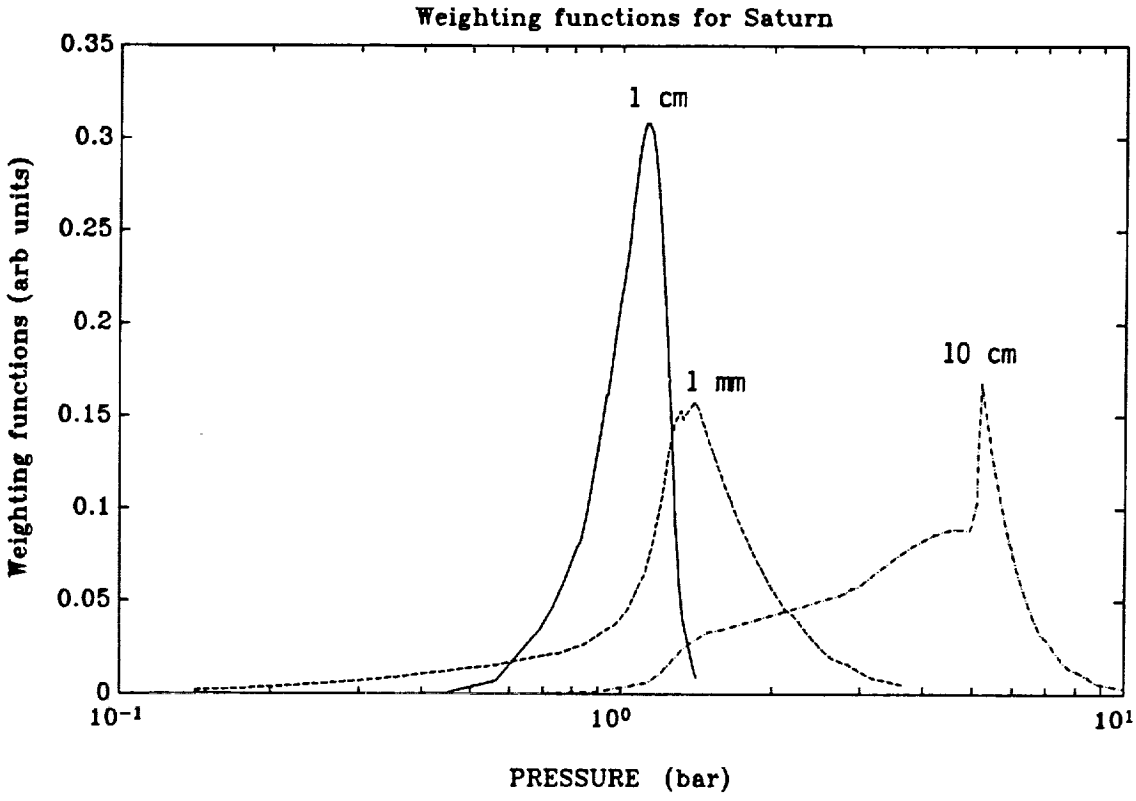

Figure 3.16: Weighting functions at 1 mm, 1 cm, and 10 cm for Saturn using NH_3 distribution 3.

increased between 1965 and 1973. This was the time when the its pole, inclined at an angle of almost 90 degrees, came into view. The temporal variation can be explained to first order by a change in the viewing aspect of the planet (see *e.g.*, de Pater *et al.*, 1989).

The observed radio spectrum of Uranus is shown in Figure 3.17 along with several synthetic spectra. The spectrum at short millimeter wavelengths is dominated by pressure-induced absorption. The vertical distributions and mixing ratios of NH_3, H_2S, and H_2O have virtually no effect on Uranus' millimeter spectrum. Therefore, our computed spectra should in effect be a good test of the assumed temperature-pressure profile. At centimeter wavelengths, we show only a few of the computed spectra which have been previously explored (see, *e.g.*, de Pater *et al.*, 1989, 1991). We show the effect of pressure-broadened H_2S on Uranus' centimeter wavelength emission. The synthetic spectra with $\chi_{H_2S} > \chi_{NH_3}$ provide a better fit to the observed spectrum than those with $\chi_{H_2S} < \chi_{NH_3}$.

Weighting functions at 1 mm, 3 mm, 1 cm, and 10 cm are shown in Figure 3.18. The 1 cm weighting function has a sharp peak due to NH_3 opacity. This peak occurs at higher pressures than on Jupiter and Saturn due to the colder temperatures. The weighting function at 10 cm is similar to that of Saturn. The second peak near 20 bar is due to an increase in NH_3 abundance near the saturation pressure of NH_4SH. In contrast to Jupiter and Saturn, the 1 mm weighting peaks at higher altitudes (lower pressures) than the 1 cm weighting function. This is evidence of the large effect of pressure-induced opacity at millimeter wavelengths.

3.4.4 The radio spectrum of Neptune

de Pater and Richmond (1990) have compiled a list of Neptune's radio observations. The microwave observations in this list were normalized to the common flux scale of Baars *et al.* (1977). The millimeter observations which were cali-

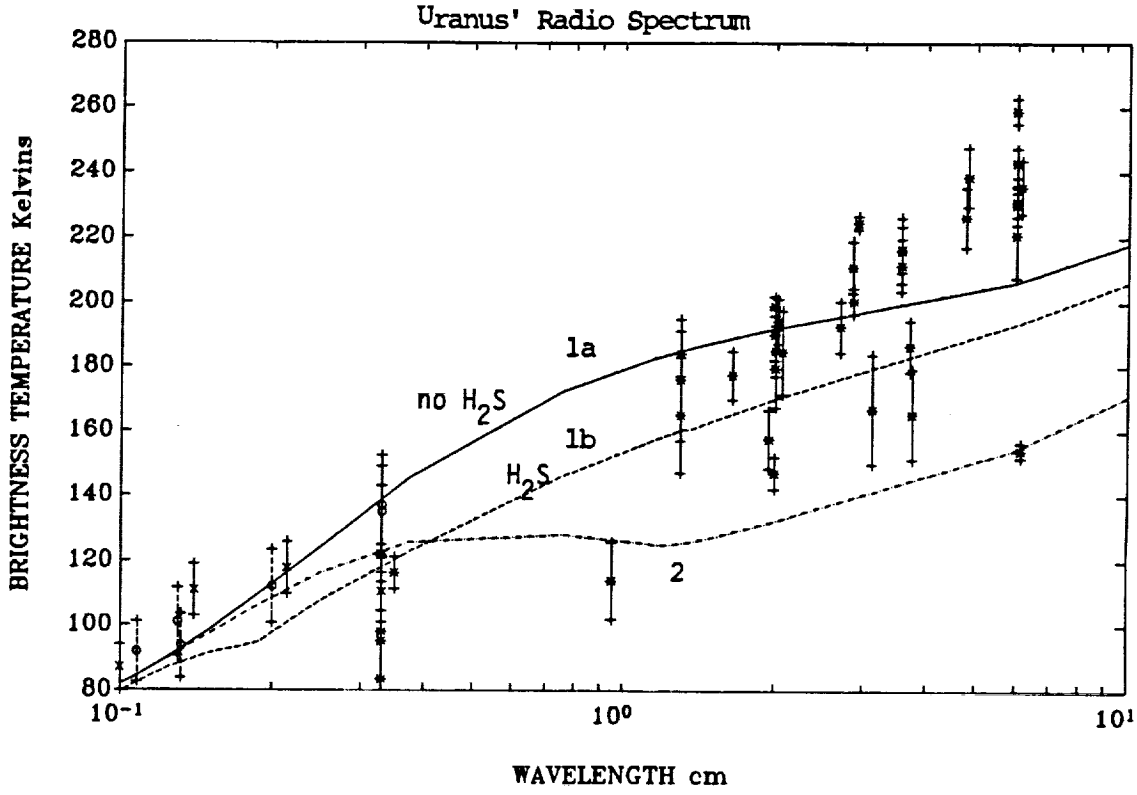

Figure 3.17: Observed spectrum of Uranus with computed emission; 1a, Solid line: $\chi_{NH_3} = 1.5\times10^{-5}$, $\chi_{H_2S} = 1.0\times10^{-4}$ (no H_2S opacity);1b, Dashed line: H_2S opacity added; 2, Dash-dot line: $\chi_{NH_3} = 4.0\times10^{-5}$, $\chi_{H_2S} = 3.3\times10^{-5}$; $\chi_{H_2O} = 1.5\times10^{-3}$ for all spectra.

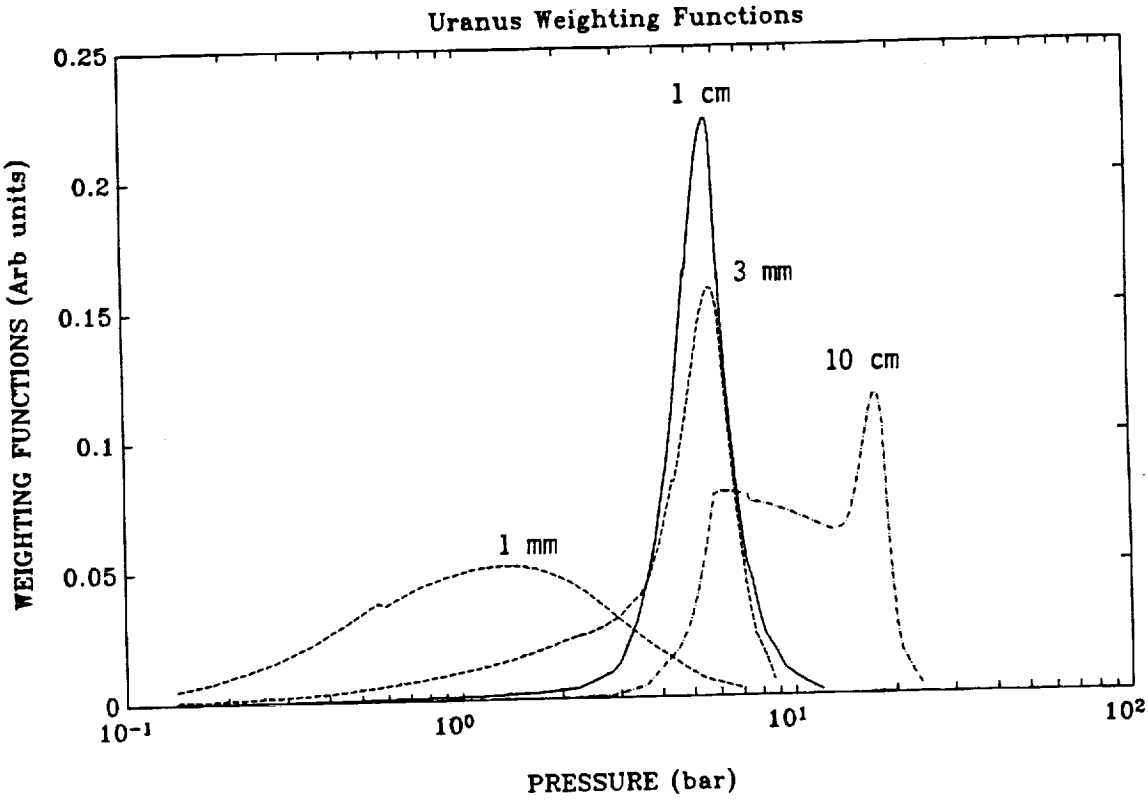

Figure 3.18: Weighting functions for Uranus at 1 mm, 3 mm, 1.3 cm, 10 cm.

brated with Mars or Jupiter were renormalized following the method described in Griffin *et al.* (1986).

Neptune's millimeter spectrum is quite similar to that of Uranus. At short millimeter wavelengths, the opacity is primarily due to pressure-induced absorption. Again, the millimeter spectrum is relatively insensitive to the mixing ratios of the volatile constituents. Romani *et al.* (1989) and de Pater *et al.* (1991) have analyzed Neptune's centimeter spectrum in great detail. At centimeter wavelengths, the spectrum is dominated by NH_3, liquid H_2O, and possibly H_2S opacity. We show Neptune's observed spectrum and a sample of computed spectra which are similar to those previously explored by Romani *et al.* (1989) and de Pater *et al.* (1991) in Figure 3.19.

3.5 Conclusions and Comparisons

The weighting functions at 1 mm peak near 1 bar for all four planets. Table 3.5 lists the magnitude of the absorption coefficients for the four Jovian planets at 1 bar and at 1 mm. At millimeter wavelengths, Jupiter and Saturn exhibit characteristics of NH_3 opacity. The millimeter-wave spectra of Uranus and Neptune are dominated by pressure-induced absorption and not NH_3 opacity. They do not provide any information about NH_3 or H_2S abundances or distributions. All four planets exhibit higher brightness temperatures at the longer centimeter wavelengths which is primarily due to the inversion spectrum of NH_3.

Using our new formalism for the Ben-Reuven line shape in the radiative transfer model, we found that Jupiter's observed millimeter-wave spectra can adequately be explained with NH_3 as the primary opacity source. Good fits to the observed spectrum are achieved using vertical distributions for NH_3 derived from equilibrium condensation models with $\chi_{NH_3} = 2.5 \times 10^{-4}$ (solar abundance enhanced by a factor of 1.3) and $\chi_{H_2S} \leq 2.9 \times 10^{-5}$ (solar abundance).

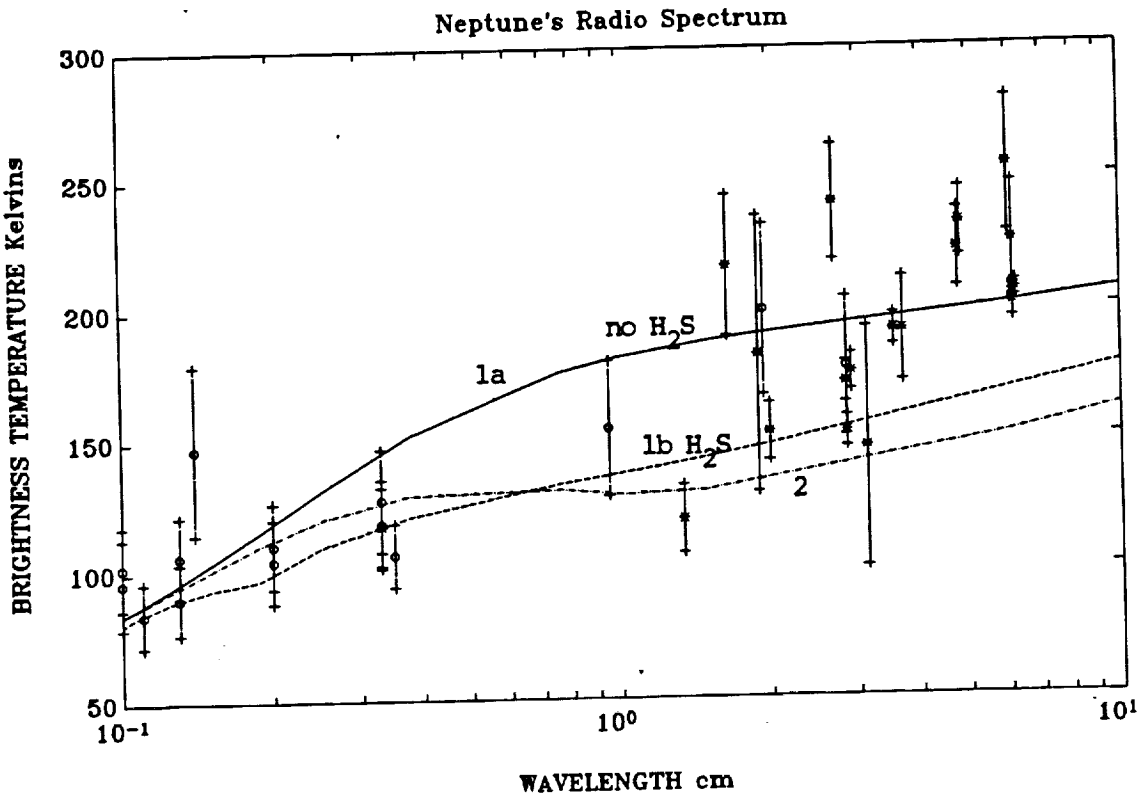

Figure 3.19: Observed spectrum of Neptune with computed emission; 1a, solid line: $\chi_{NH_3} = 1.5 \times 10^{-4}$, $\chi_{H_2S} = 3.3 \times 10^{-4}$ (no H_2S opacity); 1b, Dashed line: H_2S opacity added; 2, Dash-dot line: $\chi_{NH_3} = 4.0 \times 10^{-5}$, $\chi_{H_2S} = 3.3 \times 10^{-5}$; $\chi_{H_2O} = 1.5 \times 10^{-3}$ for all spectra.

Table 3.5: Magnitude of absorption coefficients (in cm^{-1}) at 1 bar, 1 mm

	Jupiter	Saturn	Uranus	Neptune
α_{H_2}	1×10^{-8}	3×10^{-8}	2×10^{-7}	2×10^{-7}
α_{NH_3}	3×10^{-7}	1×10^{-7}	1×10^{-13}	1×10^{-13}
α_{H_2S}	8×10^{-11}	1×10^{-10}	1×10^{-27}	1×10^{-27}
α_{H_2O}	2×10^{-11}	4×10^{-11}	2×10^{-26}	2×10^{-26}
α_{PH_3}	4×10^{-10}	-	-	-

The influence of gaseous H_2O on Jupiter's spectrum is small. Detection of the 183 GHz H_2O line would be extremely difficult with ground-based radio telescopes due to blanking by the terrestrial H_2O line. Cloud condensates may be providing opacity. However, due to large uncertainties in the dielectric properties of the condensates and cloud bulk densities, no firm conclusions regarding cloud opacities can be drawn at this time. Gaseous hydrogen sulfide may be providing additional opacity on Jupiter. Observations with greater spectral resolution are needed in order to detect the potential effect of H_2S opacity on Jupiter's millimeter spectrum and thus distinguish between the effects of H_2S and NH_3 opacity. We discuss the approach and results of such an observation in the following chapter.

CHAPTER 4

Dual Wavelength Observation of Jupiter at 1.4 mm

Sulfur is the tenth most abundant element in the solar system (Anders and Grevesse, 1989). Although sulfur has been detected on Jupiter's volcanic moon Io, it remains mysteriously absent from the list of elements detected in the atmospheres of the Jovian planets. Ground-based observation with radio telescopes provides one of the few means capable of probing beneath the dense cloud layers of the Jovian planets where sulfur in the form of gaseous hydrogen sulfide (H_2S) may be found. Jupiter presents the best target for the H_2S search due to its cloud structure and extreme brightness at millimeter wavelengths. Determination of the sulfur abundance in the giant planet atmospheres would provide valuable information needed to develop and refine models of the origin and evolution of the planets and solar system. The search for sulfur is also of interest relative to the long-standing problem of the unknown composition of colored cloud materials in Jupiter. Because ammonium polysulfides and other sulfur compounds are leading candidates for this material (West *et al.*, 1986), detection of any sulfur containing molecule would be of great value.

Both theory and observation suggest that nearly all of the sulfur is locked up in the clouds of Jupiter's troposphere. Thermochemical models predict that H_2S will combine with NH_3 to form an ammonium hydrosulfide (NH_4SH) ice cloud near the 2 bar pressure level on Jupiter (see Section 3.4.1). If the abundance of H_2S is

less than the abundance of NH_3 at subcloud altitudes in Jupiter's atmosphere, the reaction to produce NH_4SH should rapidly deplete H_2S. Any H_2S which escaped destruction in the reaction to form NH_4SH should be destroyed by photolysis near 1 bar (Bezard *et al.*, 1983). Infrared observations of Jupiter at 2.7 μm by Larson *et al.* (1984) provide a strict upper limit on the abundance of H_2S at pressures between 0.7 and 1.2 bar. This limit reinforces the hypothesis that nearly all of the H_2S is depleted by the formation of an NH_4SH cloud. This leaves millimeter-wave observations as one of the only means of probing deep enough in the atmosphere to detect H_2S.

Bezard *et al.* (1983) suggested that the rotational lines of gaseous hydrogen sulfide (H_2S) in Jupiter's troposphere might provide excess opacity in Jupiter's millimeter spectrum. Millimeter-wave observations probe altitudes in the Jovian atmosphere at and below the altitude of the putative NH_4SH cloud base, where gaseous H_2S may exist. As shown in Figure 3.11, three strong rotational lines of H_2S could potentially affect the emission from Jupiter at millimeter wavelengths. The center frequencies of these lines are 168.8, 216.7 and 300.5 GHz (1.78, 1.38, and 1.00 mm). The hydrogen sulfide (H_2S) transition at 216.7 GHz provides the best opportunity to search for H_2S because it appears in relatively transparent regions of the atmospheres of Jupiter and the earth. In Jupiter's atmosphere, opacity from NH_3 obscures the effects of potential H_2S lines at wavelengths shorter than 1 mm. Interference from the 183 GHz water vapor line in the earth's atmosphere would complicate an observation of the 168.8 GHz H_2S transition.

Detecting the 1.4 mm (216.7 GHz) H_2S line with existing instrumentation is difficult. This line is pressure-broadened by hydrogen (H_2) and helium (He), spreading its total width over 30-40 GHz. Most of the existing observations of Jupiter at millimeter wavelengths have been made with broadband filters which have pass bands of approximately 70 GHz. The filters effectively average the emission detected in the pass band, smearing any smaller scale spectral features

such as pressure-broadened H_2S lines. Other receivers used in millimeter and submillimeter astronomy are designed in order to detect narrow emission lines ($\Delta\nu/\nu \sim 10^{-4}$) in the interstellar medium. These receivers typically have pass bands of less than 1 GHz which would be too narrow to detect pressure-broadened H_2S lines.

We have developed an approach in which a high resolution receiver can be used in order to search for broad spectral features, such as the pressure-broadened H_2S lines on Jupiter. This technique involves observing the differential emission between two or more wavelengths in order to detect H_2S or place limits on its abundance. We have used this approach to observe Jupiter with the 10.4 m Caltech Submillimeter Observatory (CSO)[1] at Mauna Kea, Hawaii. In addition, we have used Mars as a calibration source in order to derive a reliable brightness temperature for Jupiter at 1.4 mm.

4.1 Sensitivity Calculation

Before any observations were undertaken, we had to confirm that the receiver would be sensitive to the change in Jupiter's emission due to H_2S absorption. It is useful to first define several quantities used in this type of calculation. The Rayleigh-Jeans approximation is commonly used at radio frequencies in order to simplify Planck's law (Equation 3.10):

$$B = 2\nu^2 kT/c^2 = 2kT/\lambda^2. \tag{4.1}$$

The Rayleigh-Jeans approximation is valid for $h\nu \ll kT$. The approximation produces errors of approximately 10% at millimeter wavelengths. Using the Rayleigh-Jeans approximation, the total spectral power density, S, radiated from a spherical

[1]The CSO is operated by the California Institute of Technology under funding from the National Science Foundation, Contract #AST-88-15132.

blackbody of radius r at a distance d from the source is

$$S = 2\pi kT(r/d)^2/\lambda^2, \tag{4.2}$$

(Gulkis, 1987), where S is called the flux density. The flux density is in units of power per unit surface area per unit frequency. A commonly used unit for flux density is the Janksy (Jy) which is defined as 10^{26} W m^{-2} Hz^{-1}. The change in antenna temperature, ΔT, (in Kelvins) due to a certain flux density, S, is

$$\Delta T = \frac{S}{2\,k} A_{\rm eff}, \tag{4.3}$$

where $A_{\rm eff}$ is the effective area of the antenna. The effective area is

$$A_{\rm eff} = \sigma\pi\ R^2, \tag{4.4}$$

where σ is the efficiency of the dish, and R is the radius of the antenna.

We first compute the change in antenna temperature (ΔT_{H_2S}) resulting from the expected 2 K difference in Jupiter's brightness temperature due to H_2S absorption using Equations 4.2-4.4. For Jupiter, $r \simeq 71.6 \times 10^3$ km and $d \simeq 4.2$ AU (astronomical units) or 6.28×10^8 km. The diameter of the CSO is 10.4 m and an efficiency of 30% is assumed. We computed the difference in emission assuming a temperature of 180 K at 216 GHz and a temperature of 182 K at 200 GHz. After taking into account the differential flux due to the difference in wavelength, ΔT_{H_2S} is 0.76 K.

We now examine the sensitivity of the receiver in order to determine whether or not it is capable of measuring ΔT_{H_2S}. The sensitivity equation of an ideal balanced Dicke radiometer is

$$\Delta T_{\rm rms} = 2\,\frac{T_S}{\sqrt{t\ d\nu}}, \tag{4.5}$$

where $\Delta T_{\rm rms}$ is called the rms noise power, T_S is the system temperature (a measure of the noise power from the receiver), t is the integration time in seconds, and $d\nu$ is the band width of the receiver in Hz. The full receiver band width of the CSO is

500 MHz. The receiver operates between 200 and 260 GHz. Although the CSO is equipped to make observations with much greater resolution, the full band width of the receiver will be utilized in order to achieve the necessary sensitivity.

The noise temperature of the CSO (for double side band) is reported to be 100 K at 200 GHz and the system sensitivity approximately 500 mJy for a one second integration time. Evaluating Equation 4.5 gives a $\Delta T_{\rm rms} < 0.1$ K. Since $\Delta T_{\rm rms} < \Delta T_{\rm H_2S}$, we are not limited by the sensitivity of the CSO receiver.

4.2 Instrumentation and Procedure

Figure 4.2 shows a block diagram of the CSO facility. The CSO has two available receivers. The 345 GHz receiver is located at the Cassegrain mount. The 230 GHz receiver is located at the sidecab mount in a separate room. A mirror is used to optically transmit the signal from the antenna to the 230 GHz (sidecab) receiver. Our observations were made with the 230 GHz receiver. The receiver is a superconducting insulator superconducting (SIS) quasiparticle tunnel junction mixer. It is contained in a liquid helium dewar at a temperature of about 4 K. A low noise amplifier is maintained at a temperature of about 12 K. The receiver operates in a double side band mode with a band separation of 2.8 GHz (IF band 1150-1650 MHz). A detailed drawing of the 230 GHz receiver is shown in Figure 4.3. The receiver's LO (local oscillator) is generated by doubling a signal from a Gunn oscillator. The oscillator is phase locked to a microwave frequency counter. The LO signal is optically coupled to the receiver through a horn antennas and focusing lenses. The CSO is equipped with two available Acousto-Optic Spectrometers (AOS). Each AOS has 1024 channels with total bandwidths of 500 or 50 MHz. The backend computer automatically controls attenuator settings in order to prevent saturation of the AOS.

The receiver requires careful tuning at each frequency. Tuning the receiver

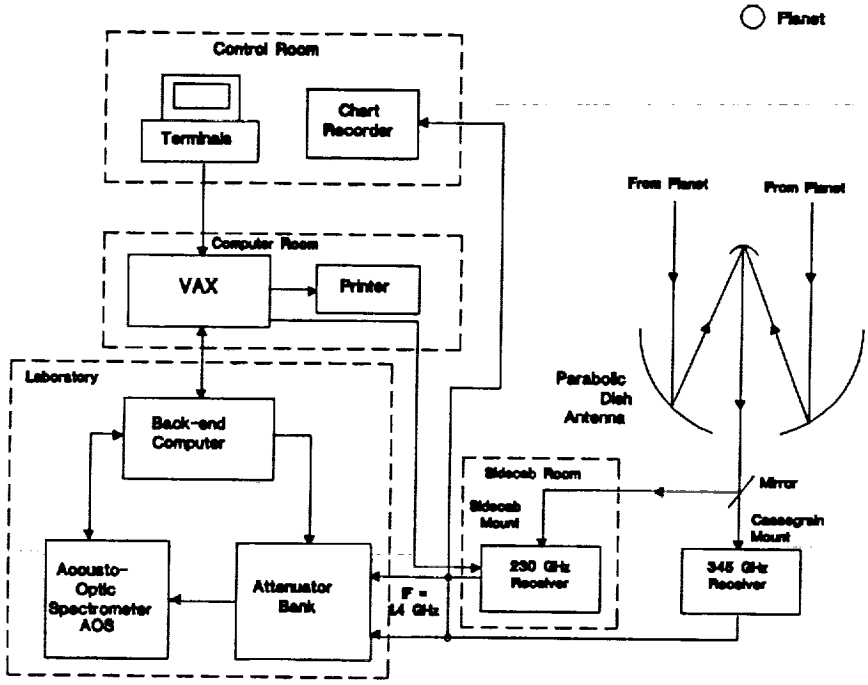

Figure 4.1: Block diagram of the Caltech Submillimeter Observatory (CSO).

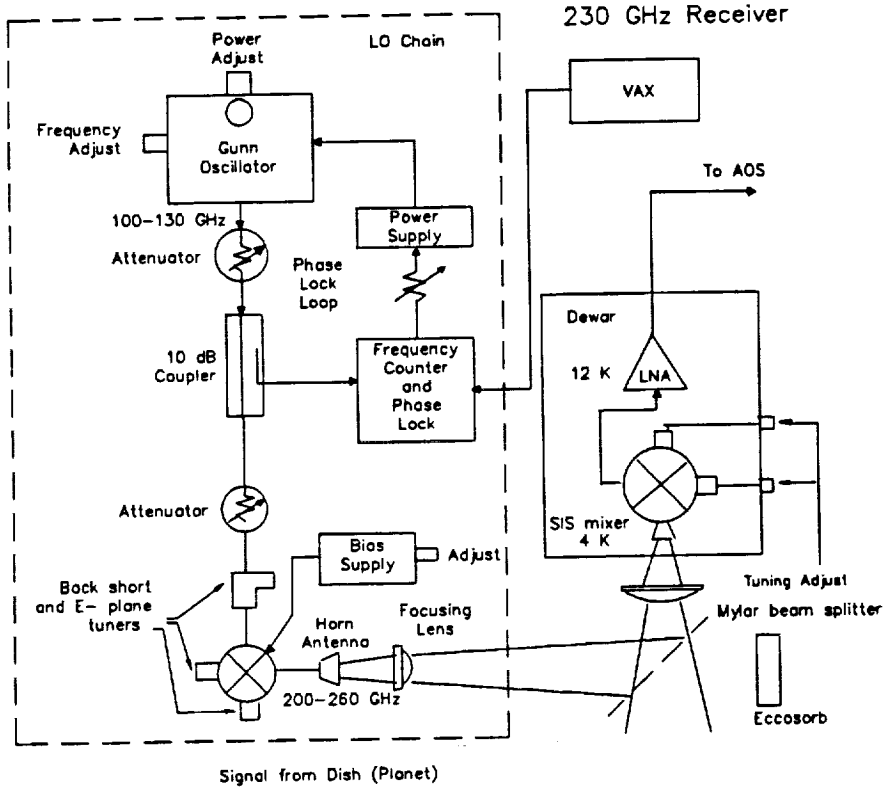

Figure 4.2: Block diagram of the CSO 230 GHz receiver.

involves the manual adjustment of several back shorts and attenuators in order to optimize the receiver temperature (see Figure 4.3). Because the two frequencies we chose were separated by approximately 15 GHz, it was not possible to use a single local (Gunn) oscillator (LO). Changing oscillators increased the time required to tune the receiver. We required between 45 minutes and 2 hours to achieve adequate receiver temperatures.

The receiver temperature can be computed by measuring the voltages at the receiver with a hot load (piece of absorber at ambient temperature $T_h \simeq 273$ K) and cold load (piece of absorber dipped in liquid nitrogen at a temperature $T_c \simeq 77$ K). The hot and cold load voltages (V_h and V_c, respectively) are related to the receiver temperature (T_{RX}) by

$$V_h = G[T_{RX} + T_h] \tag{4.6}$$

and

$$V_c = G[T_{RX} + T_c]. \tag{4.7}$$

The Y_{factor} is defined as

$$Y_{factor} = \frac{V_h}{V_c} = \frac{T_{RX} + T_h}{T_{RX} + T_c}. \tag{4.8}$$

Solving for T_{RX} with $T_h = 273$ K and $T_c = 77$ K yields

$$T_{RX} \simeq \frac{273 - 77\ Y_{factor}}{Y_{factor} - 1}. \tag{4.9}$$

The receiver temperatures (double side band) measured at 215 and 230 GHz were 220 K and 240 K respectively.

The primary objective of our observation was to detect the potential dip in Jupiter's spectrum resulting from H_2S absorption. Our approach was to use the total band width of the AOS essentially as a band pass filter or photometer at two or more frequencies. The emission is measured near the center of the H_2S line where the potential absorption from H_2S is at a maximum. The emission is then measured on either side (or both sides) of the line where the H_2S opacity is small

(*i.e.*, the *continuum*). In order to infer H_2S absorption, we need only measure a differential emission between two or more wavelengths. Lellouch *et al.* (1984) used a similar approach to search for PH_3 and HCN spectral features on Jupiter. A second objective of our observation was to obtain a reliable brightness temperature of Jupiter at this wavelength. This requires a precise estimate of the brightness temperature of Mars, which was used as the primary calibrator.

Figure 4.3 shows the potential effect of H_2S on Jupiter's spectrum at 216 GHz (1.4 mm). The dotted and solid lines are computed Jovian spectra with and without H_2S absorption, respectively. We also show the frequencies at which we observed Jupiter with the double side band CSO receiver. We observed Jupiter with the local oscillator (LO) centered at 215.3 GHz and 229.6 GHz. We were unable to observe at the low frequency tail of the H_2S line, because there were no available oscillators operating near 200 GHz.

We observed both Jupiter and Mars on (UT) 25 November 1990 with the LO centered at 215.3 GHz. The frequency of the H_2S line (216.7 GHz) is centered in the upper side band. We observed Mars first, then Jupiter, followed by Mars again, checking for variation in the observed temperature of Mars. We observed no variation in the temperature of Mars on this night.

We used the same procedure to observe the two planets on (UT) 26 November, 1990 at a frequency 229.6 GHz. This frequency was chosen so that the CO transition at 230.5 GHz, which has been observed in the spectrum of Mars, would be between the upper and lower side bands. Therefore, it would not interfere with the continuum of Mars. At this frequency, some variation occurred in the observed antenna temperature of Mars prior to and following the observation of Jupiter. This variation results in a large uncertainty in the observed temperature of Mars and thus a large uncertainty in the Mars/Jupiter ratio at this frequency. The receiver was then retuned to a center frequency of 215.3 GHz to repeat the observation of 25 November. We observed Mars followed by Jupiter. Because the

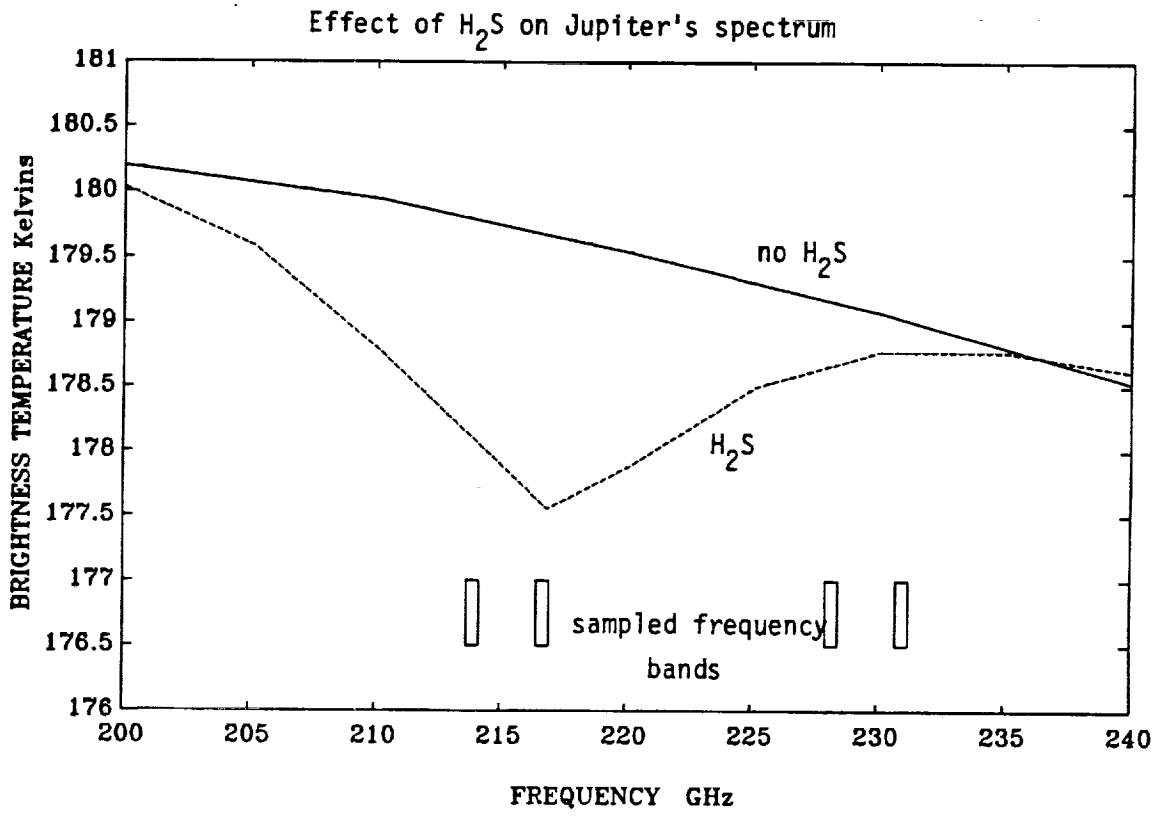

Figure 4.3: Effect of H_2S absorption at 216 GHz and frequencies at which we observed Jupiter with the double side band (DSB) CSO receiver. Dashed line: spectrum with H_2S absorption, solid line: spectrum without H_2S absorption.

elevation of Mars was low and weather conditions marginal after observing Jupiter, we were unable to observe Mars a second time.

Ideally, the observations of Jupiter should be made when the calibrator (Mars) is close to the source (Jupiter) in the sky. In that case, the effects of any temporal or spatial variation in the earth's atmospheric opacity would be limited. However, good observations of Jupiter relative to Mars can still be made even if the planets are not ideally positioned. During our observation, Jupiter reached zenith approximately 5 hours after Mars. We were careful to observe Jupiter and Mars at times when the atmospheric opacity was observed to be stable and both planets were at similar elevations. The amount of observing time satisfying these conditions was limited.

The airmass, M, is a term commonly used by astronomers to describe the elevation of the target. The airmass is related to the zenith angle θ (90 degrees - elevation) by

$$M = \sec(\theta) = \frac{1}{\mu}. \tag{4.10}$$

A plot of the airmasses of Jupiter and Mars is shown in Figure 4.4. Generally, observations should be made when $M < 1.5$. Jupiter and Mars were both positioned at $M < 1.5$ between 02:00 and 04:00 local time.

Chopping was accomplished by position switching or alternately pointing the telescope ON the source (planet) and then at a position in the sky OFF the source 5′ in either the + or - azimuth direction. The telescope remains both ON the source and OFF the source for a duration of 10 seconds. One scan of the source is defined as 4 ON/OFF cycles resulting in a total integration time of 80 seconds. The basic symmetric pattern is ON -OFF +OFF ON, where OFF is 5′ off the planet in the + and - azimuth directions. Normally, the scans alternately begin in the ON and OFF positions. This alternating pattern may be manually overridden.

The size of Jupiter is approximately equal to the beam width of the telescope. Therefore, telescope pointing is critical. Accurate telescope pointing is

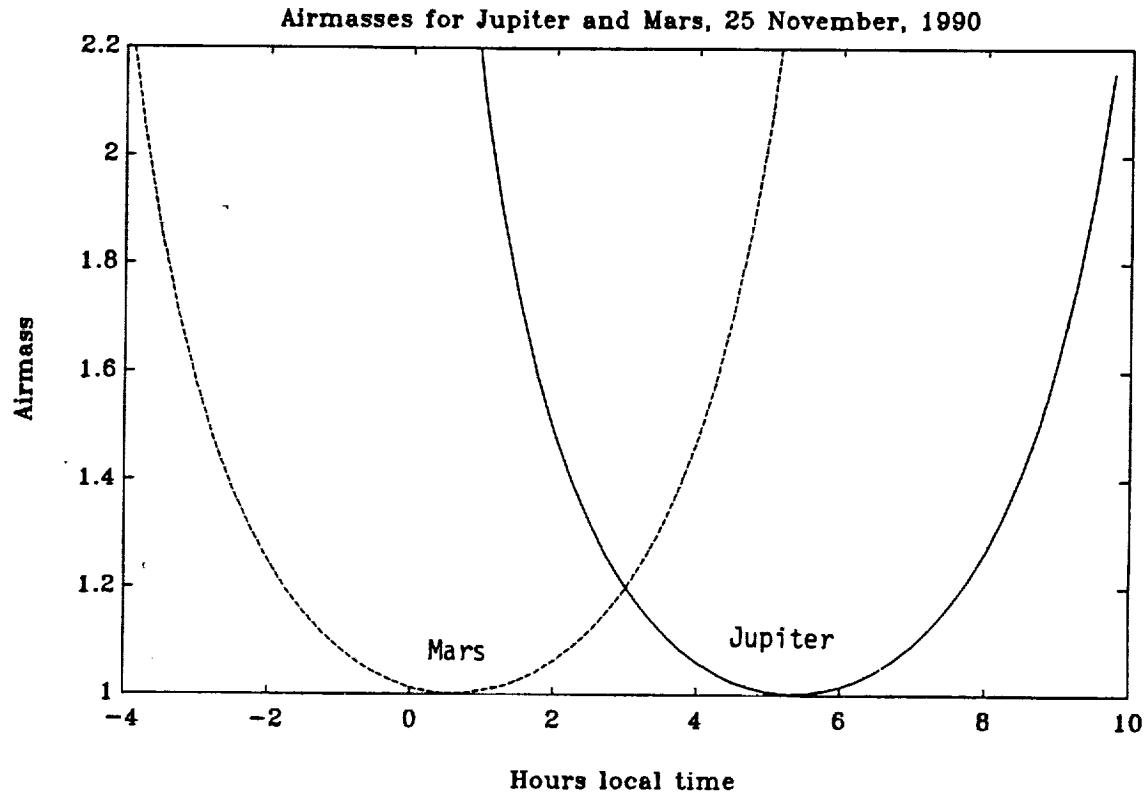

Figure 4.4: Plot of air masses of Jupiter and Mars on 26 November.

accomplished by constructing a five point map of the planet. An on-line program uses a Gaussian fit to position the planet in the center of the telescope beam. For observations of Jupiter, the telescope was typically repositioned after every other scan. The telescope was repositioned following every third or fourth scan of Mars. The pointing remained accurate to better than 4" (or $\sim$ 10%) between repositioning.

4.3 Calibration

Before each scan of the planet, the computer automatically executes a chopper wheel calibration scan. This calibration procedure removes the effects of the earth's atmospheric opacity. Because both our source and calibrator have finite and different angular sizes, additional calibration steps are required.

During the chopper wheel calibration scan, the computer controls a chopper wheel which located in front of the Cassegrain feed (between the secondary and tertiary mirrors). First, a hot (ambient temperature) load is positioned in the beam of the antenna. The back-end computer inserts the necessary attenuators to prevent the AOS from saturating. A voltage level, V_h, is measured with the AOS. The hot load is removed and the telescope is positioned on the sky (off source). A voltage, V_{sky}, is measured with the AOS. A calibration factor, Cal, is defined as

$$\mathrm{Cal} = \frac{V_h - V_{sky}}{V_{sky}} = \frac{G\,\alpha\,\beta\,\gamma\,T_h e^{-\tau}}{V_{sky}}, \tag{4.11}$$

(Phillips, 1989) where G is the system temperature to voltage conversion factor, α is called the hot spillover efficiency (1 - the fraction of power falling on the ground), β is the cold spillover efficiency (1 - the fraction of power falling on the sky), γ is the source coupling efficiency, and τ is the atmospheric opacity at the zenith angle in optical depths. A similar ratio, OO-scan (On/Off scan), is defined

for a scan of the source (planet)

$$\mathrm{OO-scan} = \frac{V_s - V_{\mathrm{sky}}}{V_{\mathrm{sky}}} = \frac{G\ \alpha\ \beta\ \gamma\ T_s e^{-\tau}}{V_{\mathrm{sky}}}. \tag{4.12}$$

where V_s is the voltage level of the source. Taking the ratio of the two quantities OO − scan and Cal yields

$$\frac{\mathrm{OO-scan}}{\mathrm{Cal}} = \frac{\beta\gamma T_s}{T_h} \tag{4.13}$$

or

$$T_s = \frac{T_h}{\beta\gamma}\frac{\mathrm{OO-scan}}{\mathrm{Cal}} \tag{4.14}$$

for double side-band observations. Since the value of $\beta\gamma$ is not known, the computer (CLASS data analysis package) gives a plot of the corrected source temperature (T_A^*) versus upper and lower side-band frequency where

$$T_A^* = \frac{2T_h}{\beta\gamma}\frac{\mathrm{OO-scan}}{\mathrm{Cal}}. \tag{4.15}$$

A typical Mars spectrum is shown in Figure 4.5.

For a source (planet) whose size is comparable to the size of the antenna beam, the product of the cold spillover efficiency, β, and the source coupling efficiency, γ, can be computed from:

$$\beta\gamma(\mathrm{MainBeam}) = \left[\frac{T_A^*(\mathrm{Planet})}{2T_{\mathrm{Planet}}}\right] \cdot \left[1 - \exp\left[-\left(\frac{D}{\Theta}\right)^2 \ln 2\right]\right]^{-1} \tag{4.16}$$

(Phillips, 1989) where D is the angle subtended by the planet, Θ is the beam width (FWHM), T_{Planet} is the actual brightness temperature of the planet, and T_A^* is the observed temperature (automatically corrected by the computer for atmospheric effects and telescope losses). Mars is an ideal calibrator, because it is both bright and compact. Because Mars has a tenuous atmosphere, its millimeter-wave spectrum is relatively flat (with the exception of a few narrow lines such as the CO line mentioned above). Its brightness temperature can be predicted with good accuracy. By assuming a value of T_{Mars} based on radiative transfer models and using the observed value of T_A^* (Mars), a value of $\beta\gamma$ can be computed. This value

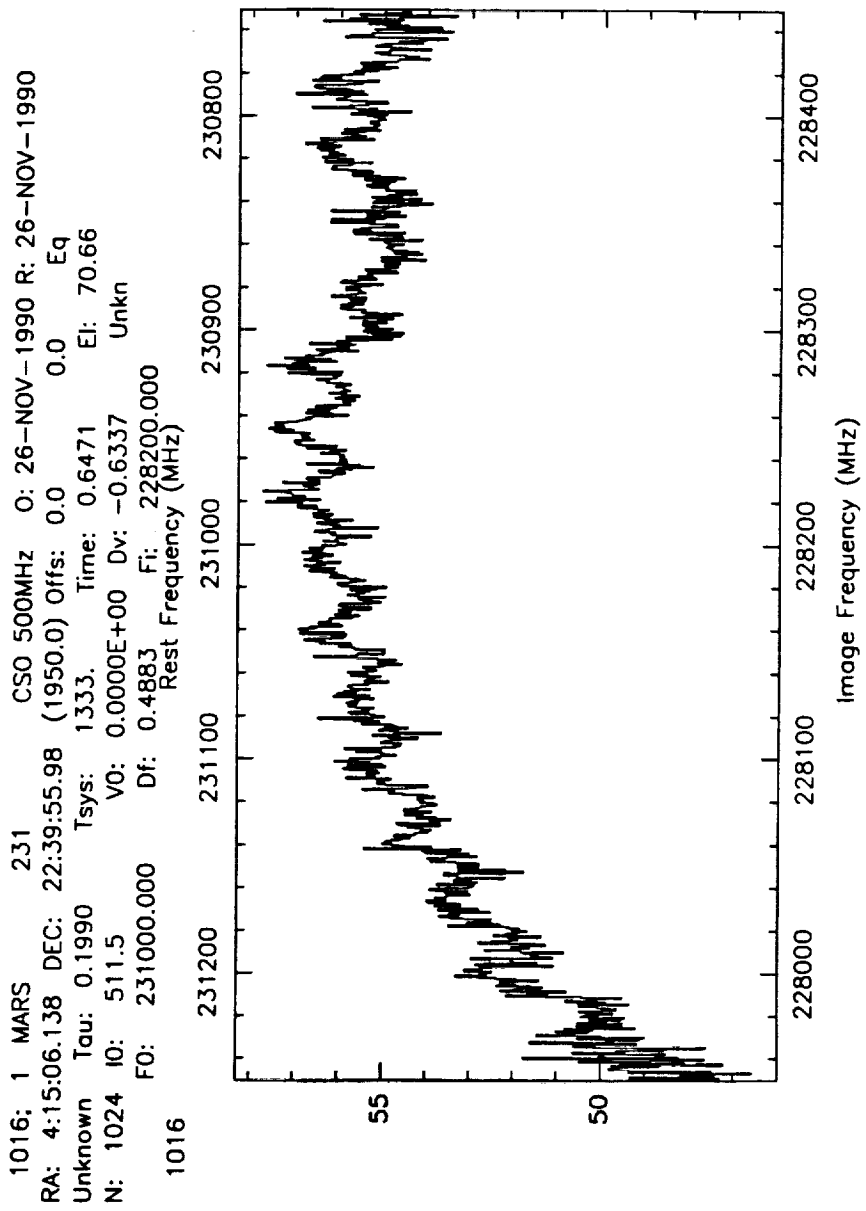

Figure 4.5: Typical observed Mars spectrum as produced by the CLASS data analysis package. Upper and lower side band frequencies are shown on the top and bottom horizontal axes, respectively.

of $\beta\gamma$ is then used to compute the brightness temperature of Jupiter, $T_{Jupiter}$, from the observed value T_A^* (Jupiter).

In Equation 4.16, the second term represents a correction for the partial filling of the antenna beam (Ulich *et al.*, 1980). We compute the size or diameter of the planets as viewed from the earth, D, (in arc seconds) from the precise earth to planet distance and the planet's radius. For Jupiter, we use an equatorial radius at the 1 bar level of 71495 km and an ellipticity of 0.065. This value is based on the radio occultation experiment aboard *Voyager* (Lindal *et al.*, 1986). We use a value of 3397 km for the Martian equatorial radius with an ellipticity of 0.0006. These are the same values as those used by Griffin *et al.* (1986). The exact earth to planet distances for Mars and Jupiter were taken from the Astronomical Almanac (1990). For Mars and Jupiter, the true geocentric distances were approximately 4.86 and 0.4 AU respectively. This yields a diameter of about 18″ for Mars and polar and equatorial diameters of 37.9″ and 40.5″ respectively for Jupiter. The effective diameter of Jupiter in Equation 4.16 is the geometric mean of the polar and equatorial diameters.

The beam width of the antenna is inversely proportional to the wavelength λ. The FWHM beam width of a parabolic reflector is

$$\Theta \simeq \frac{d}{\lambda\sqrt{\rho_a}}, \tag{4.17}$$

(Gagliardi, 1984) where d is the diameter of the reflector, and ρ_a is the antenna efficiency factor which is dependent on how the antenna aperture is electromagnetically illuminated. Because ρ_a is not precisely known, the beam width should be measured. In order to infer the beam width of the antenna (Θ), we obtained a map of Jupiter at 230 GHz from Schinckel (*private communication*, 1991). The contour plot is shown in Figure 4.6. We read off values from the two dimensional beam map of Jupiter at the equator (using linear interpolation between the contour lines) to develop a one dimensional beam map of Jupiter's equator. The map of Jupiter's equator was then deconvolved with a model of the expected emission

at Jupiter's equator which takes into account the effects of its oblate shape and limb darkening (see Section 3.1). Figure 4.7 shows the equatorial beam scan and the expected brightness temperatures of Jupiter's equator. The resulting antenna pattern is shown in Figure 4.8. The beam is Gaussian with a FWHM of 45.9″ at 230 GHz. Assuming that the antenna or illumination efficiency factor is constant over the range of 215.3 to 230 GHz, the FWHM at 215.3 GHz would be 49.0″.

We use brightness temperatures of 211.9 and 212.6 K for Mars at 216 and 230 GHz, respectively (Rudy *et al.*, 1987 and Rudy, *private communication*, 1991). Rudy's model accounts for both seasonal and longitudinal variation. The longitudinal variation in the Martian brightness temperature predicted by Rudy's model was less than 1 K or 0.5%. Since Rudy's model is extrapolated from observations at 2 and 6 cm, we have used an additional check. Ulich (1981) has developed the only empirical model for predicting the millimeter brightness temperature of Mars. Ulich's model is based on millimeter observations using absolute calibration. Ulich's model is limited in that it is based on observations at a single frequency (86 GHz or 3.5 mm). His model takes into account only seasonal variation and neglects longitudinal variation. At this frequency Rudy's model predicts the brightness temperatures over one Mars rotation to vary between 197 and 203 K. Ulich's empirical expression is

$$T_B(86\ \text{GHz}) = T_B'\left(\frac{R}{R_o}\right)^{1/2}, \tag{4.18}$$

where R is the heliocentric distance, $T_B' = 206.8 \pm 1.5$ K, and $R_o = 1.524$ AU. During our observation, $R = 1.50545$ AU. The resulting Martian brightness temperature using Equation 4.18 is 208.1 ± 1.5 K at 86 GHz. This temperature is within about 5% of Rudy's predicted brightness temperatures. Previous observers have arbitrarily assumed the uncertainty in the Martian brightness temperature to be ±10% or approximately ±20 K (see, *e.g.*, Griffin *et al.*, 1986). Although Rudy estimates that the uncertainty in his model is better than 10% (Rudy, *private communication*, 1991), we will conservatively assume the uncertainty in the

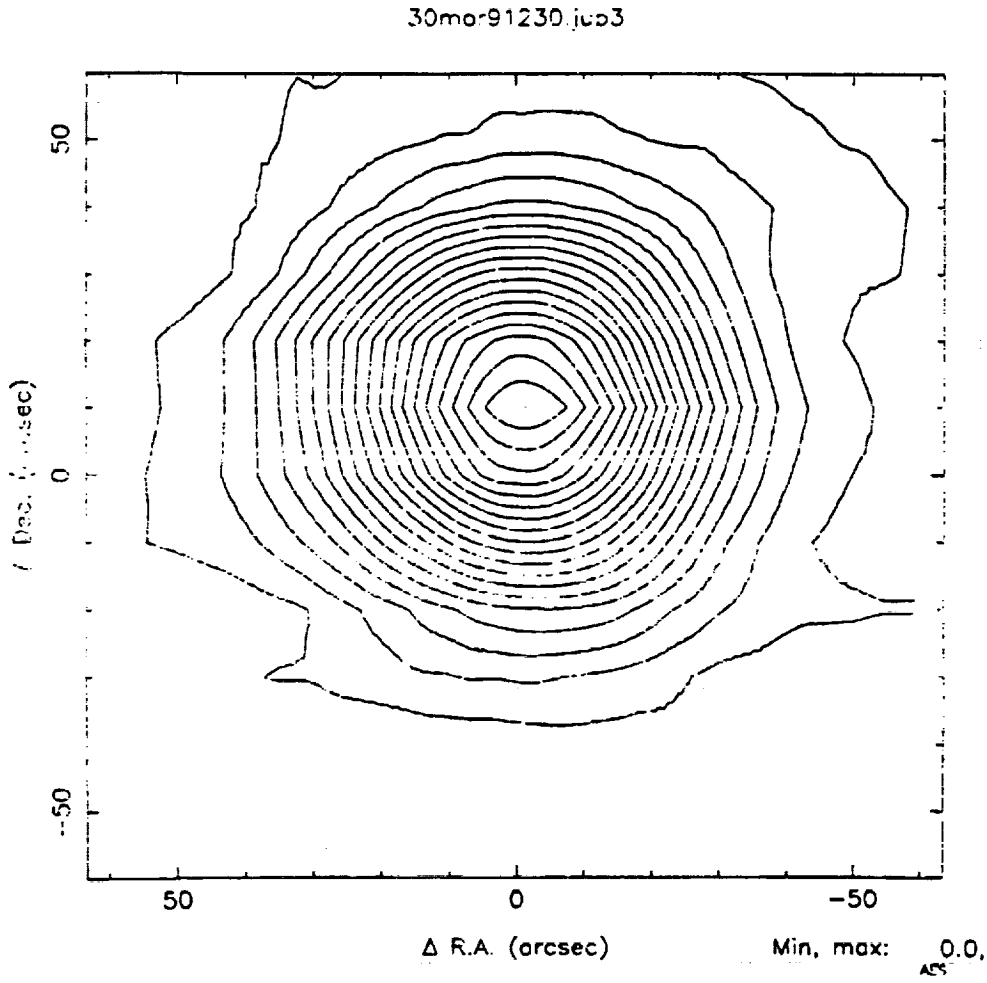

Figure 4.6: Map of Jupiter at 230 GHz.

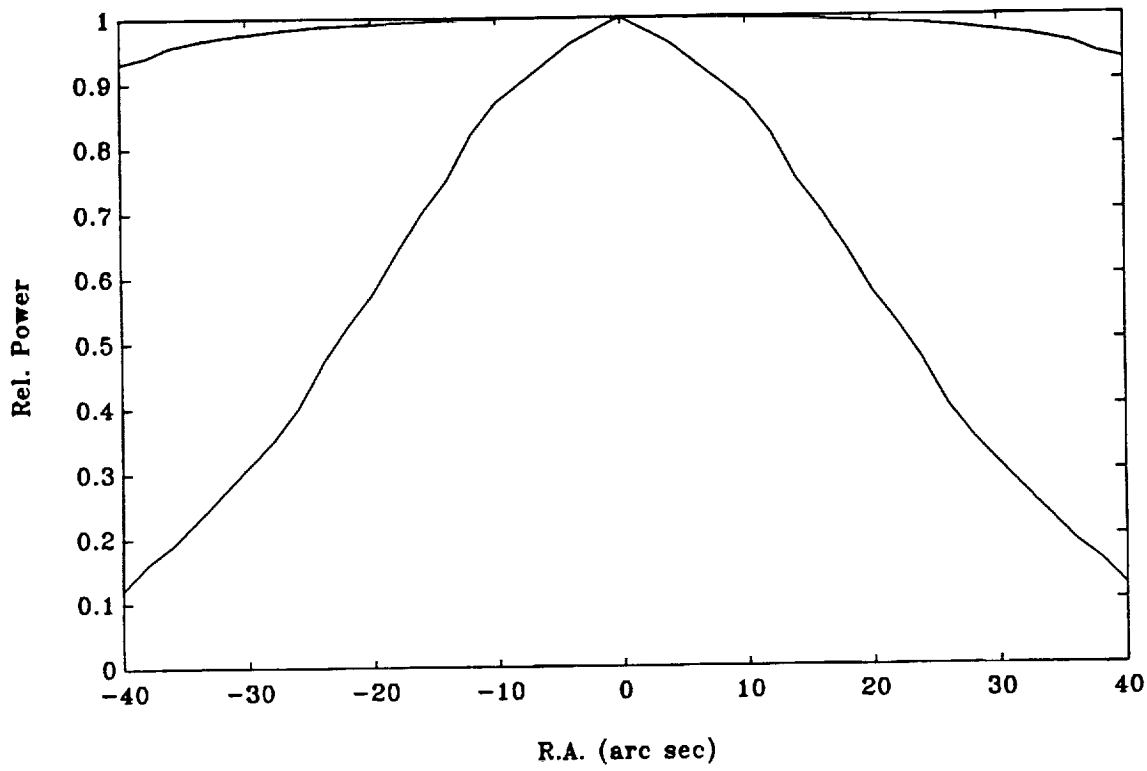

Figure 4.7: Equatorial cut through the beam map of Jupiter and the computed brightness temperature (normalized to 1) for an equatorial cut through Jupiter including limb darkening

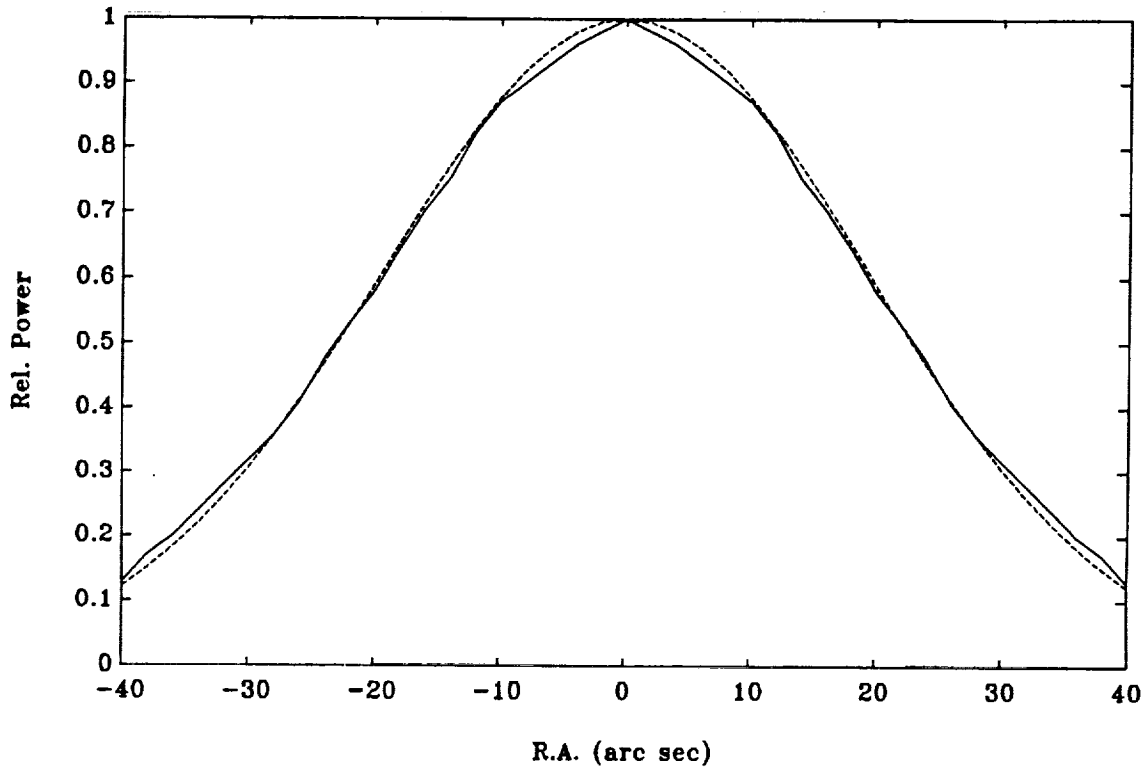

Figure 4.8: Plot of the beam shape of the CSO at 230 GHz; Solid line: Inferred beam shape of the CSO, dashed line: Gaussian beam with FWHM = 45.9″.

Martian brightness temperature to be 10%.

4.4 Atmospheric Conditions

The atmospheric opacity was monitored with a separate tipping radiometer or tau meter operated by the NRAO at 225 GHz. Plots of τ_z (the zenith optical depth) for 25 and 26 November are shown in Figures 4.9 and 4.10, respectively. These plots are good indicators of the atmospheric opacity and variability of the weather.

The tau meter records opacity as a function of altitude in only one direction. We checked the weather conditions frequently for local variation (*i.e.*, clouds). A 6 inch optical telescope (Paigeatron) mounted just below the CSO reflector and connected to a video display in the control room allowed us to monitor the visibility of the planets. Frequent trips outside the observatory were also required to observe local conditions.

Another indicator of the observing conditions is the system temperature (T_{sys}) which is defined as the system noise at the source elevation divided by the loss factor of the source or

$$T_{sys} = \frac{T_{RX} + (1 - \alpha e^{-\tau}) T_h}{\alpha \beta \gamma e^{-\tau}} \tag{4.19}$$

(Phillips, 1989). The voltages of the source (planet) and the sky (V_s and V_{sky}, respectively) are related to the receiver temperature (T_{RX}) by

$$V_{sky} = G[T_{RX} + (1 - \alpha e^{-\tau/\mu}) T_h] \tag{4.20}$$

and

$$V_s = G[T_{RX} + (1 - \alpha e^{-\tau/\mu}) T_h + \alpha \beta \gamma T_s e^{-\tau/\mu}], \tag{4.21}$$

where T_h is the temperature of the sky, and T_s is the temperature of the source. Substituting Equation 4.20 into Equation 4.11 yields

$$\mathrm{Cal} = \frac{\alpha e^{-\tau} T_h}{T_{RX} + (1 - \alpha e^{-\tau}) T_h}. \tag{4.22}$$

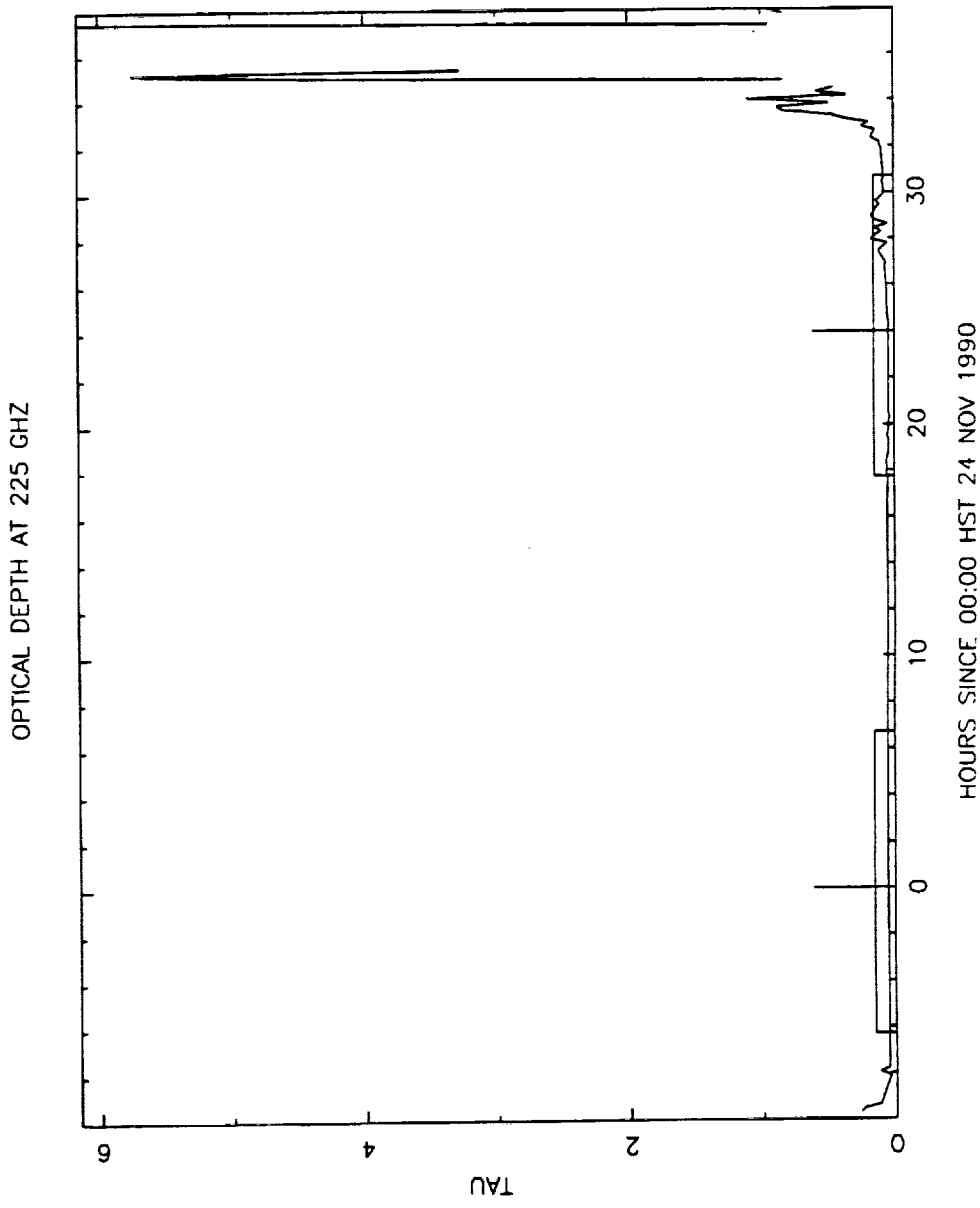

Figure 4.9: Plot of τ as a function of hour for 25 November.

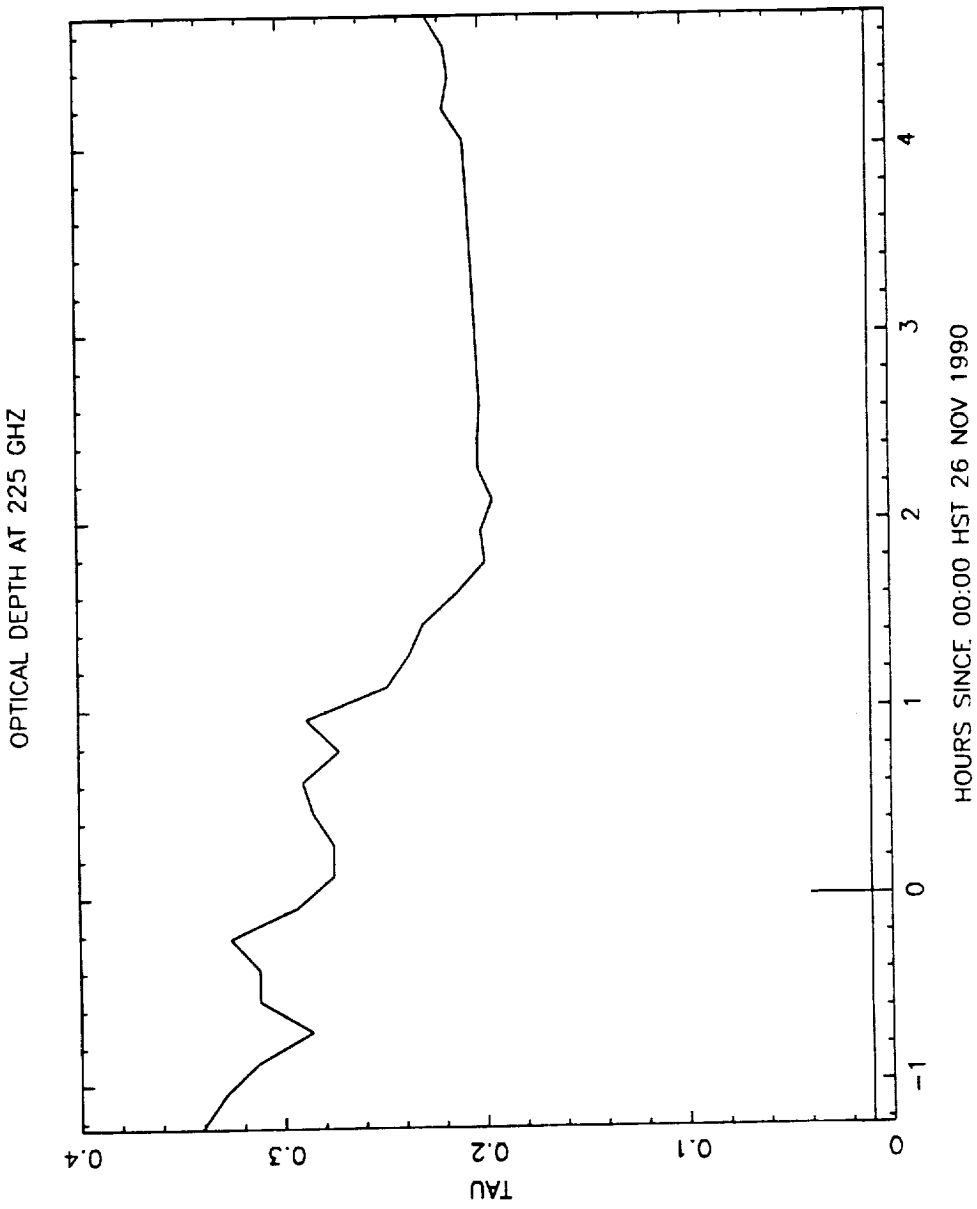

Figure 4.10: Plot of τ as a function of hour for 26 November.

Then, T_{sys} can be written as

$$T_{sys} = \frac{T_h}{\text{Cal}\ \beta\gamma}. \tag{4.23}$$

Because the quantity $\beta\gamma$ is not known, the computer gives the system temperature as

$$T_{sys} = \frac{T_h}{\text{Cal}}. \tag{4.24}$$

The system temperature for each scan is listed in Tables 4.1-4.3.

We were unable to observe on the first scheduled night of observation (24 November) due to poor weather conditions (low lying cumulus cloud and fog). We utilized this night by familiarizing ourselves with the receiver tuning process. The zenith optical depth (τ_z) was stable at 0.05 on 25 November for approximately three hours. As the night progressed, the humidity rose from an initial 20% to 100% at around 04:00 local time. At this time, fog was visible and observations were terminated. On 26 November, τ_z was higher but relatively stable at 0.2 for approximately four hours. The humidity was initially high (80%) and rose to 100% at 05:00. Fog was again visible, and we noted ice on the surface of the telescope at this time.

4.5 Data Analysis

Using the data analysis package CLASS, we fit a zero order baseline to the observed spectrum of each scan. The antenna temperature (T_A^*) corrected for atmospheric opacity is averaged over the 1024 channels of the AOS to reflect a mean and RMS deviation for in each scan. Tables 4.1-4.3 list T_A^*, the RMS noise, the system temperature (T_{sys}), and the zenith optical depth (τ) for each scan. Also listed is the position of the antenna at the beginning of the scan (ON or OFF source). We also note when the antenna was repositioned.

The overall observational uncertainty was dominated by scatter in the means of individual scans and not the base line ripple observed in a single scan. As

Table 4.1: Listing of observations (UT) 25 November 1990 at 216 GHz.

Scan	Source	T_A^* (K)	RMS (K)	T_{sys}	τ	ON/OFF	Comments
1001	Cal						Not pointed
1002	Cal						
1003	Mars	47.5	3.1			ON	
1004	Cal						
1005	Mars	43.2	1.5			OFF	
1006	Cal						
1007	Orion						
1008	Cal						
1009	Orion						
1010	Cal						
1011	Orion						
1012	Cal						
1013	Cal						
1014	Cal						
1015	Mars	59.4	1.5	963.2	0.055	OFF	2 Five-points
1016	Cal						
1017	Mars	58.4	1.4	959.2	0.056	ON	
1018	Cal						
1019	Mars	59.4	1.3	963.2	0.055	OFF	
1020	Cal						
1021	Mars	58.7	1.3	970.2	0.055	ON	1 Five-point
1022	Cal						
1023	Mars	59.3	1.4	966.7	0.055	OFF	
1024	Cal						
1025	Mars	60.4	1.2	980.6	0.055	ON	
1026	Cal						
1027	Mars	59.5	1.7	976.0	0.055	OFF	
1028	Cal						
1029	Mars	60.3	1.6	984.0	0.055	OFF	
1030	Cal						
1031	Cal						
1032	Cal						
1033	Cal						3 Five-points
1034	Cal						
1035	Jupiter	162.8	2.7	1013	0.055	ON	
1036	Cal						
1037	Jupiter	148.2	3.5	1013	0.055	OFF	1 Five-point
1038	Cal						
1039	Jupiter	159.1	1.9	991.3	0.055	ON	
1040	Cal						
1041	Jupiter	149.9	2.9	996.5	0.055	OFF	1 Five-point
1042	Cal						
1043	Jupiter	162.8	2.2	996.1	0.055	OFF	
1044	Cal						
1045	Jupiter	146.7	3.1	986.1	0.055	ON	1 Five-point
1041	Cal						
1048	Mars	57.8	0.8	962.5	0.055	ON	
1049	Cal						
1050	Mars	62.0	0.9	977.8	0.055	ON	1 Five-point
1051	Cal						
1052	Mars	61.1	0.9	974.3	0.055	OFF	
1053	Cal						
1054	Mars	61.7	1.1	993.0	0.055	OFF	
1055	Cal						
1056	Mars	57.5	0.9	989.3	0.055	OFF	

Table 4.2: Listing of observations (UT) 26 November 1990 at 230 GHz.

Scan	Source	T_A^* (K)	RMS (K)	T_{sys}	τ	ON/OFF	Comments
1001	Cal						Noisy
1002	Mars	47.5	3.1			ON	needs retuning
1003	Cal						
1004	Mars	45.2	1.5			OFF	
1005	Cal						
1006	Mars	40.8	0.8			ON	
1007	Cal						
1008	Mars	49.2	1.5			OFF	
1009	Cal						Retuned
1010	Mars	64.3	4.5	1348	0.213	ON	not pointed
1011	Cal						
1012	Mars	54.6	3.1	1341	0.213	OFF	
1013	Cal						2 Five-points
1014	Mars	55.5	2.2	1347	0.213	ON	
1015	Cal						
1016	Mars	54.7	2.0	1333	0.199	OFF	
1017	Cal						1 Five-point
1018	Mars	55.8	2.2	13382	0.199	ON	
1019	Cal						
1020	Mars	53.8	2.0	1344	0.199	OFF	
1021	Cal						
1022	Mars	64.2	2.0	1349	0.201	ON	
1023	Cal						
1024	Mars	54.0	2.1	1358	0.201	OFF	
1025	Cal						
1026	Cal						
1027	Cal						2 Five-points
1028	Jupiter	140.0	4.9	1557	0.202	OFF	
1029	Cal						2 Five-points
1030	Jupiter	170.5	2.6	1492	0.202	ON	
1031	Cal						1 Five-point
1032	Jupiter	142.7	5.5	1521	0.202	OFF	
1033	Cal						1 Five-point
1034	Jupiter	170.9	2.6	1484	0.202	ON	
1035	Cal						1 Five-point
1036	Jupiter	145.6	5.3	1477	0.202	OFF	
1037	Cal						1 Five-point
1038	Jupiter	145.3	4.7	1464	0.201	OFF	
1039	Cal						
1040	Jupiter	166.2	2.6	1455	0.201	ON	
1041	Cal						2 Five-points
1042	Mars	66.0	2.6	1441	0.201	ON	
1043	Cal						
1044	Mars	66.0	2.7	1446	0.201	ON	
1045	Cal						1 Five-point
1046	Mars	63.8	1.8	1451	0.201	OFF	
1047	Cal						
1048	Mars	64.3	1.3	1453	0.201	OFF	
1049	Cal						1 Five-point
1050	Mars	63.6	1.2	1461	0.201	OFF	
1051	Cal						
1052	Mars	60.9	1.3	1464	0.201	ON	
1053	Cal						
1054	Mars	61.0	1.4	1474	0.201	OFF	
1055	Cal						
1056	Mars	63.4	2.5	1473	0.201	ON	

Table 4.3: Listing of observations (UT) 26 November 1990 at 216 GHz.

Scan	Source	T_A^* (K)	RMS (K)	T_{sys}	τ	ON/OFF	Comments
1057	Cal						1 five point
1058	Mars	47.5	0.8	1512	0.226	ON	
1059	Cal						
1060	Mars	43.2	0.7	1540	0.224	OFF	
1061	Cal						
1062	Mars	40.8	0.9	1559	0.224	ON	
1063	Cal						
1064	Mars	49.2	1.5	1591	0.224	OFF	
1065	Cal						2 Five-points
1066	Jupiter	129.9	2.2	1093	0.224	OFF	
1067	Cal						
1068	Jupiter	144.0	2.8	1113	0.230	ON	
1069	Cal						2 Five-point
1070	Jupiter	132.5	2.2	1113	0.236	OFF	
1071	Cal						2 Five-points
1072	Jupiter	147.0	2.4	1117	0.236	ON	
1073	Cal						2 Five-point
1075	Cal						
1076	Cal						
1077	Orion						
1078	Cal						
1079	Orion						
1080	Cal						
1081	Orion						
1082	Cal						
1083	Orion						
1084	Cal						1 Five-point
1085	Jupiter	147.7	1.7	1079	0.221	ON	
1086	Cal						
1087	Jupiter	137.3	3.4	1083	0.218	OFF	
1088	Cal						1 Five-point
1089	Jupiter	147.4	1.9	1077	0.218	ON	
1090	Cal						
1091	Jupiter	139.3	3.1	1082	0.219	OFF	
1092	Cal						1 Five-point
1093	Jupiter	151.5	1.7	1085	0.219	ON	

expected, we are limited by sky noise and systematic errors, not the sensitivity of the receiver. The averaged observed temperatures, T_A^*, are listed in Table 4.4. We also list the computed values of $\beta\gamma$. The expected value of $\beta\gamma$ at 230 GHz is approximately 0.72. We note that our observed values of $\beta\gamma$ varied from night to night by as much as 10%.

The spectra of both Jupiter and Mars at the two observed frequencies are expected to be flat over band width (500 MHz) of the receiver. Both random and systematic processes contribute to the observed baseline ripple (see Figure 4.8). The ripple is still present after averaging several scans. Therefore, it must be systematic in part.

We also note systematic variations in the scans of both Jupiter and Mars. The recorded temperatures of Jupiter from scans which began with the telescope ON the planet were consistently higher than those from scans which began with the telescope OFF the planet (on the sky). We believe that the computer-controlled attenuators were not set to adequate levels on the scans which began OFF the source. This would cause the amplifiers to be driven into compression which would result in lower observed antenna temperatures. Compression of the amplifiers was also observed and confirmed independently by Schinckel (*private communication*, 1991). Therefore, we believe that only the scans which started ON Jupiter are reliable and include only these scans in our calculation of Jupiter's observed brightness temperatures. We list the data used to derive brightness temperatures for Jupiter at 215 and 230 GHz in Table 4.5. The uncertainty in the relative brightness temperatures of Jupiter, $T_{Jupiter}$, for individual nights is the quadratic sum of the observed uncertainties in T_A^* for Mars and Jupiter (note: This does not include the additional $\pm 10\%$ uncertainty in the absolute temperature of Mars).

Our observed brightness temperatures of Jupiter and those of previous observations near 1.4 mm are reported in Table 4.6. The first uncertainty represents the 1σ statistical uncertainty in the Mars/Jupiter ratio appropriate for searching

Table 4.4: Observed antenna temperatures.

Freq. (GHz)	Date (UT)	Source	$T_A^* \pm 1\sigma$ (K)	$\beta\gamma$	Comments
215.31	11/25/90	Mars	59.7±0.4	0.825	All scans (2 sets)
215.31	11/25/90	Jupiter	154.9±6.7		All scans (1 set)
			161.6±1.2		scans starting ON source only
			148.2±0.9		scans starting OFF source only
215.31	11/26/90	Mars	51.4±0.6	0.713	All scans (1 set)
215.31	11/26/90	Jupiter	141.8±6.4		All scans (2 sets)
			147.5±1.2		scans starting ON source only
			134.7±2.5		scans starting OFF source only
229.60	11/26/90	Mars	60.5±4.4	0.743	All scans (2 sets)
			54.8±0.4	0.673	Low's only
			63.6±0.7	0.782	High's only
229.60	11/26/90	Jupiter	154.5±12.9		All scans (1 set)
			169.2±1.5		scans starting ON source only
			143.4±1.3		scans starting OFF source only

Table 4.5: Observational data used to computed Jupiter's brightness temperature.

Freq. (GHz)	Date (UT)	$T_A^* \pm 1\sigma$ Mars	$T_A^* \pm 1\sigma$ Jupiter	T_{Mars} assumed	$T_{Jupiter}$ observed
215.31	11/25/90	59.7±0.4	161.6±1.2	211.9	166.3 ± 1.7
215.31	11/26/90	51.4±0.6	147.5±1.2	211.9	175.0 ± 2.5
229.60	11/26/90	60.5±4.4	169.2±1.5	212.6	178.1 ± 13.0
229.60	11/26/90	54.8±0.4	169.2±1.5	212.6	196.7 ± 2.3
229.60	11/26/90	63.6±0.7	169.2±1.5	212.6	169.4 ± 2.4

for possible spectral features. The second uncertainty includes an additional 10% uncertainty in the assumed brightness temperature of Mars required for *absolute* brightness temperature measurements. Our observed brightness temperatures are in good agreement with previous observations at wavelengths near 1.4 mm (Rather *et al.*, 1974, Courtin *et al.*, 1977, Ulich *et al.*, 1984 and Griffin *et al.*, 1986). All of the previous observations were made with broadband filters (see also Table 3.3) and only the observations of Courtin *et al.* (1977) and Griffin *et al.* (1985) used Mars as a calibrator. Rather *et al.* (1974) and Ulich *et al.* (1984) somewhat arbitrarily assigned brightness temperatures of 150 and 165 K, respectively, to Jupiter based on their observations of several planets and previously observed planetary brightness temperatures at longer and shorter wavelengths.

Finally, we chose to utilize the spectral information available in the 1024 channels of the AOS to obtain additional calibration information and to check for the unlikely presence of narrow line core emission from H_2S in Jupiter's stratosphere. We observed line emission from the core of the Orion molecular cloud on

Table 4.6: Observed Jovian brightness temperatures near 1.4 mm.

Wavelength (mm)	Freq (GHz)	T_B^a (K)	Calibrator	$\Delta\nu$ (GHz)	Reference
1.30	231	175.0±2.5(18)	Mars	3.2	This work
1.32	227	170.9±3.9(18)	Mars	70	Griffin *et al.*(1986)
1.32	227	165±8(18)	planets	39	Ulich *et al.*(1984)
1.39	216	178.11±13.0(22)	Mars	3.2	This work
1.40	214	148±16(22)[b]	planets	275	Rather *et al.*(1975)
1.40	214	168±11(20)[c]	Mars	210	Courtin *et al.*(1977)

[a]First uncertainty is 1σ observational uncertainty,
the second uncertainty includes an additional 10% for absolute calibration

[b]Brightness temperatures as corrected in Berge and Gulkis (1976)

[c] Recalculated using beam correction factor in Ulich (1980)

both nights at 215.3 GHz in addition to the two planets. The hydrogen sulfide line emission from Orion at 216.7 GHz (centered in the upper side band) was clearly visible after one scan. If an H_2S emission core is present in the scans of Jupiter, it will also appear in the center of the upper side band. An H_2S mixing ratio of close to 1×10^{-6} would have to be present in the stratosphere in order to detect an emission core. Based on the strict upper limits (as low as 1×10^{-9}) which have been placed on the abundance of H_2S in Jupiter's stratosphere at several wavelengths from the infrared to uv (summarized by Larson *et al.*, 1984), no such feature is expected. Figure 4.11 shows an average of all scans of Jupiter at 215.3 GHz for 25 November. Indeed, no H_2S emission core is visible.

The line intensities in the spectra of Orion also provide a secondary calibration source. An averaged spectrum of Orion observed on 26 November is shown in Figure 4.12. There is good agreement between our spectra of Orion (26 November) and those of Sutton *et al.* (1985). However, the line intensities of the averaged spectra taken on 25 November are significantly higher than those of Sutton *et al.* (1985) which could be due to a side band ratio $\neq 1$. This might also explain the high value of $\beta\gamma$ observed on 25 November. Therefore, we believe the 215.3 GHz observation on 26 November to be more reliable than the 25 November observation.

4.6 Observational Results

Figure 4.13 shows several synthetic emission spectra of Jupiter near 216 GHz using the radiative transfer and thermochemical model described in Chapter 3. We have computed the Jupiter's emission using the NH_3 and H_2S vertical distributions shown in Figure 3.9. Our observed brightness temperatures and corresponding error bars are also shown along with several other previous observations.

We were unable to obtain repeatable observations at individual frequencies

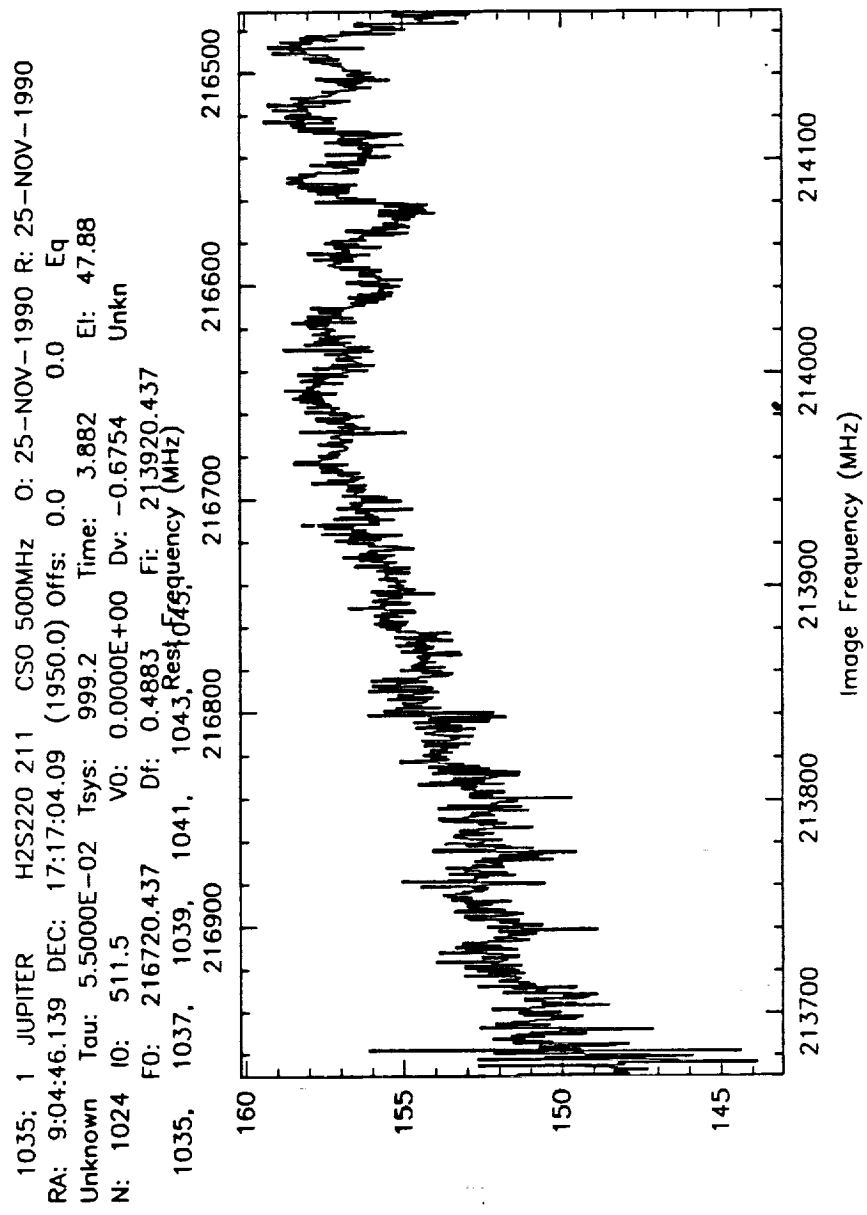

Figure 4.11: Average of Jupiter scans at 215.3 GHz for 25 November.

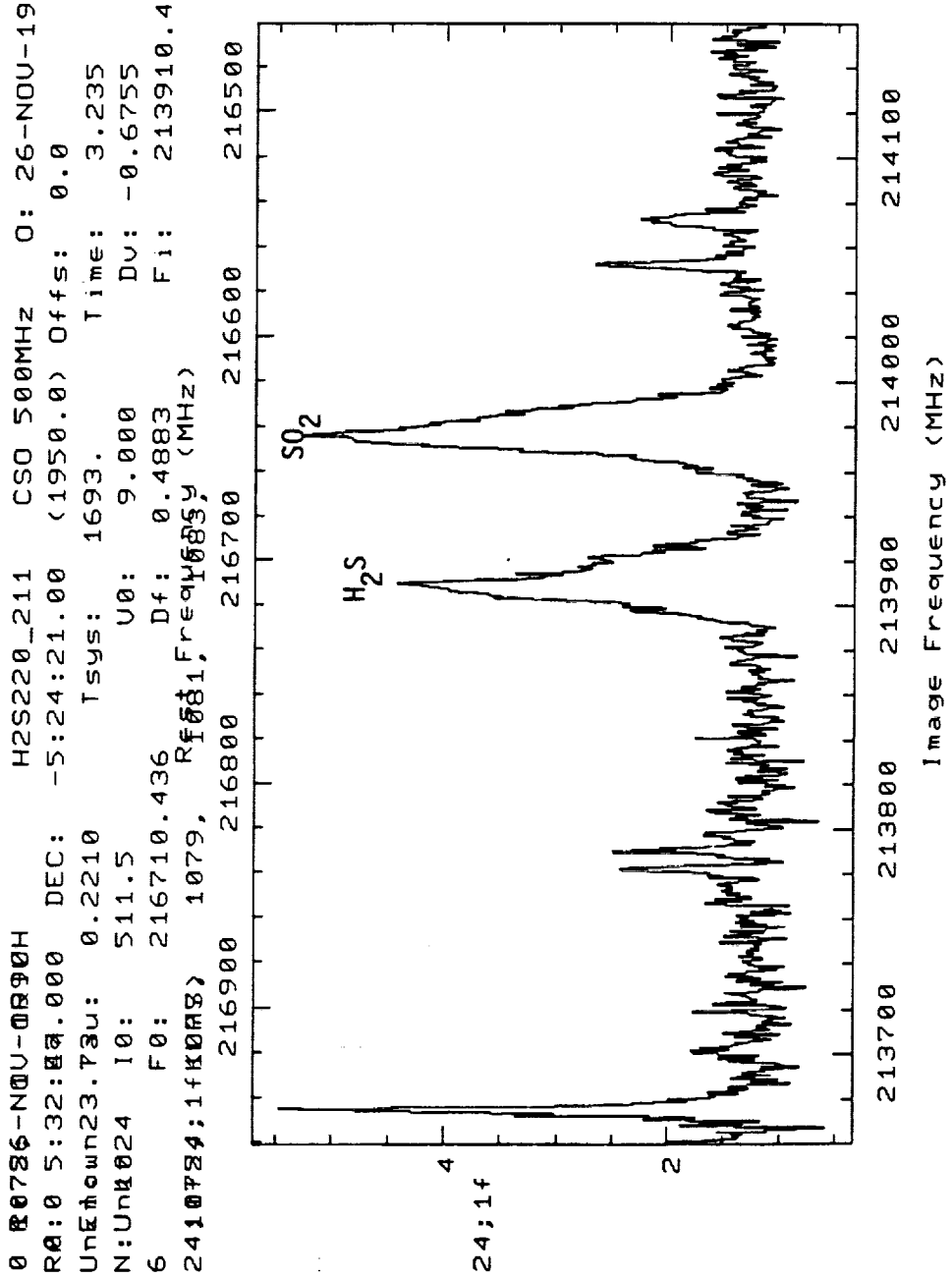

Figure 4.12: Average of Orion scans at 215.3 GHz for 26 November.

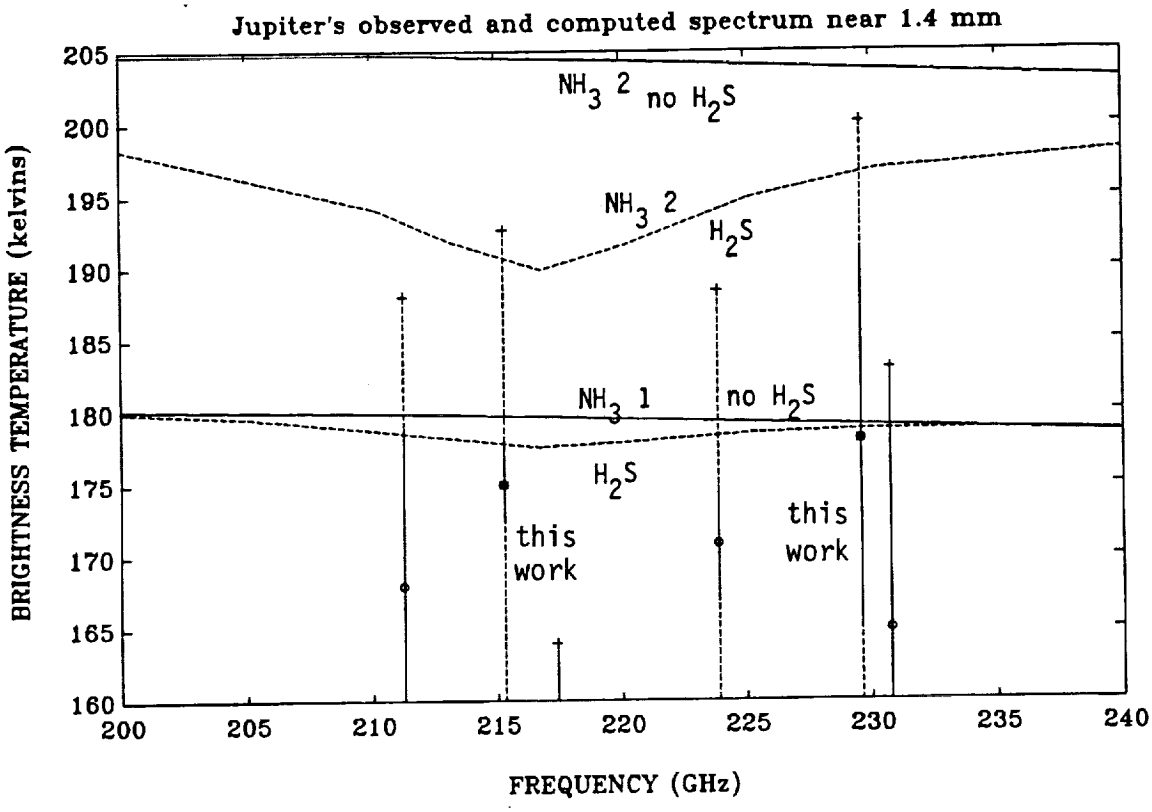

Figure 4.13: Observed spectrum of Jupiter near 216 GHz. •: our observations; o: other observations from Table 4.6. Theoretical spectra using distributions in Figure 3.9, solid line: NH_3, H_2O, and pressure-induced opacity only; dashed line: H_2S opacity added.

over several nights due to poor weather conditions. The uncertainties for our observation (especially for the single observation at 229.6 GHz) are large. Therefore, we did not detect a statistically significant difference in emission due to H_2S at the two wavelengths. Although we were unable to set tighter limits on the H_2S abundance in Jupiter's atmosphere, our results reinforce previous limits summarized by Larson *et al.*, 1985. Even though we did not achieve our primary objective of detecting H_2S gas, we were able to measure Jupiter's brightness temperature relative to Mars at the highest spectral resolution recorded at this wavelength.

CHAPTER 5

Summary and Conclusion

5.1 Uniqueness of Work

This research makes contributions in the areas of both planetary science and millimeter-wave measurements. The major contributions are summarized below:

1. Conducted first laboratory measurements of gaseous NH_3 opacity at Ka-band ($\nu = 32 - 40$ GHz, $\lambda = 7.5 - 9.38$ mm) under simulated Jovian conditions

2. Conducted first laboratory measurements of gaseous NH_3 opacity at W-band ($\nu = 94$ GHz $\lambda = 3.2$ mm) under simulated Jovian conditions

3. Developed new parameterization of the Ben-Reuven line shape for computing the absorptivity of NH_3 under Jovian conditions

4. Conducted first laboratory measurement of the hydrogen and helium broadened line width of gaseous H_2S at 1.4 mm

5. Documented for the first time new techniques in millimeter-wave measurements (*e.g.*, laser tuning of the resonator) and documented for the first time solutions to problems which occur in millimeter-wave measurements (*e.g.*, dielectric loading)

6. Incorporated for the first time the results of the millimeter-wave laboratory absorption measurements of NH_3 and H_2S into a radiative transfer model and computed synthetic emission spectra from the four giant planets

7. Developed new expressions for computing the radio opacity of pressure-induced absorption from H_2-H_2, H_2-He and H_2-CH_4 pairs and water vapor under Jovian conditions

8. Demonstrated that Jupiter's observed millimeter-wave emission is entirely consistent with synthetic spectra in which NH_3 is the primary source of opacity

9. Observed Jupiter at 1.4 mm for the first time using a high resolution receiver and obtained a reliable brightness temperature of Jupiter using Mars as the calibration standard

This research has culminated in the publication of several journal papers: Joiner *et al.* (1989), Joiner and Steffes (1991), and Joiner *et al.* (1991). This research has also been presented as several conference reports: Joiner *et al.* (1987), Joiner and Steffes (1988), Joiner and Steffes (1989), Joiner and Steffes (1990a,b).

5.2 Suggestions for Future Research

Although we were unable to obtain a positive detection or H_2S or set new upper limits on the H_2S abundance in Jupiter's atmosphere, the search for H_2S at millimeter wavelengths should not be abandoned. Poor weather conditions and instrumental difficulties contributed to large uncertainties in our observation. However, given more ideal conditions, the statistical uncertainties could be significantly reduced and systematic effects eliminated. In order to reduce the observational uncertainty, the integration time must be increased (*i.e.*, observations should be repeated over several days). Weather conditions must be exceptional in order to eliminate any variations in the observed temperatures of Jupiter and Mars caused by variations in the earth's atmospheric opacity. In addition, observations should be made at a minimum of three frequencies, corresponding to the center of the

H_2S line and on *both* sides of the line, in order to achieve a convincing detection of the pressure-broadened line.

Improvements in millimeter-wave technology will make the detection of broad spectral features (*i.e.*, pressure-broadened lines in planetary atmospheres) more feasible in the future. Wide band oscillators coupled with computer-controlled tuning will significantly reduce the time required to tune receivers. In addition, new instruments which can be mounted on existing millimeter and submillimeter antennas, such as Fourier Transform Spectrometers, will be better suited for the detection of broad spectral features. In the future, spectrometers with the proper resolution (on the order of GHz) for planetary spectroscopy will be utilized to improve upon the results obtained with the multi-wavelength approach. Improved calibration techniques will reduce the large uncertainty that presently exists in the absolute calibration of millimeter planetary observations.

Although this research represents great strides in the understanding of the millimeter-wave spectra of the Jovian planets, more microwave and millimeter-wave laboratory measurements are needed in order to fully interpret all of the available planetary observations. For example, measurements of the millimeter dielectric properties of solid NH_3 and NH_4SH are needed to accurately assess the potential effect of cloud condensates on the millimeter-wave spectra of the giant planets. Absorption measurements of pressure-broadened H_2S at centimeter wavelengths are needed in order to interpret the centimeter emission from Uranus and Neptune. In addition, a measurement of the equilibrium constant for the reaction of NH_3 and H_2S to form solid NH_4SH is needed in order to accurately predict the altitude at which the putative NH_4SH cloud will form. It is hoped that this research has provided the initiative for continued exploration of the millimeter-wave spectrum as part of the study of the Jovian planets.

BIBLIOGRAPHY

ASTRONOMICAL ALMANAC 1990. U. S. Naval Observatory, U. S. Govt. Printing Office, Washington, D. C.

ANDERS, E. AND N. GREVESSE 1989. Abundances of the elements: meteoritic and solar. *Geochim. Cosmochim. Acta* **53**, 197-214.

ATREYA, S. K.AND P. N. ROMANI 1985. Photochemistry and clouds of Jupiter, Saturn, and Uranus. In *Recent advances in planetary meteorology.* ed. G. E. Hunt. Cambridge Univ. Press, Cambridge, 17-68.

BAARS, J. W. M., R. GENZEL, I. I. PAULINY-TOTH, AND A. WITZEL 1977. The absolute spectrum of Cas A: an accurate flux density scale and a set of secondary calibrators. *Astron. Astrophys.* **61**, 99-106.

BACHET, G., E. R. COHEN, P. DORE, AND G. BIRNBAUM 1983. The translational-rotational absorption spectrum of hydrogen. *Can. J. Phys* **61**, 591-603.

BATTAN, L. J. 1973. *Radar Observation of the Atmosphere.* University of Chicago Press, Chicago.

BEN-REUVEN, A. 1966. Impact broadening of microwave spectra. *Phys. Rev.* **145**, 7-22.

BERGE, G. L., AND S. GULKIS 1976. Earth-based radio observation of Jupiter: Millimeter to meter wavelengths. In *Jupiter* (T. Gehrels, Ed.), 621-692. Univ. of Arizona Press, Tuscon.

BEZARD, B., A. MARTEN, J. P. BALUTEAU, D. GAUTIER, J. M. FLAUD, AND C. CAMY-PEYRET 1983. On the detectability of H_2S in Jupiter. *Icarus* **55**, 259-271.

BJORAKER, G. L., H. P.LARSON, AND V. G. KUNDE 1986A. The gas composition of Jupiter derived from 5 μm airborne spectroscopic observations. *Icarus* **66**, 579-609.

BJORAKER, G. L., H. P.LARSON, AND V. G. KUNDE 1986B. The abundance and distribution of water vapor in Jupiter's atmosphere *Astrophys. J.* **311**, 1058-1072.

BORYSOW, J., L. TRAFTON, AND L. FROMMHOLD 1985. Modeling of Pressure-Induced Far-Infrared Absorption Spectra: Molecular Hydrogen Pairs. *Astrophys. J.* **296**, 644-654.

BRIGGS, F. H., AND P. D. SACKETT 1989. Radio observations of Saturn as a probe of its atmosphere and cloud structure. *Icarus* **80**, 77-103.

CRC PRESS 1983. *CRC Handbook of Chemistry and Physics* (R. C. Weast, Ed.). CRC Press, Boca Raton, FL.

CHEDIN, A., N. HUSSON, N. A. SCOTT, I. COHEN HELLALET, A. BERROIR 1982. GEISA data bank (No 3).

COGDELL, J. R., J. H. DAVIS, B. T. ULRICH, AND B. J. WILLS 1975. Flux density measurements of radio sources at 2.14 millimeter wavelength. *Astrophys. J.* **196**, 363-368.

COLLIN, R. E. 1966. *Foundations for Microwave Engineering.* McGraw-Hill, New York.

COURTIN, R., N. CORON, T. ENCRENAZ, R. GISPERT, P. BRUSTON, J. LEBLANC, G. DAMBIER, A. VIDAL-MADJAR 1977. Observations of giant planets at 1.4 mm and consequences on the effective temperatures. *Astron. Astrophys.* **60**, 115-123.

DEPATER, I., AND S. T. MASSIE 1985. Models of the millimeter-centimeter spectra of the giant planets. *Icarus* **62**, 143-171.

DEPATER, I. 1986. Jupiter's Zone Belt Structure at Radio Wavelengths: II. Comparison of Observations with Atmosphere Calculations. *Icarus* **68**, 344-365.

DEPATER, I., P. N. ROMANI AND S. K. ATREYA 1989. Uranus deep atmosphere revealed. *Icarus* **82**, 288-313.

DEPATER, I., P. N. ROMANI AND S. K. ATREYA 1991. Possible microwave absorption by H_2S gas in Uranus' and Neptune's atmospheres. *Icarus* **91**, 220-233.

DEPATER, I. AND M. RICHMOND 1989. Neptune's microwave spectrum from 1 mm to 20 cm. *Icarus* **80**, 1-13.

DEIRMENDJIAN, D. 1969. *Electromagnetic Scattering on Spherical Polydispersions*, American Elsevier Publishing Co, Inc., New York.

DORE, P., L. NENCINI, AND G. BIRNBAUM 1983. Far infrared absorption in normal $H_2$from 77 to 298 K. *J. Quant. Spec. Rad. Trans* **30**, 245-253.

FLAUD, J. M., C. CAMY-PEYRET, AND J. W. C. JOHNS 1983. The far infrared spectrum of hydrogen sulfide. *Can. J. Phys.* **61**, 1462-1473.

GAGLIARDI, R. M. 1984. *Satellite Communications*, Lifetime Learning Publications, Wadsworth, Inc., Belmont, CA.

GASIEWSKI, A. J. 1990. Microwave radiative transfer in hydrometers. In *Atmospheric Remote Sensing by Microwave Radiometry* (M. A. Janssen, ed.) To be published by John Wiley and sons.

GAUT N. E. AND E. C. REIFENSTEIN III 1971. Environmental Research and Technology, Inc., Report No. 13, Lexington, MA.

GOODMAN, G. C. 1969. Models of Jupiter's atmosphere *Ph. D. thesis*, University of Illinois, Urbana.

GRIFFIN, M. J., P. A. R. ADE, G. S. ORTON, E. I. ROBSON, W. K. GEAR, I. G. NOLT, AND J. V. RADOSTITZ 1986. Submillimeter and millimeter observations of Jupiter. *Icarus* **65**, 244-256.

GROSS, E. P. 1955. Shape of collision-broadened spectral lines. *Phys. Rev.* **97**, 395-403.

GROSSMAN, A. W. 1990. Microwave imaging of Saturn's deep atmosphere and rings. *Ph. D. thesis*, California Institute of Technology, Pasadena.

GULKIS, S. 1987. Radio astronomy, planetary. *Encycl. Phys. Sci. Tech.*, Vol. II, 633-654.

GULKIS, S. AND I. DEPATER 1984. A review of the millimeter and centimeter observations of Uranus. In *Uranus and Neptune: Proc. of a workshop held in Pasadena, CA, Feb. 6-8, 1984*, NASA Conf. Publ. 2330, 225-262.

HELMINGER, P. AND F. C. DELUCIA 1972. Pressure broadening of hydrogen sulfide. *J. Quant. Spectrosc. Rad. Trans.* **17**, 751-754.

HOFSTADTER, M. D., G. L. BERGE AND D. O. MUHLEMAN 1990. Vertical motions in the Uranian atmosphere: an analysis of radio observation. *Icarus* **84**, 261-267.

HOFSTADTER, M. D. AND D. O. MUHLEMAN 1988. Latitudinal variations of ammonia in the atmosphere of Uranus: an analysis of microwave observations. *Icarus* **81**, 396-412.

JOINER, J., JENKINS, J. M., AND STEFFES, P. S., (1987). Laboratory Measurements of the Opacity of Gaseous Ammonia (NH_3) in the 7.3 - 8.3 mm (36-41 GHz) Range Under Simulated Conditions for the Jovian Atmospheres, *Bull. Amer. Astron. Soc.* **19**, 838.

JOINER, J., JENKINS, J. M., AND STEFFES, P. S., (1988). Millimeter-wave Measurements of the Opacity of Gaseous Ammonia (NH_3) Under Simulated Conditions for the Jovian Atmospheres, *Bull. Amer. Astron. Soc.* **20**, 867.

JOINER, J., P. G. STEFFES, AND J. M. JENKINS 1989. Laboratory measurements of the 7.5-9.38 mm absorption of gaseous ammonia (NH_3) under simulated Jovian conditions. *Icarus* **81**, 386-395.

JOINER, J., AND STEFFES, P. G. (1989). Models of the Millimeter-wave Emission of the Jovian Atmosphere Utilizing Laboratory Measurements of Gaseous Ammonia (NH_3). *Bull. Amer. Astron. Soc.* **21**, 945.

JOINER, J., AND STEFFES, P. G. (1990). Study of the Millimeter-wave Absorbing Constituents in the Jovian Atmospheres. *Bull. Amer. Astron. Soc.* **22**, 1032.

JOINER, J., AND STEFFES, P. G. (1990). Measurement of the Pressure-Broadened Linewidths of Gaseous Hydrogen Sulfide (H_2S). Poster presented at Second International Conference on Laboratory Research for Planetary Atmospheres.

JOINER, J., AND P. G. STEFFES 1990. Modeling of Jupiter's millimeter-wave emission utilizing laboratory measurements of ammonia (NH_3) opacity. *JGR:Planets, accepted.*

JOINER, J., P. G. STEFFES, AND K. S. NOLL 1990. Search for sulfur (H_2S) on Jupiter at millimeter wavelengths. Submitted to *IEEE Trans. Microwave Theor. Tech.*

KLEIN, M. J. AND S. GULKIS 1978. Jupiter's atmosphere: Observations and interpretation of the microwave spectrum near 1.25 cm wavelength. *Icarus* **25**, 44-60.

KLEIN, M. J., M. A. JANSSEN, S. GULKIS AND E. T. OLSEN 1978. Saturn's microwave spectrum: Implications for the atmosphere and the rings. In *The Saturn System*, NASA CF-2068, (D. M. Hunten and D. Morrison, Eds.), 195-216. NASA, Washington, D. C.

KRAUS, G. F., J. E. ALLEN, JR., AND L. C. COOK 1989. Vapor pressure measurements of hydrogen sulfide. *Bull. Amer. Astron. Soc.* **21** 948.

LARSON, H. P., D. S. DAVIS, R. HOFMAN, AND G. L. BJORAKER 1984. The Jovian atmospheric window at 2.7 microns: A search for H_2S. *Icarus* **60**, 621-639.

LELLOUCH, E., T. ENCRENAZ AND F. COMBES 1984A. The observability of HCN on Jupiter in the millimeter range. *Astron. Astrophys.* **135**, 365-370.

LELLOUCH, T. ENCRENAZ AND E., F. COMBES AND P. DROSSART 1984B. The observability of HCN and PH_3 on Saturn in the millimeter range. *Astron. Astrophys.* **135**, 371-376.

LELLOUCH, E., F. COMBES, AND T. ENCRENAZ 1984c. Microwave observations of Jupiter and Saturn. *Astron. Astrophys.* **140**, 216-219.

LELLOUCH, E., J. L. DESTOMBES 1985. Search for minor atmospheric species in the millimeter range of Jupiter and Saturn. *Astron. Astrophys.* **152**, 405-412.

LINDAL, G. F., G. E. WOOD, G. S. LEVY, J. O. ANDERSON, D. N. SWEETNAM, H. B. HOTZ, B. J. BUCKLES, D. P. HOLMES, P. E. DAMS, V. R. ESHLEMAN, G. L. TYLER, AND T. A. CROFT 1981. The atmosphere of Jupiter: An analysis of the Voyager Radio Occultation measurements. *J. Geophys. Res.* **86**, 8721-8727.

LINDAL, G. F., D. N. SWEETNAM, AND V. R. ESHLEMAN 1985. The atmosphere of Saturn: An analysis of the Voyager Radio Occultation measurements. *J. Geophys. Res.* **90**, 1136-1146.

LINDAL, G. F., J. R. LYONS, D. N. SWEETNAM, V. R. ESHLEMAN, D. P. HINSON, AND G. L. TYLER 1987. The atmosphere of Uranus An analysis of the Voyager Radio Occultation measurements. *J. Geophys. Res.* **92**, 14987-15002.

MIE, G. 1908. Beitrage zur optik truber medien, speziell kolloidaler metalasungen. *Ann. Physik*, **25**, 377.

MORRIS, E. C., AND R. W. PARSONS 1970. Microwave absorption by gas mixtures at pressures up to several hundred bars. *Astron. J. Phys.* **23**, 335-349.

PHILLIPS, T. G. 1989 Caltech Submillimeter Observatory (CSO) Handbook.

PALTRIDGE, G. W. AND C. M. R. PLATT 1976. *Radiative Processes in Meteorology and Climatology*, American Elsevier Publishing Co., Inc., New York.

POLLACK, J. B., AND P. BODENHEIMER 1989. Theories of the origin and evolution of the giant planets. In *Origin and evolution of atmospheres* (S. K. Atreya, J. B. Pollack and M. S. Matthews, Eds.), 564-602.

POYNTER, R. L., AND R. K. KAKAR 1975. The microwave frequencies, line parameters, and spectral constants for NH_3. *Astrophys. J. Suppl.* **29**, 87-96.

RATHER, J. D. G., B. L. ULICH, AND P. A. R. ADE 1974. Planetary brightness temperature measurements at 1.4 mm wavelength. *Icarus* **23**, 448-453.

ROMANI, P. N., I. DEPATER, AND S. K. ATREYA 1989. Neptune's deep atmosphere revealed. *Geophys. Res. Lett.* **16**, 933-936.

RUDY, D. J., D. O. MUHLMENAM, G. L. BERGE, B. M. JAKOSKY, P. R. CHRISTENSEN 1987. Mars: VLA observations of the northern hemisphere and the northern polar region at wavelengths of 2 and 6 cm. *Icarus* **71**, 159-177.

SILL, G., U. FINK, AND J. R. FERRARO 1980. Absorption coefficients of solid NH_3 from 50-7000 cm^{-1}. *J. Opt. Soc. Am.* **70**, 724-739.

SPILKER, T. R. 1990. Laboratory measurements of Microwave absorptivity and refractivity spectra of gas mixtures applicable to giant planet atmospheres. *Ph. D. thesis*, Stanford University, Stanford.

STEFFES, P. G., AND J. M. JENKINS 1987. Laboratory measurements of the microwave opacity of gaseous ammonia under simulated conditions for the Jovian atmosphere. *Icarus* **72**, 35-47.

SUTTON, E. C., G. A. BLAKE, C. R. MASSON, AND T. G. PHILLIPS 1985. Molecular line survey of Orion A from 215 to 247 GHz. *Astrophys. J. Suppl.* **58**, 341-378.

TERMAN, F. E. 1943. *Radio Engineers' Handbook.* McGraw-Hill Book Company, Inc., New York.

TOWNES, C. H., AND A. L. SHAWLOW 1955. *Microwave Spectroscopy.* McGraw-Hill, New York.

TYLER,G. L., D. N. SWEETNAM, J. D. ANDERSON, S. E. BORUTZKI, J. K. CAMPBELL, V. R. ESHLEMAN, D. L. GRESH, E. M. GURROLA, D. P. HINSON, N. KAWASHIMA, E. R. KURSINSKI, G. S. LEVY, G. F. LINDAL, J. R. LYONS, E. A. MAROUF, P. A. ROSEN, R. A. SIMPSON, AND G. E. WOOD 1989. Voyager radio science observations of Neptune and Triton. *Science* **86**, 1466-1473.

ULABY, F. T., R. K. MOORE, A. K. FUNG 1981. *Microwave Remote Sensing Active and Passive.* Addison-Wesley Publishing Company, Inc., Reading, MA.

ULICH, B. L. 1974. Absolute brightness temperature measurements at 2.1 mm wavelength. *Icarus* **21**, 254-261.

ULICH, B. L. 1981. Millimeter-wavelength continuum calibration sources. *Astron. J.* **86**, 1619-1626.

ULICH, B. L., J. R. COGDELL, AND J. H. DAVIS 1973. Planetary brightness temperature measurements at 8.6mm and 3.1 mm wavelengths. *Icarus* **19**, 59-82.

ULICH, B. L., J. H. DAVIS, P. J. RHODES, AND J. M. HOLLIS 1980. Absolute brightness temperature measurements at 3.5 mm wavelength. *IEEE Trans. Ant. Prop.*, **AP-28**, No. 3, 367-377.

ULICH, B. L., J. R. DICKEL, AND I. DEPATER 1984. Planetary Observations at a wavelength of 1.32 mm. *Icarus* **60**, 590-598.

VALKENBURG, E. P. AND V. E. DERR 1966. A High-Q Fabry-Perot interferometer for water vapor measurements in the 100 Gc/s to 300 Gc/s frequency range. *Proc. IEEE* **54**, No. 4., 493-498.

VAN VLECK, J. H., AND V. F. WEISSKOPF 1945. On the shape of collision-broadened lines. *Rev. Mod. Phys.* **17**, 433-443.

WALLACE, L. 1980. The structure of the Uranus atmosphere. *Icarus* **43**, 231-259.

WATERS, J. W. 1976 Absorption and emission of microwave radiation by atmospheric gases. In *Methods of Experimental Physics*, M. L. Meeks, ed., 12 Part B, Radio Astronomy, Academic Press, Section 2.3.

WERNER M. W., G. NEUGEBAUER, J. R. HOUCK, AND M. G. HAUSER 1978. One millimeter brightness temperatures of the planets. *Icarus* **35**, 289-296.

WEST R. A., D. F. STROBEL, AND M. G. TOMASKO 1986. Clouds, aerosols, and photochemistry in the Jovian atmosphere. *Icarus* **65**, 161-217.

WEIDENSCHILLING, S. J., AND J. S. LEWIS 1973. Atmospheric and cloud structures of the Jovian planets. *Icarus* **20**, 465-476.

WILLEY, D. R., T. M. GOYETTE, W. L. EBENSTEIN, D. N. BITTNER, AND F. C. DELUCIA 1989. Collisionally cooled spectroscopy: Pressure broadening below 5K. *J. Chem. Phys.* **91**, 122-125.

ZHARKOV, V. N. AND V. P. TRUBITSYN 1978. *Physics of Planetary Interiors* (W. B. Hubbard, Ed.), vol. 6 of *Astronomy and Astrophysics Series.* Puchart Publishing House, Tucson, AZ.

ZHEVAKIN, S. A., AND A. P. NAUMOV 1963. Coefficient of absorption of electromagnetic waves by water vapor in the range 10 microns-2 cm. *Radiophys. Quantum Electron.* **6**, 674-694.